

Confinement Effects on the Hydrodynamic Performance of a Fully-Passive
Oscillating-Foil Turbine

by

Sierra Mann

B.Sc., University of Saskatchewan, 2019

A Thesis Submitted in Partial Fulfillment of the
Requirements for the Degree of

MASTER OF APPLIED SCIENCE

in the Department of Mechanical Engineering

© Sierra Mann, 2022
University of Victoria

All rights reserved. This thesis may not be reproduced in whole or in part, by
photocopying or other means, without the permission of the author.

Confinement Effects on the Hydrodynamic Performance of a Fully-Passive
Oscillating-Foil Turbine

by

Sierra Mann

B.Sc., University of Saskatchewan, 2019

Supervisory Committee

Dr. Peter Oshkai, Co-Supervisor
(Department of Mechanical Engineering)

Dr. Guy Dumas, Co-Supervisor
(Department of Mechanical Engineering)

ABSTRACT

Current emissions targets have created a strong need for introducing more renewable energy sources into the energy mixture. The oscillating-foil turbine (OFT) has gained interest in recent years for renewable energy extraction. Experimental and numerical studies on the OFT experience different levels of wall confinement than what may be experienced at a natural site. Walls in close proximity will direct the flow at the turbine, causing a greater perceived velocity by the turbine, and thus a higher theoretical performance. This work aims to increase understanding of flow confinement on the fully-passive OFT. This is motivated by (1) enabling comparison between turbine performance operating at different confinement levels, and (2) potentially providing a means to enhance performance by designing a turbine which uses confinement to its advantage.

The experiments were performed using a NACA0015 foil with an aspect ratio of 7.5 in a water tunnel equipped with adjustable lateral walls. The foil was undergoing passive oscillations in pitch and heave degrees of freedom. The kinematic parameters of the foil oscillations and its energy harvesting performance were measured at eight blockage ratios, ranging from 22% to 60%, for two structural configurations of the turbine.

Quantitative flow imaging was performed using particle image velocimetry (PIV), at three confinement levels, to observe the timing of the leading-edge vortex (LEV) formation and shedding throughout the foil oscillation cycle. Loading on the foil was related to the flow structure by calculating the moments of vorticity with respect to the pitching axis of the foil.

The results showed that the efficiency and the power coefficient increased with increasing confinement. This was expected due to the higher incident velocity on the foil in the presence of the confining walls. At the highest level of confinement, the close proximity of the foil to the walls during parts of the oscillation cycle resulted in a change in the phase lag between the pitching and the heaving components of the foil motion. In turn, this shift in the kinematic parameters led to a sharp decrease in the energy-extraction performance of the turbine.

Contents

Supervisory Committee	ii
Abstract	iii
Contents	iv
List of Tables	vi
List of Figures	vii
List of Symbols	xi
Acknowledgements	xiii
1 Introduction	1
1.1 Background	1
1.1.1 Oscillating-foil Turbine	3
1.1.2 Confinement Effects	10
1.2 Objectives	11
1.3 Structure	13
2 Experimental System	14
2.1 Governing equations	14
2.2 Experimental Setup	20
3 Methodology	23
3.1 Freestream Velocity	23
3.2 Performance Data	23
3.3 Flow Visualization	24
4 Hydrokinetic performance of the fully-passive OFT	26

4.1	Baseline case of the OFT operating withing the true water flume walls	26
4.2	Effects of lateral confinement on the turbine performance	28
4.2.1	Blockage Corrections and Trends	32
5	Quantitative Flow Patterns	41
5.1	Two-dimensional Flow Patterns	41
5.2	Contributions of the shed vorticity to the instantaneous force on the foil	46
6	Conclusions	53
6.1	Future Work	55
A	False Wall Apparatus	58
B	Standard deviations of the kinematic and performance parameters	67
C	Uncertainty in the kinematic and performance parameters	70
D	Curve Fitting	72
D.1	ε vs. W/c curve fits	72
D.2	C_p vs. ε curve fits	75
D.3	η vs. ε curve fits	80
E	Blockage Corrections	85
E.1	Barnsley and Wellicome Correction	85
E.2	Houlsby Correction	90
	Bibliography	94

List of Tables

Table 2.1	List of parameters used in the governing equations of motion. Adapted from [1].	17
Table 2.2	Levels of confinement W/c enforced by the different false wall positions.	22
Table 4.1	Normalized structural parameters held constant for all experiments. Two pitch stiffness configurations were used, as specified in the table.	27
Table 4.2	Baseline performance of the turbine in the lowest confinement case for configurations $K0$ and $K056$	27
Table B.1	Standard deviations of kinematic and performance parameters for the $K0$ configuration	68
Table B.2	Standard deviations of kinematic and performance parameters for the $K056$ configuration	69
Table C.1	Uncertainties (%) in kinematic and performance parameters for the $K0$ configuration	70
Table C.2	Uncertainties (%) in kinematic and performance parameters for the $K056$ configuration	71

List of Figures

Figure 1.1	Extraction window of the OFT (left) compared to the extraction window of an HAT (right) [2]. The dashed lines indicate the total area swept by the turbine during operation.	2
Figure 1.2	Heaving and pitching motions of the oscillating-foil, with inflow left to right. Key parameters shown include: heave position $h(t)$, heave amplitude H_0 , pitch position $\theta(t)$, pitch amplitude θ_0 , chord length c , and total swept distance d [3].	3
Figure 1.3	Analytical model of confined flow passing through an actuator disk [4].	10
Figure 2.1	Schematic of the fully-passive OFT system, with flow moving right to left. Definitions of the key parameters shown are included in Tbl. 2.1 [1].	14
Figure 2.2	3D model of the fully-passive OFT used in this experimental work. The grey components are stationary, the blue component is the heaving carriage which moves only in the heave DOF, and the red components include the foil mounted on a pitching shaft; these components can move in both heave and pitch DOFs [5].	15
Figure 2.3	The set-up of the fully-passive turbine prototype with key structural components and measurement devices pointed out.	15
Figure 2.4	Illustration of the frontal areas defined in Eq. 2.16. H and W are the height and width of the flow cross section, respectively, and H_T and W_T are the foil's span and swept distance, respectively.	20
Figure 2.5	Schematic of the experimental setup, showing the false wall placement in the water channel.	21
Figure 3.1	Schematic of the flow imaging set-up, showing the planar light sheet at the foil's mid-span, illuminated by the Nd-YAG laser, and the camera perpendicular to the data acquisition plane. . .	25

Figure 4.1	Blockage ratio ε as a function of confinement level W/c , for the $K0$ and $K056$ configurations.	28
Figure 4.2	Efficiency η and power coefficient C_p functions of blockage ratio ε , for the $K0$ and $K056$ configurations.	29
Figure 4.3	Kinematic parameters of the OFT as functions of the blockage ratio ε . (a) normalized heave amplitude H_0^* , and pitch amplitude Θ_0 . (b) Reduced frequency f^* and phase lag ϕ	31
Figure 4.4	Plot of the curve fit Eq. 4.1 for blockage ratio ε vs. confinement level W/c for configurations $K0$ and $K056$. 95% confidence bounds are indicated by dashed lines.	34
Figure 4.5	Curve fits for the power coefficient C_p as a function of blockage ratio ε with 95% confidence bounds. (a) Polynomial fits for the $K0$ and $K056$ configurations using Eqs. 4.2 and 4.3. (b) Linear fits for the $K0$ and $K056$ configurations using Eqs. 4.4 and 4.5.	36
Figure 4.6	Curve fits for the efficiency η as a function of blockage ratio ε with 95% confidence bounds. (a) Polynomial fits for the $K0$ and $K056$ configurations using Eqs. 4.6 and 4.7. (b) Linear fits for the $K0$ and $K056$ configurations using Eqs. 4.8 and 4.9.	37
Figure 4.7	Comparison of the C_p curve data with the corrected data using the (a) BW correction. (b) Houlsby correction.	38
Figure 5.1	Patterns of the phase-averaged dimensionless out-of-plane vorticity at sequential phases (i) $t^*=0/10$, (ii) $t^*=1/10$, (iii) $t^*=2/10$, (iv) $t^*=3/10$, (v) $t^*=4/10$ for the $K0$ configuration. The top, middle and bottom rows correspond to confinement levels $C1$, $C4$, and $C7$, respectively, as defined in Tbl. 2.2. The inflow velocity magnitude $U_\infty = 0.38$ m/s is directed from top to bottom. The LEV is labelled A and the shed vortex from the previous half-cycle plus the TEV from the current half-cycle is labelled B. A^* denotes the trailing edge vortex from the previous half-cycle, where the new LEV has not yet formed.	42

Figure 5.2	Patterns of the phase-averaged dimensionless out-of-plane vorticity at sequential phases (i) $t^*=0/10$, (ii) $t^*=1/10$, (iii) $t^*=2/10$, (iv) $t^*=3/10$, (v) $t^*=4/10$ for the <i>K056</i> configuration. The top, middle and bottom rows correspond to confinement levels <i>C1</i> , <i>C4</i> , and <i>C7</i> , respectively, as defined in Tbl. 2.2. The inflow velocity magnitude $U_\infty = 0.38$ m/s is directed from top to bottom. The LEV is labelled A and the shed vortex from the previous half-cycle is labelled B.	43
Figure 5.3	Moment of vorticity (M_ω) of the primary vortex A (\bullet) and the shed vortex B (\circ) for the <i>K0</i> configuration. (a) Lateral moment (M_ω) _y . (b) Streamwise moment (M_ω) _x	48
Figure 5.4	Moment of vorticity (M_ω) of the primary vortex A (\bullet) and the shed vortex B (\circ) for the <i>K056</i> configuration. (a) Lateral moment (M_ω) _y . (b) Streamwise moment (M_ω) _x	49
Figure A.1	False wall assembly drawing.	59
Figure A.2	Post and plate assembly drawing.	60
Figure A.3	Top plate of post and plate assembly drawing.	61
Figure A.4	Bottom plate of post and plate assembly drawing.	62
Figure A.5	Post in the post and plate assembly drawing.	63
Figure A.6	False floor drawing.	64
Figure A.7	False wall 1 drawing.	65
Figure A.8	False wall 2 drawing.	66
Figure B.1	Time evolution of the normalized heave and pitch positions of the foil over 10 cycles for the <i>K0</i> configuration at confinement level <i>C0</i>	67
Figure B.2	Time evolution of the normalized heave and pitch positions of the foil over 10 cycles for the <i>K056</i> configuration at confinement level <i>C7</i>	68
Figure D.1	Comparison of curve trends of ε vs. W/c for the <i>K0</i> configuration.	74
Figure D.2	Comparison of curve trends of ε vs. W/c for the <i>K056</i> configuration.	75
Figure D.3	Comparison of curve trends of C_p vs. ε for the <i>K0</i> configuration.	77
Figure D.4	Comparison of curve trends of C_p vs. ε for the <i>K056</i> configuration.	79

Figure D.5 Comparison of curve trends of η vs. ε for the <i>K0</i> configuration.	82
Figure D.6 Comparison of curve trends of η vs. ε for the <i>K056</i> configuration.	84
Figure E.1 Illustration of the control volume used in the BW blockage correction analysis [6].	85
Figure E.2 Illustration of the control volume used in the 1D momentum analysis considering free surface effects and downstream wake mixing [7]	90

List of Symbols

ε	Blockage ratio
η	Efficiency
ω	Vorticity
ϕ	Phase lag
ρ	Density
θ	Pitch angle
b	Blade span
c	Blade chord
C_p	Power coefficient
$C_{F_y Coulomb}$	Coulomb friction force coefficient in heave
C_{F_y}	Hydrodynamic force coefficient in heave
$C_{M Coulomb}$	Coulomb friction moment coefficient
C_M	Hydrodynamic moment coefficient
D_θ	Pitch viscous damping coefficient
D_h	Linear heaving damping coefficient
$D_{h,v}$	Heave viscous damping coefficient
$D_{h,e}$	Heave eddy-current brake damping coefficient
f^*	Reduced frequency
h	Heave position
H_0	Heave amplitude
H_0^*	Normalized heave amplitude
I_θ	Moment of inertia
k_θ	Pitch stiffness constant
k_h	Heaving stiffness constant
M_ω	Moment of vorticity
m_h	Heaving mass

θ_0	Pitch amplitude
Re	Reynolds number
S	Static moment
T	Oscillation period
t^*	Normalized phase
U_∞	Freestream velocity
x_θ	Location of center of mass from pitching axis
x_p	Location of pitching axis from the leading edge

Abbreviations

2D	Two-dimensional
3D	Three-dimensional
CFD	Computational fluid dynamics
DOF	Degree of freedom
GHG	Greenhouse gas
LEV	Leading edge vortex
OFT	Oscillating-foil turbine
PIV	Particle image velocimetry
TEV	Trailing edge vortex

ACKNOWLEDGEMENTS

I would like to give my sincere thanks to those who have gotten me here:

Dr. Peter Oshkai, for your incredible mentorship in and beyond this academic work. You cultivated a collaborative and caring group atmosphere, which provided a great amount of room for academic and personal growth. Your passion for knowledge will continue to inspire me.

Dr. Guy Dumas, for providing your expertise, guidance, and support on this project. You brought new perspectives which enhanced my understanding on the topic.

Waltfred Lee and Kevin Gunther, for taking the time to share your works and knowledge on the subject. It was a pleasure to collaborate with both of you, and I appreciate the additional understanding it provided me, enabling the current work to happen.

Research groupmates, Duncan McIntyre, Chad Magas, Curtis Evans, AJ Messner, and Gleb Sharikov, for standing by me through this process. Having friends like you made this experience all the more enjoyable.

My parents, Rob and Lana, and my partner, Dylan Zaluski, for continual support and encouragement through this journey.

Chapter 1

Introduction

1.1 Background

Over the past ten years, global warming of over 1°C has occurred due to emissions from human activities. The largest contributors to this temperature increase are carbon dioxide and methane. Effects of global warming including weather and climate extremes, heavy precipitation, draught, and sea level rise are already being observed today. With each incremental temperature increase, these global weather events are expected to become more severe and frequent [8]. To intervene, the Paris Agreement was signed by 195 countries, including Canada, in 2015 to limit the global temperature increase to 1.5°C [9]. This corresponds to achieving net zero greenhouse gas (GHG) emissions by 2050. According to the IEA, three-quarters of global GHGs are contributed by the energy sector. There is therefore a large emphasis on a shift to renewable energy sources in the Net Zero 2050 framework. Renewables including wind, solar, geothermal, bioenergy, and hydro will make up the majority of the energy mixture by 2050, while fossil fuels will fall from around four-fifths to one-fifth of the energy mixture [10].

Harvesting hydrokinetic energy from tidal and river flows is a promising renewable source due to the predictability and high energy density in these zones [6]. Although these flows have been relatively untapped, Canada is one of the countries developing this form of power, with two major sites in Baie d'Ungava in Québec and the Bay of Fundy in Nova Scotia. The overall hydrokinetic potential in Canada is estimated to be 15,000 MW from river flows and 42,000 MW from tidal flows, while the global potential for tidal energy is estimated to be 17,500 TWh/yr [11]. The tide cycle is well

predicted, so this energy form is desirable due to its dependability and certainty [12]. With many urban centers neighbouring bodies of water, these sites are also ideal for efficient energy transportation directly to the electrical grid.

Hydrokinetic turbines are used to convert the kinetic energy of flowing water into usable mechanical energy. This can then be converted to electric energy to be directly fed into the electrical grid or stored by batteries. The main forms of hydrokinetic turbines include horizontal axis turbines (HAT), vertical axis turbines (VAT), and oscillating-foil turbines (OFT). The HAT operates using blades which rotate at a constant angular velocity around an axis aligned with the flow. This is the most mature type of turbine due to its applications in both the wind energy and propeller sectors. For this reason, it is currently the most used for tidal applications. The major downfall of the HAT with respect to tidal and river applications is the circular energy extraction window. In contrast, the VAT and OFT extract energy from a rectangular flow window. This is more ideally suited to a shallow river or tidal flow applications because it maximizes the exploitable flow energy in a given area, as is illustrated in Fig. 1.1.

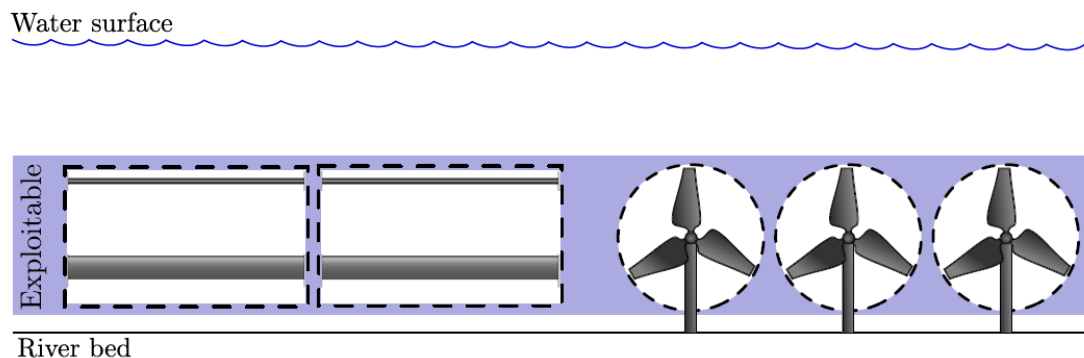


Figure 1.1: Extraction window of the OFT (left) compared to the extraction window of an HAT (right) [2]. The dashed lines indicate the total area swept by the turbine during operation.

The VAT extracts flow energy through rotational motion of the blades, similar to the HAT. However, the blades instead rotate around an axis which is perpendicular to the oncoming flow. This design makes the turbine operation independent of the incoming flow direction. In contrast, the OFT consists of one or more blades undergoing a lateral flapping motion to extract energy, rather than the rotational blade motion used in the VAT and HAT designs. Since the OFT does not undergo rotary motion, it is not subjected to centrifugal forces. This makes it a more robust

option compared to the VAT, while still offering the desirable rectangular sweep area for shallow water applications. The OFT is the focus of this thesis - the following sections will further describe its specific operating principle and state of the art.

1.1.1 Oscillating-foil Turbine

Oscillating-foils, or flapping-wings, are streamlined bodies which move in heaving and pitching degrees of freedom (DOFs) in stable, periodic cycles. The heave DOF $h(t)$ refers to translational motion perpendicular to the flow direction and its amplitude H_0 defined as the maximum offset from its equilibrium axis. The pitch DOF $\theta(t)$ is the axial rotation about the pitching axis, with amplitude Θ_0 defined as the maximum angular offset from its equilibrium axis. The two DOFs operate with a phase lag ϕ between them, such that the maximum travel of each motion occurs at different times in the oscillation cycle. The foil undergoes a maximum travel d during pitch reversal measured at the trailing edge of the foil. These kinematics are illustrated in Fig. 1.2, where the foil is subjected to an inflow coming from the left.

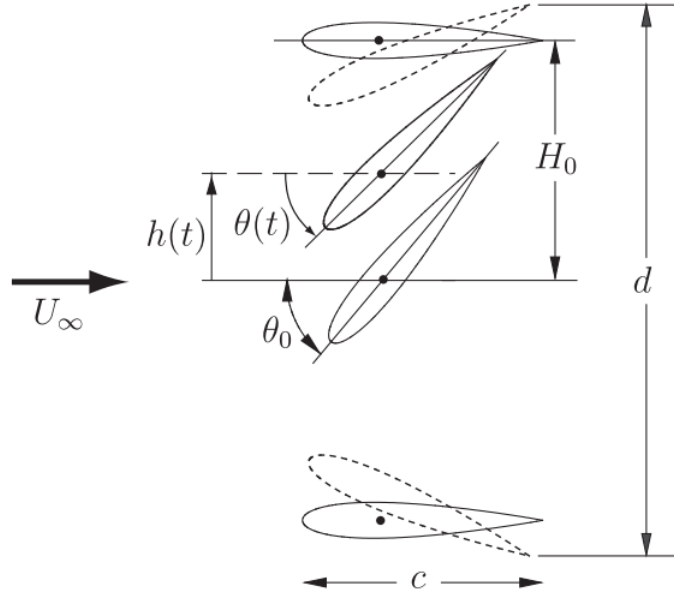


Figure 1.2: Heaving and pitching motions of the oscillating-foil, with inflow left to right. Key parameters shown include: heave position $h(t)$, heave amplitude H_0 , pitch position $\theta(t)$, pitch amplitude θ_0 , chord length c , and total swept distance d [3].

The motion of the oscillating-foil is inspired by nature. This type of motion can be observed in bird or insect flight [13], or in the undulations of a fish's caudal fin [14,15].

The propulsion and maneuvering observations have been used in technology such as unmanned machines [16], ships, and submarines [17,18]. In addition to these examples of the structure introducing energy into the flow, other everyday structures present us with examples of the opposite. Energy can also be transmitted to the structure, as can be observed in special circumstances of planes' wings fluttering or bridges galloping [19]. As energy is introduced to the structure, it will oscillate with growing motions unless the energy is damped out. Although it is undesirable to have the transfer of energy from the flow to the structure in these circumstances, this idea provides us with the potential to harvest energy from a flow.

The underlying physics of the energy transfer between the oscillating-foil and surrounding flow has been thoroughly investigated to facilitate useful applications [20]. The lift generated from flapping wings is strongly linked to the strength and evolution of the leading edge vortex (LEV) [21, 22]. The unsteady lift generation was observed in early investigations of insect flight [23, 24]. Further investigations of the relationship between the LEV and the forces acting on the foil have been conducted for the energy harvesting application, which demonstrated that the LEV timing with respect to the structural motion was key for high energy extraction performance [25–28].

Energy Harvesting Mode

The OFT refers to the case for which there is a net energy transfer from the flow to the oscillating-foil. The turbine moves in both DOFs with a phase lag between them, as described previously. The foil experiences an effective theoretical angle of attack α_{eff} to the oncoming flow based on the pitch angle and the relative motion of the foil with respect to the inflow velocity,

$$\alpha_{eff}(t) = \arctan(-\dot{h}(t)/U_\infty) - \theta(t), \quad (1.1)$$

where \dot{h} is the foil's heave velocity and U_∞ is the freestream velocity. This equation is theoretical, only, because it uses the freestream velocity, and therefore does not account for the slowing of the flow immediately upstream of the turbine. The pitch amplitude, and thus the effective angle of attack, must be large to promote dynamic stalling, and the limit cycle oscillation phenomenon. The kinematic parameters characterizing the turbine's motion include the heave amplitude H_0 , the pitch amplitude Θ_0 , the frequency of oscillation f , and the phase lag between the two DOFs ϕ . Ex-

tensive compilations of research on the operation and optimization of the OFT can be found in reviews by Young et. al [29], Xiao and Zhu [30] and Wu et al. [31].

Following the work of McKinney and Delaurier in 1981 [32], the field of OFTs has grown in the interest of optimizing the concept for commercial deployment. Their work introduced the wingmill: a small experimental turbine with prescribed phasing between DOFs. The foils in most studies move in sinusoidal motion, with heave and pitch motion described by

$$h(t) = H_0 \sin(\gamma t + \phi), \quad (1.2)$$

$$\theta(t) = \Theta_0 \sin(\gamma t), \quad (1.3)$$

where γ is the angular frequency. Active control of the kinematic parameters to impose the sinusoidal profile can be achieved by actuation or by physical linkages. Knowing the flow induced forces and moments on the foil, the total extracted power can be obtained from the sum of the power extracted from the heave and pitch DOFs:

$$P(t) = P_Y(t) + P_\theta(t) = Y(t)\dot{h}(t) + M(t)\dot{\theta}(t), \quad (1.4)$$

where P_Y is the power extraction from the heave DOF, P_θ is the power extraction from the pitch DOF, Y is the hydrodynamic force on the foil acting in the heave direction, M is the hydrodynamic moment acting on the foil about the pitch axis, and $\dot{\theta}$ is the pitch velocity. It is clear from this equation that an efficient energy harvester requires that the highest hydrodynamic forces are well-timed with the highest velocities during the oscillation cycle. If the terms become negative, the foil is instead transferring energy to the water, thus acting in the propulsion regime instead of the energy harvesting regime.

A large amount of research has been devoted to validating the feasibility of the OFT. The potential of the OFT was revisited by Jones et al. [33] where they demonstrated a vast underperformance of a physical prototype with respect to numerical predictions, and that there was a large amount of room for developing the concept. Kinsey and Dumas [34] investigated the parametric space by varying the frequency and pitch amplitude in a 2D, low Reynolds Number (Re) numerical study. They found that efficiencies as high as 34% were achievable with a large pitching amplitude of 70° to 80°, and a reduced frequency f^* between 0.12 and 0.18 (unitless). This

was a promising finding, given the practical efficiency limit of 59%, from the Betz limit [35]. Subsequently, Kinsey and Dumas [3] tested a prototype to better evaluate real-world feasibility. The prototype consisted of a linkage between pitch and heave to create a one DOF system, and operated with two foils in tandem. Promising results were achieved with a maximum system efficiency of 40%, however, major mechanical losses up to 25% were incurred due to friction in the linkages. A single foil prototype was tested by Abiru and Yoshitake [36] in the same year, confirming this range of efficiencies, with their turbine achieving efficiencies between 32 and 37%.

Activation Modes

The oscillating-foil can be operated in three different activation modes: fully-active, semi-passive, or fully-passive. A large amount of research has gone into the fully-active turbine, where kinematics of both the pitch and heave degrees of freedom are prescribed. The kinematics may be controlled using actuation with an input signal to control motion shapes (e.g., [37]), they can be controlled using physical linkages to constrain the motion and couple the degrees of freedom with a prescribed phase lag (e.g., [32]), or they can be controlled using a combination of the two (e.g., [3]). Although having control of the motion is ideal in order to implement the optimal kinematics for high performance, the actuation and physical linkages impose additional complexity to the system that can lead to higher costs, higher losses due to friction, and more moving parts leading to a less robust system.

To address these concerns, passive operation modes have been pursued, where either one or both of the DOFs are passively controlled using spring-and-damper systems. The semi-passive turbine uses a motor to drive one DOF, while the other DOF responds to the oscillatory forces. Most studies have focused on driving pitch motion and passively controlling heave motion [36, 38–42], achieving efficiencies in the range of 25–37%. More recently, Boudreau et al. [43] investigated the possibility of controlling the heave motion only. Their high Re , 2D study achieved a maximum efficiency of 45.4%.

The system may be even further simplified by removing all actuation and mechanical coupling to achieve a fully-passive system. Poirel et al. [44] first demonstrated the possibility of stable oscillations of a foil which is elastically mounted in both pitch and heave. The potential of harvesting energy from the stable passive oscillations has been further pursued in the recent years. Different studies have explored the para-

metric space to determine which conditions the foil could harvest energy in. Peng and Zhu [45] found that there are four different responses of the elastic system, with one of the responses being suitable for energy harvesting. This has later been backed up by other studies [46, 47].

Further numerical work has been done to validate the potential of the fully-passive concept [48–53]. Veilleux and Dumas [52] optimized the fully-passive turbine using a 2D numerical solver to vary the parametric space. They found that the main beneficial mechanisms for enhancing turbine performance are the synchronization between the DOFs, and the nonsinusoidal shape of the pitching motion. Boudreau et al. [1] later designed an experimental prototype based on the optimal case from Veilleux and Dumas’ work. The prototype achieved a promising energy harvesting efficiency of 31% in its most optimal case. Duarte et al. [54] further investigated the parametric space of a fully-passive OFT prototype, where they demonstrated the optimal parameter space between the pitch parameters: the pitch axis, pitch damping, and pitch stiffness. Recently, another experimental prototype was demonstrated by Qadri et al. [55], where they introduced physical heave and pitch limiters. This concept further supports the ability of the turbine to operate with elastically supported degrees of freedom; however, it is worth noting that their definition of fully-passive does not quite align with that used here: the operating parameters are not directly controlled in any way.

Towards Industrial Deployment

Industrial deployment of the OFT has been attempted in the past by UK companies Engineering Business Ltd. and Pulse Tidal. Unfortunately, neither of these deployments were successful due to low efficiencies making them not economically viable. Much of the research into OFTs has therefore focused on both optimizing the turbine’s performance and investigating real-world effects to provide an economically viable option.

Optimization of the turbine has included its kinematics, geometry, and structure. According to Kinsey and Dumas [34], the kinematics of the turbine provide the largest performance enhancements, while geometry and viscous properties provide secondary effects. In their numerical parametric study, efficiency was maximized at large pitching amplitudes which promoted dynamic stall. Past research has looked at the effects of varying specific kinematic parameters and their effects on the fluid-structure inter-

action and performance. The optimal frequency of the turbine is that which matches the frequency of the most unstable wake mode [56]. Most works have considered the heave amplitude on the order of one chord length; however, large amplitude motions up to $15c$ have also shown high efficiencies [57]. At a higher heave amplitude, the turbine has access to a large flow window, so the total power extraction will increase, but the efficiency may increase or decrease.

The optimal kinematics align the timing of the flow forces with the maximum foil velocities, since power extraction is the product of the two parameters, as demonstrated in Eq. 1.4. Therefore, the phase lag between the two DOFs is a key parameter. McKinney and Delaurier’s [32] pioneering work showed that the optimal efficiency is achieved at $\phi \approx 90^\circ$ while the maximum power output is achieved at $\phi \approx 110^\circ$ for a larger flow window. Other attempts to manipulate the timing of the flow and kinematics have included using non-sinusoidal pitch profiles in both propulsive and energy extraction applications. While a sinusoidal profile has proven optimal for propulsive applications, the non-sinusoidal profile has been proven to enhance performance for energy extraction applications [26, 58–61].

Modifications to the shape, structure, and geometry have also been introduced to enhance the turbine performance. Enhancements in performance have arisen from the use of combined foils [62], gurney flaps [63], and added surface roughness [64] by manipulating the boundary layer and the LEV development. Foil flexibility has also proven to be effective, as it alters the local angle of attack and leads to enhanced lift [65]. Implementing passive and actively deforming foils has been shown to enhance efficiency by over 30%, relative to low-efficiency cases of the rigid foil [66–68]. The location of the pitching axis with respect to the center of gravity and location of force application is important for the turbine kinematics and performance. The optimal location depends on other set parameters, although past works investigating this subject have found that the optimal location is between $0.3c$ and $0.5c$ [34, 39, 69].

Considerations for real-world deployment have also been investigated to further evaluate the viability of the oscillating-foil for tidal generation. Most of the research in this area has relied on numerical models, which consider a 2D problem since it is less computationally expensive. The drawback is that it does not account for 3D effects such as tip losses and free surface effects. Direct comparison between the 2D and 3D configurations shows a drop in performance of 20-30%, although these losses can be limited to 10% with the use of endplates on each of the extremities [70]. Kim et al. [71] investigated the effect of the finite span on pitch and heave performance

individually, finding that the 3D effect did not affect pitch performance, but that the heave efficiency scaled linearly with aspect ratio due to the delay in LEV growth.

Flow is controlled and conditioned in an experiment, however the conditions may be variable in an environmental setting. This may include changes in turbulence levels, shear effects, and variable velocity. Studies looking at higher Reynolds numbers on the order of 10^5 to 10^6 have revealed that energy extraction performance is enhanced in the turbulent flow compared to laminar flow. The flow field has also been shown to differ greatly from the laminar case, where the presence of the LEV is no longer an important driving mechanism [72, 73]. The effect of high Reynolds number on the fully-passive turbine was later investigated by Boudreau et al. [53], where they found that the performance matched that of the fully-active case. Other environmental effects have been found to have less of an impact, such as shear layer effects and time varying velocity, where the performance of the turbine was comparable to that in uniform flow [48, 74].

In addition to environmental considerations, the form of deployment would likely include arrays of flow harvesters, similar to wind farms. Towards this goal, studies have investigated the interactions between two or more foils which operate in tandem or parallel configurations. Most studies to date have focused on the tandem configuration, where the foils share the same flow window. The phase shift and distance between turbines are the key parameters to determine whether the turbines will interact constructively or destructively, but with proper parameters, the configuration shows promising performance [75–79]. Extending these studies to have more than two foils operating in tandem, Karbasian et al. [80] found that the efficiency increased with increased foils up until a certain number where efficiency remains the same. Ma [81] demonstrated that a hydraulic coupling system could be used for a parallel system, which was able to maintain continuity of the foils’ motions without any external control.

An additional key consideration to understand how OFTs will operate at an environmental site is the level of confinement the turbine operates within. It is known that flow over a solid body will impose different forces in an unconfined versus confined setting [82]. This will be further explored in the following section with application to hydrokinetic turbines.

1.1.2 Confinement Effects

Operating a turbine within confining walls has been shown to enhance energy extraction performance by forcing more flow through the turbine [83]. Intentionally deploying the OFT in a confined environment could therefore be beneficial from a performance viability standpoint. In addition, quantifying confinement effects is important to allow for comparison between experiments and deployment at natural sites. Experimental studies are limited to the confinement of the water tunnel, and must be compared to deployment in sites which may experience less confinement. Computational fluid dynamics (CFD) studies often consider operation in a very large, unconfined domain, and must be compared to natural sites which would experience varying levels of confinement from local bathymetry and proximity to the seabed and free surface, in addition to confinement effects from neighbouring turbines if deployed in an array.

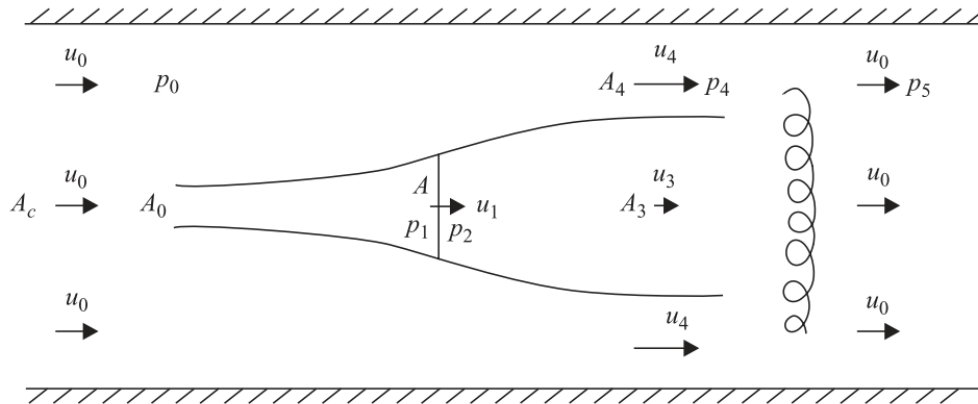


Figure 1.3: Analytical model of confined flow passing through an actuator disk [4].

Analytical models using axial momentum theory on an actuator disk, demonstrated in Fig. 1.3, have been used to develop corrections for blockage. The first correction was developed by Glauert [84] for propellers being tested in a wind tunnel. These models have been extended to develop similar corrections for general bluff bodies and streamlined bodies [82], as well as for turbines operating near walls and free surfaces, and demonstrate enhanced power extraction when operating in a confined channel versus an open environment [4, 7, 85–87]. Numerical and experimental works have confirmed an increase in performance of different types of turbines operating in confinement [83, 88, 89]. Further, studies have compared experimental results with predictions made by analytical models, finding mixed results in how well the

experiments aligned with the models [90].

Several studies have been conducted to assess the effects of confining walls on the performance and operation of the OFT. Gauthier et al. [6] found an increase in performance which they attributed to a larger effective angle of attack due to the local flow acceleration, which lead to a stronger LEV. Su et al. [91] investigated the effect of both one and two-wall confinement, which both lead to an increase in efficiency with a more pronounced effect for the two-wall configuration. As confining walls get closer to the foil, a drop in performance has been observed due to vorticity interaction with the wall, indicating an optimal wall spacing exists for enhancing the energy extraction performance [92, 93].

There have not yet been studies to determine the effects of confining walls on the fully-passive activation mode of the OFT. For this case, there is expected to be a performance increase by forcing more flow through the turbine, as observed for previously investigated turbines. Unlike the past works on active OFTs, though, the fully-passive OFT's kinematics are subject to change with environmental changes. This introduces more uncertainty into how the performance of the turbine will change as the confinement level is increased.

1.2 Objectives

Exploring how a device performs under confinement has been heavily researched to better understand how experiments can be compared to full scale operation. Most experiments are conducted in a flume or tow tank with set dimensions, and therefore a set confinement level. Since it is understood that the flow forces on a solid body change with changing confinement level, the results of a controlled experiment may not exactly reflect how the device will perform when deployed in a natural setting. It has been shown analytically, numerically, and experimentally that all geometries of turbines will demonstrate higher performance with higher confinement levels. It is important to understand to what extent performance is expected to be altered. Additionally, knowing the potential performance increase can be used to design for a confined turbine configuration that can enhance energy extraction performance. Confinement studies are thus very practically important for confidence in comparing energy extraction potential at different sites, and for increasing efficiency and therefore viability of the fully-passive OFT for energy harvesting at river and tidal sites.

While there has been extensive research on the effect of confinement for axial and

cross-flow rotary turbines, research has been limited for the oscillating-foil turbine since it is a less mature area. Of these studies, none of them focus on the fully-passive OFT concept. The fully-passive OFT is expected to follow the general trend of increased performance with confinement; however, the passive concept allows for all kinematic parameters to change in addition to the effective flow magnitude and direction that has been observed in other turbine confinement studies. Without a constant kinematic parameter space, it is unknown to what extent the passive turbine will align with classic confinement analysis and experimental studies on fully constrained turbines. Further, stable limit-cycle oscillations are not guaranteed since kinematics are not directly imposed. It is therefore also important to determine whether stable and periodic motions are maintained as the turbine experiences increasing levels of confinement. The viability of the fully-passive OFT operating in different confinement levels without adjustment of its structural parameters is to be established.

This thesis aims to bridge this gap by experimentally investigating the effect of a fully-passive OFT prototype operating within different spacing of confining walls. The fully-passive prototype produced by Boudreau et al. [5] was studied in the water tunnel in the Fluid Mechanics Laboratory at the University of Victoria. The turbine consists of a NACA0015 foil, elastically supported in pitch and heave. The water channel is equipped with a false wall apparatus to vary the level of lateral confinement the turbine is subjected to. The present work studies the effect of confinement on the performance metrics and links the performance changes to the changes in turbine kinematics. The secondary investigation uses particle image velocimetry (PIV) for flow imaging to observe the flow feature evolution both qualitatively and quantitatively, and relate the flow evolution to the changes in performance.

The author aims to add to the collective effort of oscillating-foil studies, specifically on the impact of flow confinement on the operation of the fully-passive OFT. The present work will contribute the ability to compare model and real-world scale performance, and provide a means to enhance performance of the turbine. Both of these motivators ultimately aid in the eventual practical development of the OFT and eventual large scale deployment for energy harvesting.

1.3 Structure

This section provides the layout of the thesis. The following chapters will provide the theory of the fully-passive OFT, a description of the experimental prototype and confinement apparatus, followed by the data acquisition and visualization techniques and their respective results. The thesis is concluded with a summary of key findings and recommendations for future work. The contents of each chapter are as follows:

Chapter 1 Presents a general overview of the OFT operation modes. It includes a brief overview of existing studies to understand the turbine's performance potential and the viability of full scale deployment. Finally, an overview of the studies involving confinement effects on hydrokinetic turbines is presented.

Chapter 2 Describes the fundamentals of the fully-passive OFT prototype and the performance parameters which characterize the turbine's operation. The experimental set-up is described, including the set up of both the turbine and the confinement apparatus in the water channel.

Chapter 3 Describes the Data Acquisition for performance quantification and the PIV methodology used to acquire time resolved velocity field measurements.

Chapter 4 Presents the power extraction performance of the turbine under different confinement levels, for two different configurations of structural parameters. Kinematics are analyzed to describe the shift in performance at different confinement levels. Performance data is described with curve fits and compared with existing blockage corrections.

Chapter 5 Presents the PIV results at three different confinement levels for the two structural configurations. Visual results are presented to demonstrate the LEV formation and wake evolution. An analysis and results of the forces induced on the foil by the wake vorticity is presented.

Chapter 6 Contains a summary of main findings of this experimental campaign and provides avenues for future work.

Chapter 2

Experimental System

2.1 Governing equations

The fully-passive turbine used in this campaign is the same physical prototype used in the studies by Boudreau et al. [1,5]. The reader may refer to these works for details of the prototype's design and calibration. Only key parameters that are relevant to this study will be included here. A schematic modeling the the two DOF turbine system is provided in Fig. 2.1. The figure demonstrates the foil's position with respect to the oncoming flow at an arbitrary instant in time, the stiffness and damping components in each DOF, and definitions of key dimensions.

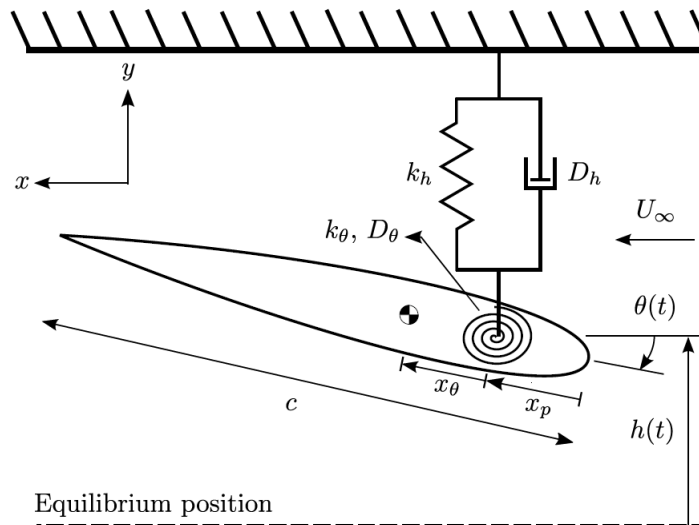


Figure 2.1: Schematic of the fully-passive OFT system, with flow moving right to left. Definitions of the key parameters shown are included in Tbl. 2.1 [1].

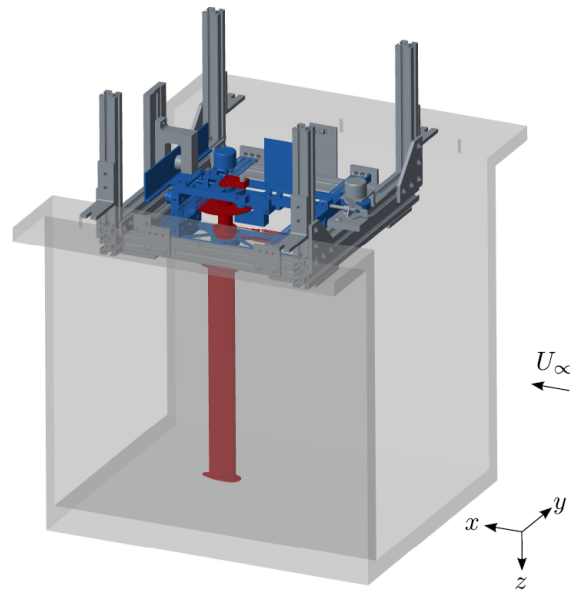


Figure 2.2: 3D model of the fully-passive OFT used in this experimental work. The grey components are stationary, the blue component is the heaving carriage which moves only in the heave DOF, and the red components include the foil mounted on a pitching shaft; these components can move in both heave and pitch DOFs [5].

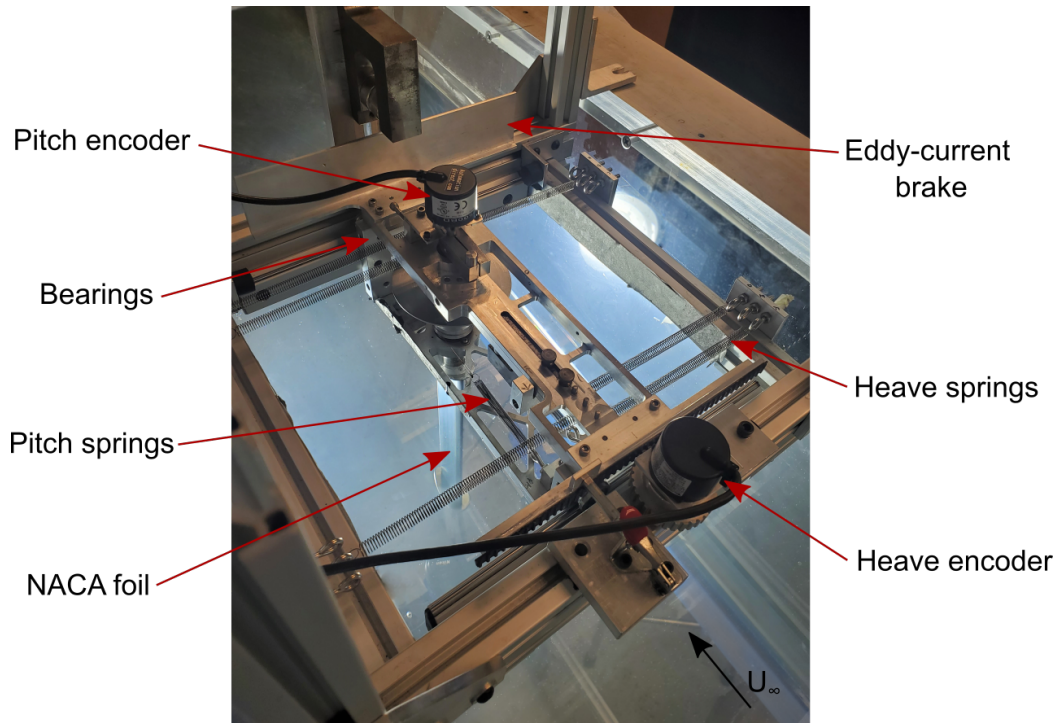


Figure 2.3: The set-up of the fully-passive turbine prototype with key structural components and measurement devices pointed out.

A model of the fully-passive OFT prototype is shown in Fig. 2.2, with the moving components identified by colour. A top view of the physical prototype, indicating some of the key structural parameters is provided in Fig. 2.3.

The dimensionless governing equations for the fully-passive OFT motion are provided in Eqs. 2.1a and 2.1b [94]. The derivation of these equations is provided in the thesis of Veilleux [95]. Each equation of motion consists of a hydrodynamic term, inertial term, inertial coupling term, structural term, and Coulomb friction term, as is labeled below.

$$C_{F_y}/2 = m_h^* \ddot{h}^* + S^* \left(\ddot{\theta}^* \cos\theta - \dot{\theta}^{*2} \sin\theta \right) + D_h^* \dot{h}^* + k_h^* h^* + C_{F_y \text{Coulomb}}/2, \quad (2.1a)$$

$$\underbrace{C_M/2}_{\text{hydrodynamic}} = \underbrace{I_\theta^* \ddot{\theta}^*}_{\text{inertial}} + \underbrace{S^* \ddot{h}^* \cos\theta}_{\text{inertial coupling}} + \underbrace{D_\theta^* \dot{\theta}^* + k_\theta^* \theta}_{\text{structural}} + \underbrace{C_{M \text{Coulomb}}/2}_{\text{Coulomb friction}}, \quad (2.1b)$$

where the superscript ($\dot{}$) denotes that a term is differentiated with respect to time, and the superscript ($\ddot{}$) denotes the term is twice differentiated with respect to time. The terms in Eqs. 2.1a and 2.1b are defined in Tbl. 2.1, with their mathematical definitions provided in Eqs. 2.2 through 2.6.

$$C_{F_y} = \frac{F_y}{0.5\rho U_\infty^2 bc}, \quad C_{F_y \text{Coulomb}} = \frac{F_y \text{Coulomb}}{0.5\rho U_\infty^2 bc}, \quad (2.2)$$

$$C_M = \frac{M}{0.5\rho U_\infty^2 bc^2}, \quad C_{M \text{Coulomb}} = \frac{M_{\text{Coulomb}}}{0.5\rho U_\infty^2 bc^2}. \quad (2.3)$$

$$m_h^* = \frac{m_h}{\rho bc^2}, \quad I_\theta^* = \frac{I_\theta}{\rho bc^4}, \quad S^* = \frac{S}{\rho bc^3}, \quad (2.4)$$

$$D_h^* = \frac{D_h}{\rho U_\infty bc}, \quad D_\theta^* = \frac{D_\theta}{\rho U_\infty bc^3}, \quad k_h^* = \frac{k_h}{\rho U_\infty^2 b}, \quad k_\theta^* = \frac{k_\theta}{\rho U_\infty^2 bc^2}, \quad (2.5)$$

$$h^* = \frac{h}{c}, \quad \dot{h}^* = \frac{\dot{h}}{U_\infty}, \quad \ddot{h}^* = \frac{\ddot{h}c}{U_\infty^2}, \quad \dot{\theta}^* = \frac{\dot{\theta}c}{U_\infty}, \quad \ddot{\theta}^* = \frac{\ddot{\theta}c^2}{U_\infty^2}. \quad (2.6)$$

The static moment S^* is the product of the mass undergoing pitch motion and

Table 2.1: List of parameters used in the governing equations of motion. Adapted from [1].

Symbol	Units	Definition
b	[m]	Blade span length
c	[m]	Blade chord length
ρ	[kg/m ³]	Water density
U_∞	[m/s]	Freestream velocity
θ	[rad]	Pitch angle
t	[s]	Time
x_p	[m]	Distance between leading edge and pitch axis
x_θ	[m]	Distance between the pitch axis and the center of mass (defined positive when the pitch axis is upstream of the center of mass)
F_y	[N]	Hydrodynamic force component in the heave (y) direction
M	[N·m]	Hydrodynamic moment about the pitch axis
$F_{y\ Coulomb}$	[N]	Coulomb friction force component in the heave (y) direction
$M_{Coulomb}$	[N·m]	Coulomb friction moment about the pitch axis
m_h	[kg]	Mass of all the components undergoing the heaving motion
I_θ	[kg·m ²]	Moment of inertia about the pitch axis
S	[kg·m]	Static moment (mass of the components only undergoing pitching motion times x_θ)
D_h	[N·s/m]	Total linear heave damping coefficient
$D_{h,e}$	[N·s/m]	Linear heave damping coefficient of the eddy-current brake (desired energy sink)
$D_{h,v}$	[N·s/m]	Linear heave damping coefficient of the heave bearings
D_θ	[N·m·s/rad]	Linear pitch damping coefficient of the pitch bearings
k_h	[N/m]	Heave stiffness coefficient
k_θ	[N·m/rad]	Pitch stiffness coefficient

the distance between the pitch axis and center of mass. It acts as an inertial coupling between the pitch and heave DOF, as demonstrated by its appearance in both Eqs.2.1a and 2.1b. This quantity is also referred to as the static imbalance in previous works [47, 54, 95].

The turbine system includes both desired and undesired sources of damping. The eddy-current damper is used as an energy sink to model the energy that would be available for conversion to electricity by an electric generator. The bearings present inherent undesirable friction in the form of linear viscous damping and Coulomb friction. D_h is therefore defined as the sum of the desired energy sink damping coefficient $D_{h,e}$ and the undesired viscous damping coefficient $D_{h,v}$:

$$D_h = D_{h,e} + D_{h,v}. \quad (2.7)$$

The eddy current damper in pitch was not used in this experimental campaign, so the damping in pitch consists only of viscous damping:

$$D_\theta = D_{\theta,v}. \quad (2.8)$$

The eddy-current damper in heave consists of a thin aluminum plate attached to the heave carriage, and a magnetic yoke through which the plate travels at a predetermined relative distance. The damping coefficient can be adjusted by changing the height of the magnetic yoke which corresponds to a change in the strength of the magnetic field passing through the aluminum plate. With the knowledge of the damping coefficient and the heave velocity of the aluminum plate, the cycle-averaged power dissipated through the eddy-current brake $\overline{P_{h,ej}}$ can be evaluated using the following equation:

$$\overline{P_{h,ej}} = \frac{1}{T_j} \int_t^{t+T_j} (D_{h,e} \dot{h}^2) dt, \quad (2.9)$$

where T_j is the period of oscillation at the j^{th} cycle, and the other parameters are listed in Tbl. 2.1. The two key indicators of the energy extraction performance are the efficiency η_{ej} and the power coefficient $\overline{C_{P_{h,ej}}}$, defined as

$$\eta_{ej} = \frac{\overline{P_{h,ej}}}{\frac{1}{2} \rho U_\infty^3 b d_j}, \quad (2.10)$$

$$\overline{C_{P_{h,ej}}} = \frac{\overline{P_{h,ej}}}{\frac{1}{2}\rho U_\infty^3 bc} = \eta_{ej} \frac{d_j}{c}, \quad (2.11)$$

where η_{ej} describes the power extraction with respect to the power available in the flow window, and $\overline{C_{P_{h,ej}}}$ is normalized by the size of the blade. d_j is defined as the distance between the maximum and minimum positions reached by any point on the foil in the heave direction during one complete foil oscillation. The maximum heave position reached by the foil at any point in the oscillation cycle was calculated using the sum of the heave position measured at the pitching axis and the additional heave distance reached by the trailing edge of the foil, calculated using the instantaneous pitch angle.

The key kinematic parameters used to characterize the turbine's motion over an oscillation cycle include the reduced frequency f_j^* , the phase lag ϕ_j , the normalized heave amplitude H_{0j}^* , and the pitch amplitude Θ_{0j} . These are given by Eqs. 2.12 through 2.15:

$$f_j^* = \frac{f_j c}{U_\infty}, \quad (2.12)$$

$$\phi_j = \frac{360^\circ}{T_j} (t_{\theta_{maxj}} - t_{h_{maxj}}), \quad (2.13)$$

$$H_{0j}^* = \frac{h_{maxj} - h_{minj}}{2c}, \quad (2.14)$$

$$\Theta_{0j} = \frac{\theta_{maxj} - \theta_{minj}}{2}. \quad (2.15)$$

Following the definition of Gauthier et al. [6], the blockage ratio ε is given by:

$$\varepsilon = \frac{A_T}{A} = \frac{W_T}{W} \frac{H_T}{H}, \quad (2.16)$$

where A_T is the frontal area of the turbine extraction window, A is the channel cross-sectional area, W_T is the turbine's swept width (defined by $2 \cdot H_0$), H_T is the turbine's span, H is the water height, and W is the width between channel walls [6]. This blockage definition is illustrated in Fig. 2.4. Due to the passive nature of the turbine, the heaving amplitude cannot be determined prior to the experiments. In the present study, only the horizontal confinement is varied, while the water height and

turbine span remain constant. The different confinement levels are therefore defined beforehand by the normalized wall spacing W/c .

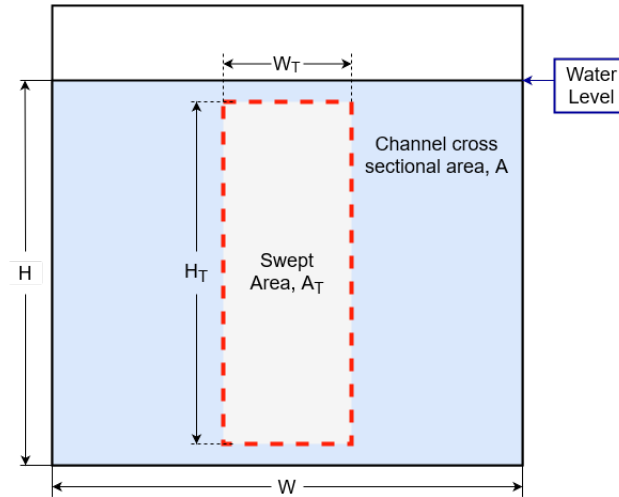


Figure 2.4: Illustration of the frontal areas defined in Eq. 2.16. H and W are the height and width of the flow cross section, respectively, and H_T and W_T are the foil's span and swept distance, respectively.

2.2 Experimental Setup

Water Flume

The experiments were conducted in a recirculating water channel in the Fluid Mechanics Laboratory at the University of Victoria. The test section of the tunnel has a cross section of 0.45 m by 0.45 m and a length of 2.5 m. The water height was 0.42 m for all experiments.

False Walls

To allow for variability in the blockage ratio, a “false wall” apparatus was installed in the water channel, as shown in Fig. 2.5. The drawings of this apparatus and instructions on its installation into the water channel can be found in Appendix A. The apparatus consists of two false walls that are 2 m in length, each made out of 0.5 in acrylic to allow optical access for the imaging techniques. Each wall has a sharp bevel at the leading edge to help suppress the leading edge separation region. The leading edge separation length was estimated to be approximately 3 in, which

is consistent with the findings of Fujiwara et al. [96], for a sharp bevelled leading edge. While leading edge geometries, such as an ellipsoidal edge [97,98], could have further suppressed the separation region, they were deemed unnecessary because the turbine was sufficiently downstream of the walls' leading edges where entrance effects would not impact the turbine. The walls are each fitted with four pins along the bottom edge, which fit into a false floor. The false floor has seven holes at each pin location to allow for seven confinement levels, in addition to the confinement level using the original tunnel wall spacing. The false walls are also fixed from the top by two drop-down brackets to ensure the walls do not move in the flow, and that they are held vertical.

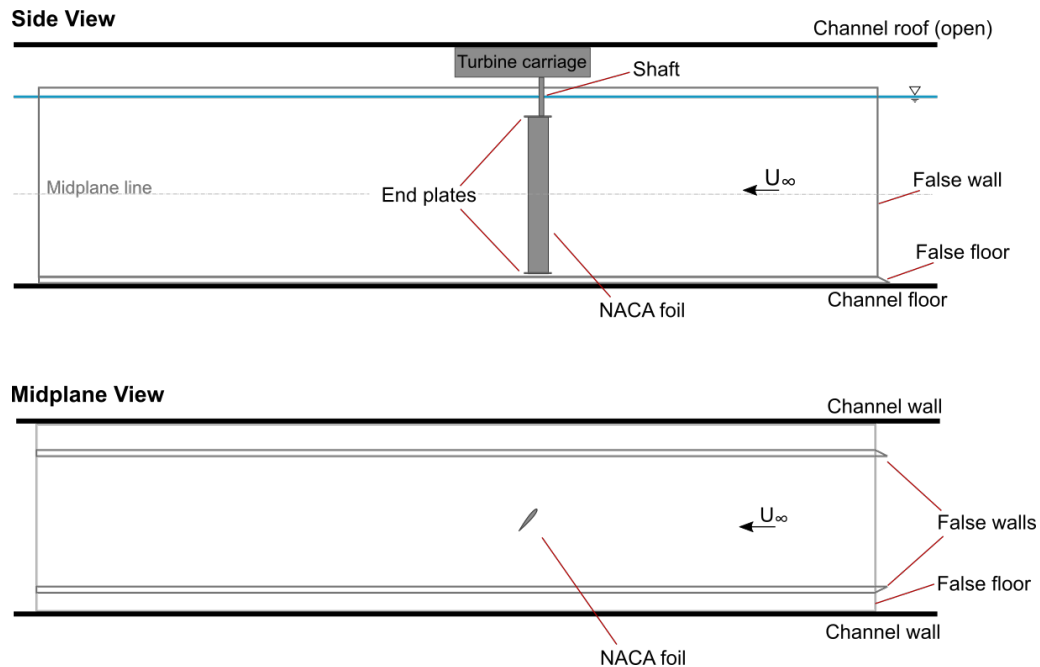


Figure 2.5: Schematic of the experimental setup, showing the false wall placement in the water channel.

The levels of confinement, defined prior to experiments as W/c , are defined in Tbl. 2.2.

Fully-Passive Oscillating-Foil Turbine

A NACA0015 foil with a 5 cm chord and 37.5 cm span ($AR = 7.5$) is attached to a pitching shaft, with the pitching axis at the third-chord point ($x_p/c = 1/3$). End plates are used to minimize tip losses and surface effects. The foil is fully submerged

in the water, with a 5 mm gap between the bottom plate and the channel floor, and only part of the pitching shaft submerged. The remainder of the prototype apparatus sits above the water. A carriage sits on linear guided roller bearings to allow for transverse motion in the heave DOF. Heave stiffness is introduced by connecting springs between the carriage and stationary frame. An eddy-current brake is used

Table 2.2: Levels of confinement W/c enforced by the different false wall positions.

Hole No.	W/c
0 ¹	9
1	7.25
2	6.75
3	6.25
4	5.75
5	5.25
6	4.75
7	4.25

as a damper for power take-off from the turbine. As discussed in Section 2.1, the damping coefficient can be adjusted by adjusting the height of the magnetic yoke with respect to the aluminum plate. The calibration of this damper is described in the thesis of Boudreau [5]. Similarly for the pitch DOF, springs are attached to the pitching shaft to allow for variable pitch stiffness. The prototype is also equipped with an eddy-current brake in the pitch DOF, but it is not used in this campaign.

¹Defined as no false walls present; the walls are the true walls of the water flume.

Chapter 3

Methodology

3.1 Freestream Velocity

The freestream velocity U_∞ was measured using planar PIV on a horizontal plane, fifteen chord lengths upstream of the pitch axis. Velocity was calculated and averaged over 100 images to obtain the average upstream velocity during the turbine's operation. Turbulence intensity of the inlet streamwise velocity fluctuations was below 1%.

The flow rate in the water channel can be controlled only by changing the frequency of its motor. At a given motor speed with constant water height, the freestream velocity between the false walls changed with changing wall spacing due to the change of flow resistance present. As the walls get closer, the turbine produces a higher flow resistance which forces more flow to travel through the space between the false walls and channel walls. To ensure that the freestream velocity was constant between confinement cases, multiple PIV tests were conducted at different motor frequency settings to select the proper frequency setting associated with a given confinement level. Freestream velocities between the different cases were within 0.5% of one another for all confinement cases.

3.2 Performance Data

Position data for the two DOFs was acquired using rotary encoders. The heave encoder used a rack-and-pinion to translate the transverse motion into rotary motion for the encoder to capture. Data was averaged over 90 cycles for each test, with a

sampling frequency of 83.3 Hz. The digital signals from the encoder were converted to analog signals between 0 and 5 V using a 14-bit digital-to-analog converter (DAC). The signals were then sampled with a NI USB-6218 data-acquisition board connected to a laptop.

The water temperature was measured using a standard glass thermometer. The temperature was used to estimate the water density and viscosity for parameter normalization, described in Section 2.

The viscous damping and Coulomb friction coefficients vary in the system, so these values were measured before and after each experiment to provide an average value for the data set. These parameters were estimated using the method of Feeny and Liang [99], which uses the logarithmic decrement in a free oscillation test. A full description of the testing specific to this turbine is provided in the thesis of Boudreau [5].

3.3 Flow Visualization

Planar (2D) PIV was used to visualize the turbine wake and to quantify the effect of the wake vorticity on the foil loading. The PIV setup is demonstrated in Fig. 3.1. The flow was seeded with 10 μm silver coated hollow glass spheres. The flow field was illuminated at the foil's mid-span by the Quantel Evergreen Nd:YAG 532 nm dual pulsed laser. Double frame images were captured with the LaVision XS 6M camera, using a 24 mm focal length lens. Data acquisition and vector field calculations were completed using the DaVis LaVision 10.1.2 software.

Planar PIV was deemed appropriate for the current study due to the quasi-2D nature of the flow, where there is negligible vorticity transport out of the data acquisition plane. A numerical study by Kinsey and Dumas [70] showed that the vorticity field at the mid-span of a foil with aspect ratio $AR=7$ with the use of endplates is nearly identical to the 2D flow field. Tomographic (3D) PIV is useful for cases in which non-negligible vorticity transport occurs in all three dimensions. For example, past research from our group by Lee [100] used tomographic PIV for 3D visualization of the OFT with a sweep angle, which introduced a spanwise component of vorticity.

Phase-averaged images were captured at five different positions in a turbine half-cycle, at $t^* = t/T = 0/10, 1/10, 2/10, 3/10, \text{ and } 4/10$. Each image is the average of 300 images, taken at the same point in the cycle based on heave position. Due to the passive nature of the turbine, cyclical variation was observed between the different

images. The kinematics of the turbine begin to change as the turbine operates due to the heating of the bearings, causing changes in the system's friction. According to Lee [100], the averaging of 300 images balanced these two effects, where the wake vorticity converged before beginning to change due to the bearings. The reader may refer to this work for further details on the convergence test and results.

The field of view of the PIV images was 174 x 218 mm, with a resolution of 2200 x 2752 pixels. The multi-pass cross-correlation was conducted with an initial interrogation window of 64 x 64 pixels to a final pass with 32 x 32 pixel interrogation windows, with 75% overlap between neighbouring windows. The final resolution of the vector field was 0.63 mm/vector. Due to the inherent bias and precision errors present in the PIV methodology, velocity uncertainty of up to 5% was observed.

The average velocity field, and the resulting vorticity fields were calculated directly in the DaVis software. The vorticity fields were then brought into MatLab, where convolution with a Gaussian kernel was applied to smooth the images.

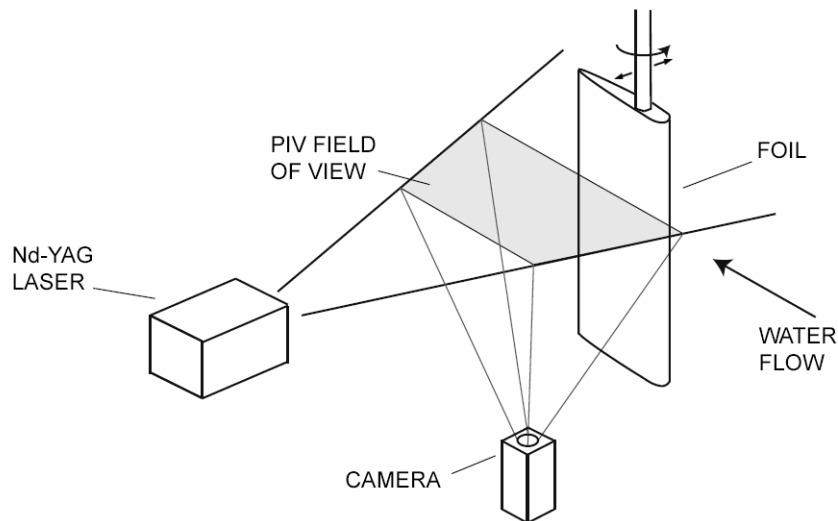


Figure 3.1: Schematic of the flow imaging set-up, showing the planar light sheet at the foil's mid-span, illuminated by the Nd-YAG laser, and the camera perpendicular to the data acquisition plane.

Chapter 4

Hydrokinetic performance of the fully-passive OFT

4.1 Baseline case of the OFT operating withing the true water flume walls

The baseline experiment was conducted in the water channel, without the false wall apparatus, for the confinement case $C0$ at normalized wall spacing $W/c = 9$. Following preliminary testing, a well performing case was selected at Re 19 000. This Re is in the range of past works conducted on the physical prototype in this water channel [1,94,100]. The parameters were intended to be similar to the case of Boudreau et al. [5], with modifications to account for increased friction in the prototype since its commissioning. Two different structural configurations were considered: zero pitch stiffness $k_{\theta}^* = 0$ (referred to as $K0$), and a case with a normalized pitch stiffness of $k_{\theta}^* = 0.056$ (referred to as $K056$). Investigating two configurations allowed for a comparison of how the systems responded under different structural configurations. This will ultimately help inform whether blockage corrections must account for structural differences, or if a general correction can be applied to the fully-passive OFT. The pitch stiffness used in the $K0$ configuration corresponded to the baseline case used in Boudreau et al., while the $K056$ configuration corresponded to a point where the highest efficiency was observed in Boudreau et al.'s parametric study [5]. The constant structural parameters are provided in Tbl. 4.1. The bearing friction throughout the experiments was variable, so an averaged value is provided. The key kinematic and performance metrics are summarized in Tbl. 4.2 for the $K0$ and $K056$ configura-

rations. With the turbine structural parameters held constant for each configuration, the lateral wall distance was varied by changing the wall position from *C1* through *C7* as described in Section 2.

Table 4.1: Normalized structural parameters held constant for all experiments. Two pitch stiffness configurations were used, as specified in the table.

Parameter	Value
Re	19000
m_h^*	3.65 ± 0.03
I_θ^*	0.098 ± 0.001
S^*	0.043 ± 0.001
$D_{h,e}^*$	1.09 ± 0.02
k_h^*	2.10 ± 0.02
k_θ^*	$0, 0.056 \pm 0.001$
$D_{h,v}^*$	0.083 ± 0.02
D_θ^*	0.006 ± 0.002
$C_{F_y \text{ Coulomb}}$	0.06 ± 0.01
$C_{M_{\text{Coulomb}}}$	0.006 ± 0.006
H/c	9

Table 4.2: Baseline performance of the turbine in the lowest confinement case for configurations *K0* and *K056*.

Performance Metric	<i>K0</i>	<i>K056</i>
f^*	0.132 ± 0.001	0.128 ± 0.001
ϕ	$100^\circ \pm 3^\circ$	$104^\circ \pm 3^\circ$
H_0^*	1.068 ± 0.002	1.22 ± 0.002
Θ_0	$87.5^\circ \pm 0.8^\circ$	$77.6^\circ \pm 0.8^\circ$
η_e	$25.4\% \pm 0.7\%$	$28.5\% \pm 0.7\%$
$\overline{C_{P_{h,e}}}$	0.74 ± 0.02	0.89 ± 0.02

The blockage ratios ε at the lowest confinement for the *K0* and *K056* configurations were 0.215 and 0.245 ± 0.002 , respectively. These values were calculated using Eq. 2.16, using geometric values from the foil and water channel, and the heave amplitude of the foil measured using the encoders.

The power extraction and relevant performance indicators, η_e and $\overline{C_{P_{h,e}}}$, are based on the power extraction from Eq. 2.9. The heave velocity used in this equation was calculated using a second order numerical derivative of the heave position data from the encoders.

4.2 Effects of lateral confinement on the turbine performance

The variable parameter in the experiments was the confinement level W/c . It was varied from the actual water channel confinement level of $W/c = 9$, to the highest level of confinement at $W/c = 4.25$, imposed by the false walls. Recall, confinement level W/c is needed to define the wall distance prior to experiments, since the blockage ratio ε is based on the heave amplitude H_0 which varies in response to the fluid structure interaction. Fig. 4.1 shows the blockage ratio that arose from each confinement case for both the *K0* and *K056* configurations. The general trend for each configuration was similar, however, the *K056* configuration reached larger ε values for a given wall spacing, compared to the *K0* configuration. Since the water level, lateral wall spacing, and foil geometry was held constant for a given confinement case, this means that the *K056* configuration reached larger heaving amplitudes than the *K0* configuration.

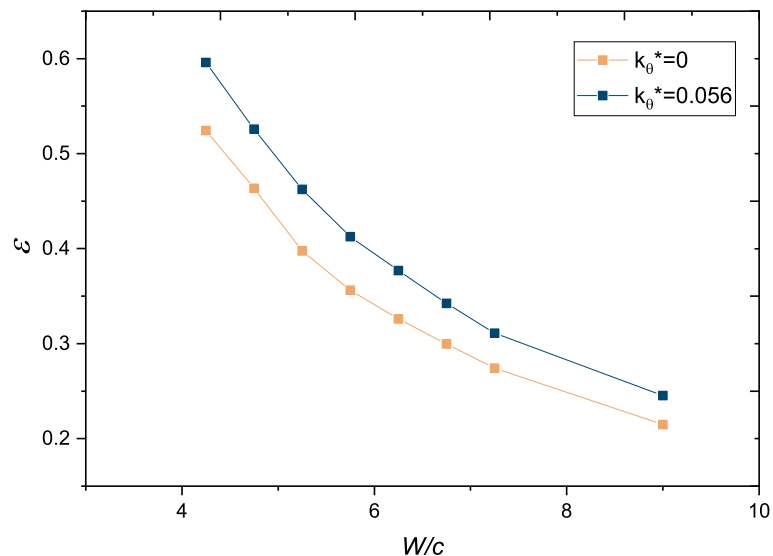


Figure 4.1: Blockage ratio ε as a function of confinement level W/c , for the *K0* and *K056* configurations.

The key performance metrics, η and C_p , are plotted as functions of ε in Fig. 4.2. Consistent with the parametric study of Boudreau et al. [1], the efficiency and power coefficient were greater overall for the configuration with added pitch stiffness (*K056*) than the configuration with zero pitch stiffness (*K0*).

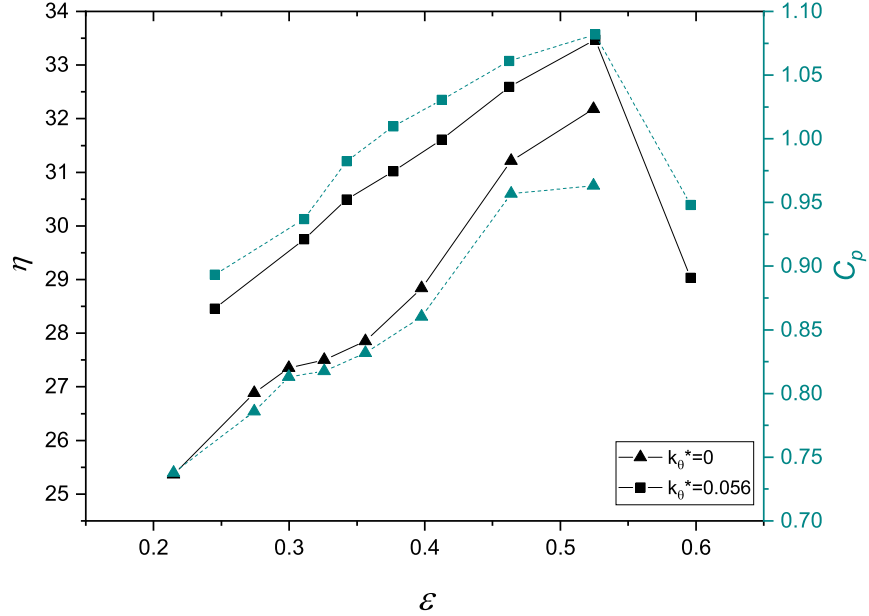


Figure 4.2: Efficiency η and power coefficient C_p functions of blockage ratio ε , for the *K0* and *K056* configurations.

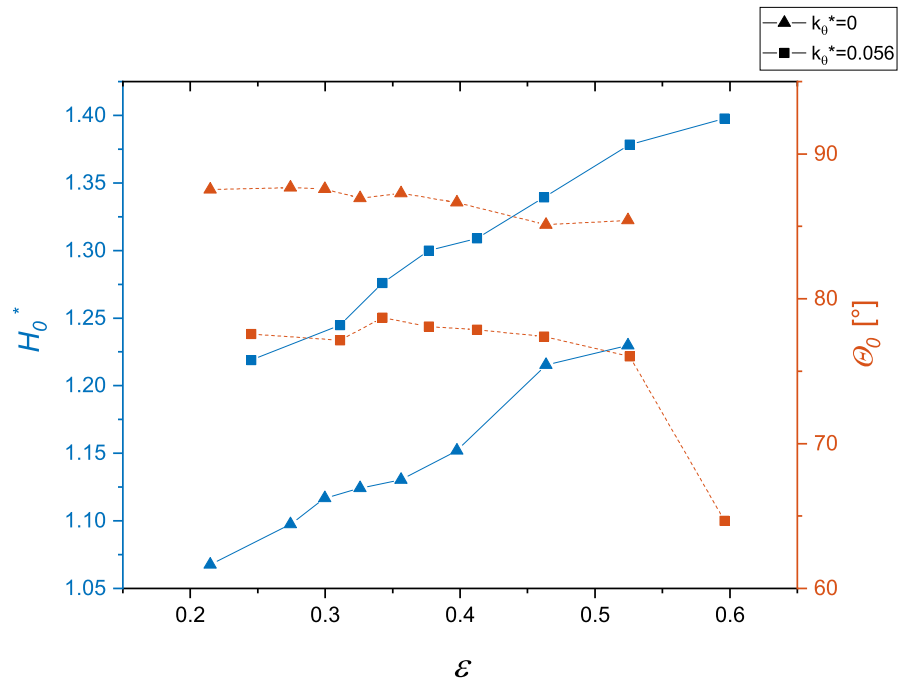
For both configurations, there was an overall increase in the performance metrics as the blockage ratio increased, up to a critical level. The power coefficient began to plateau at $\varepsilon \approx 0.45$ for both configurations. Since the *K056* configuration reached a higher blockage ratio for the same wall spacing, we observed that after the power coefficient plateaued, both the efficiency and power coefficient dropped off rapidly beyond $\varepsilon \approx 0.52$. Given that the configurations were tested within the same confinement wall spacing, it was concluded that the *K0* configuration may operate within higher confinement regions than the *K056* configuration before it becomes detrimental to the turbine's energy harvesting capability. This is an important conclusion for planning where and how these turbines may be deployed.

Curve fitting is provided in Section 4.2.1 to further investigate the performance trends, but for now it is worth observing that the efficiency trend, specifically for the *K056* configuration, was close to linear. This is consistent with trends observed for the fully constrained activation mode of the OFT by Gauthier [6].

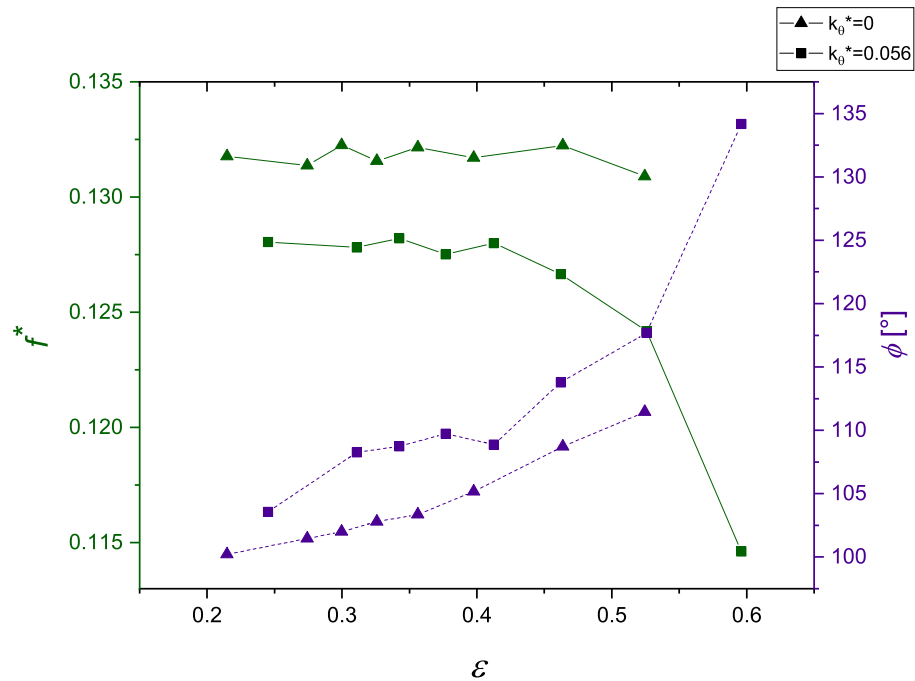
Past confinement studies on the active OFT have attributed the change in performance to the change in oncoming flow, leading to an increase in the effective angle of attack, in addition to providing more dynamic pressure and kinetic energy flux to the turbine. The fully-passive OFT is more complex since the foil kinematics can change with changing environmental conditions. The performance trends can therefore be further explained by relating them to the kinematic parameter trends. The key kinematic parameters including the heave amplitude H_0^* , pitch amplitude Θ_0 , reduced frequency f^* , and phase lag ϕ , are plotted with respect to the blockage ratio in Fig. 4.3.

First, we observe the range of blockage ratio for which performance increased in both configurations (i.e. $\varepsilon < 0.52$). In this range, the heave amplitude, plotted in Fig. 4.3(a) increased with increasing blockage ratio for both configurations. This increase in the heave amplitude provided the foil access to a larger cross-sectional flow area for energy extraction. This accounts for net energy extraction increase, and thus the increase in the power coefficient. At the same time, the reduced frequency, plotted in Fig. 4.3(b), remained relatively constant in this range of blockage ratios. The increase in heave amplitude while maintaining a constant frequency led to an increase in the heave velocity. As shown in Eq. 2.9, the extracted power is proportional to the square of heave velocity, and therefore also increased. This accounts for the observed increase in efficiency shown in Fig. 4.2. The phase lag for both configurations is between approximately 100 and 110 degrees. From McKinney and DeLaurier's [32] pioneering work, the optimal phase lag should be between 90 and 110 degrees for both high efficiency and high power coefficient. This also adds to the explanation of why the turbine operates in an efficient regime for this range of blockage ratios.

The second region of interest is at the highest level of confinement, where the power extraction plateaued for the $K0$ configuration, and the power extraction dropped off significantly for the $K056$ configuration. Above $\varepsilon = 0.52$ for $K056$, the phase lag between the DOFs rapidly increased, as shown in Fig. 4.3(b). This change in the phase resulted in an inefficient transfer of energy between the pitching and heaving DOFs. Consequently, the largest flow-induced forces attained during an oscillation cycle were not well synchronized with the maximum heaving velocity. From Eq. 1.4, this is a requirement for a high-performing energy harvester. Although there was not a dramatic increase in phase lag at the highest confinement level for $K0$, the phase lag still showed a steady increase, moving towards an inefficient operation regime as the power coefficient began to plateau. Another key feature in the kinematic plots is



(a)



(b)

Figure 4.3: Kinematic parameters of the OFT as functions of the blockage ratio ε . (a) normalized heave amplitude H_0^* , and pitch amplitude Θ_0 . (b) Reduced frequency f^* and phase lag ϕ .

the pitch amplitude. This is an important parameter because it is an indicator of the effective angle of attack, which is directly related to the formation of the LEV and, consequently, the strength of the lift forces acting on the foil. At the highest level of confinement in the *K056* configuration, the pitch amplitude dropped off quickly. This is again an indication that the LEV was not able to form very strongly and that this case was subjected to lower hydrodynamic forces than lower confinement cases. This is confirmed in the Section 5, where the wake structures are assessed qualitatively and quantitatively.

Due to the passive nature of the turbine, cyclic variations were observed in the kinematics and performance, as presented in Appendix B. In general, the OFT experienced larger standard deviations between cycles as the confinement increased. This suggests that the turbine moved toward a more erratic operation mode with confinement, which is not suitable for energy extraction.

Uncertainty in the turbine's performance arose from uncertainty in the position data, damping coefficients, stiffness values, and structural dimensions. The main sources of uncertainty in the position measurements included the uncertainty in the encoder measurements and the digital-to-analog converter. For the heave DOF, there was additional uncertainty due to the backlash in the rack-and-pinion translation system. The heave velocity was calculated using the heave position, numerically differentiated by data acquisition time. The sampling rate of 83.3 Hz introduced a small uncertainty into the heave velocity value. Damping values from the eddy-current damper were calculated using linear interpolation of calibrated values, producing inherent uncertainty from interpolation. Finally, load cell and caliper uncertainty lead to uncertainty in stiffness values of the springs, and dimensions of the turbine blade, respectively. These uncertainties compounded to produce uncertainty in the final efficiency and power coefficient values, which was limited to a maximum of 2.75% and 2.73%, respectively. A summary of the uncertainty in all kinematic parameters for each experiment is provided in Appendix C.

4.2.1 Blockage Corrections and Trends

In this section, the performance data is first fit to curves using linear regression analysis. Polynomial curves were used to precisely describe the data within the investigated and nearby parametric region. To extrapolate to lower blockage ratios than the base level blockage present in the water channel, linear fits are provided. The data is then

compared against existing blockage corrections to determine whether existing corrections are adequate for the fully-passive configuration of the OFT, or if further work should be recommended to extend the blockage corrections.

Curve Fits

Here, general curve fits are provided to describe the performance trends and to help predict expected trajectories of what the parameters will look like outside of the experimental confinement level space investigated in this campaign. The intention of this section is to provide insight into the behavior of the data, which may aid to eventually form a mathematical model for the turbine's performance as a function of blockage. It is also valuable to capture the data trends for validation of computational studies, which are better equipped to extend the current parametric space, allowing for the generation of blockage correction models for the fully-passive OFT. This curve-fitting approach is limited and has certainty only in the range of parameters explored in this study, with the fully-passive turbine operating under the structural and flow parameters listed in Tbl. 4.1, and confinement levels listed in 2.2 by changing the lateral position of the walls.

Curve fitting was conducted using the Matlab curve fitting toolbox, using least-squares linear regression formulations. The best fits are provided in this section, with other investigated curve fits provided in Appendix D. This appendix includes fitted parameters for different curve fit shapes, with their associated confidence bounds, as well as a comparison of the plotted curves.

First, the trend of how the blockage ratio ε changed with confinement level W/c was investigated for each configuration. From Fig. 4.1, the trends appeared similar, but shifted about the ε -axis. The trends could therefore be described using a single equation,

$$\varepsilon = 0.830 - 0.371 \left(\frac{W}{c} \right) + 4.75\varepsilon_0 + 0.0520 \left(\frac{W}{c} \right)^2 - 0.683 \left(\frac{W}{c} \right) \varepsilon_0 - 0.00233 \left(\frac{W}{c} \right)^3 + 0.0291 \left(\frac{W}{c} \right)^2 \varepsilon_0, \quad (4.1)$$

where ε_0 is the blockage ratio at $C0$ ($W/c = 9$). This fit follows a third order W/c and first order ε_0 polynomial fit, which is the maximum order permitted using the data points collected in this study. This fit provided a good agreement for both models with an R^2 value above 0.99. This trend is plotted for the $K0$ and $K056$

configurations in Fig. 4.4, with $\varepsilon_0 = 0.215$ and 0.245 , respectively.

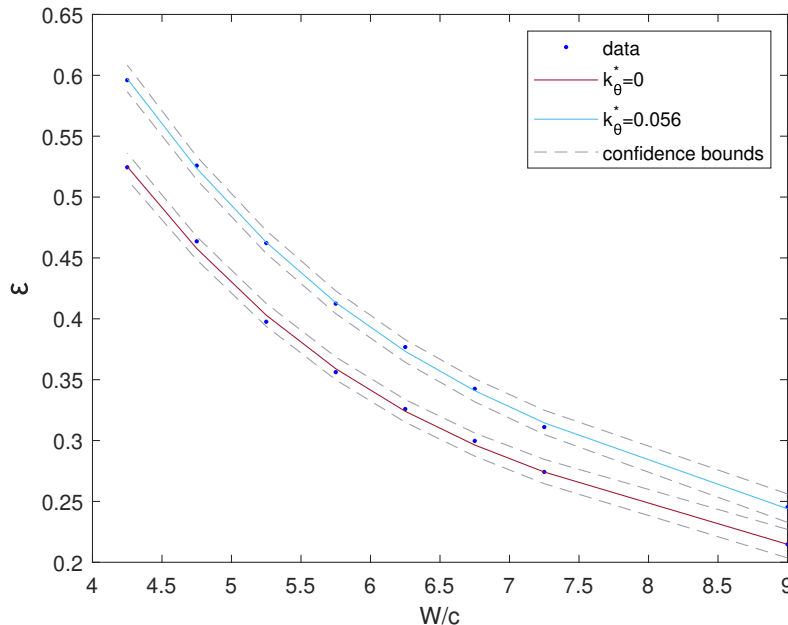


Figure 4.4: Plot of the curve fit Eq. 4.1 for blockage ratio ε vs. confinement level W/c for configurations *K0* and *K056*. 95% confidence bounds are indicated by dashed lines.

The ability to model both configurations in a single curve-fit is encouraging, since it indicates that the blockage ratio can be predicted for a given wall spacing, for both configurations tested. This should be further investigated for more structural configurations in later works, to verify that the blockage ratio follows the same trend shown here.

The cubic nature of the blockage ratio ε with respect to the confinement level W/c demonstrates that the blockage ratio began to rapidly increase when the turbine operated in close wall proximity. This sharp increase in blockage ratio was a result of two factors: (1) the wall spacing getting closer acted to decrease the area of the overall flow window, and (2) the increase in heave amplitude, as shown in Fig. 4.3a, acting to increase the overall swept area of the turbine. This means that the numerator of Eq. 2.16 increased while the denominator decreased, demonstrating that the change in blockage ratio was non-linear.

Unlike the blockage ratio trends, the trends of the performance curves for both configurations did not follow the same shape and were therefore fit with different

curves. The power coefficient as a function of blockage ratio for configurations *K0* and *K056* were best described using fourth order polynomial fits within the investigated region:

$$C_p = -227\varepsilon^4 + 329.8\varepsilon^3 - 173.8\varepsilon^2 + 40.04\varepsilon - 2.63; \quad \varepsilon(.215, .524), \quad (4.2)$$

$$C_p = -77.8\varepsilon^4 + 109.4\varepsilon^3 - 56.99\varepsilon^2 + 13.84\varepsilon - 0.4088; \quad \varepsilon(.245, .596). \quad (4.3)$$

The R^2 values of the two curve fits were 0.9927 and 0.9986, respectively. The fits were chosen based on the goodness of fit from the R^2 values, as well as based on physical resemblance from the plotted curves. Higher order polynomial fits for both configurations caused the C_p values to decrease with increasing ε in the region immediately below $\varepsilon = 0.20$, which is unphysical. The higher order models are, however, limited to the experimental space and nearby region. From the above equations, we see that the intercept for each curve is negative. This indicated negative performance in the unconfined configuration, which is again unphysical. To extrapolate data to the region of confinement below the base level provided by the water channel, simple linear models were applied in the region from *C0* to *C6*, before the performance began to plateau. The linear curves for the *K0* and *K056* configurations had R^2 values of 0.9506 and 0.9616, respectively, and are provided as:

$$C_p = 0.8104\varepsilon + 0.5559; \quad \varepsilon(.215, .463), \quad (4.4)$$

$$C_p = 0.6987\varepsilon + 0.7323; \quad \varepsilon(.245, .526). \quad (4.5)$$

Using the intercepts from Eqs. 4.4 and 4.5, the predicted unconfined values of the power coefficient for the *K0* and *K056* configurations were $C_p = 0.56$ and 0.73 . Plots of the fitted C_p curves and confidence bounds are provided in Fig. 4.5.

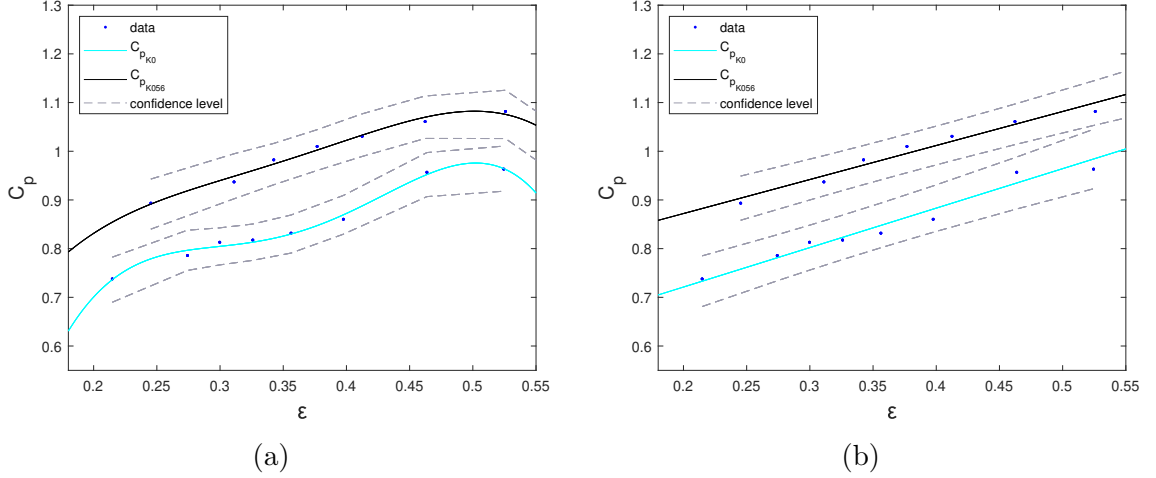


Figure 4.5: Curve fits for the power coefficient C_p as a function of blockage ratio ε with 95% confidence bounds. (a) Polynomial fits for the $K0$ and $K056$ configurations using Eqs. 4.2 and 4.3. (b) Linear fits for the $K0$ and $K056$ configurations using Eqs. 4.4 and 4.5.

Similar to the power coefficient curve fits, the efficiency was fit using higher order polynomials to closely portray the performance trend in the investigated parametric space, then fitted with simple linear fits to extrapolate to lower blockage ratios.

The curves for η versus ε were fit using a fifth order polynomial for the $K0$ configuration, and a fourth order fit for the $K056$ configuration:

$$\eta = -1.78E04\varepsilon^5 + 2.752E04\varepsilon^4 - 1.583E04\varepsilon^3 + 4140\varepsilon^2 - 450.1\varepsilon + 37.49; \quad \varepsilon(.215, .524), \quad (4.6)$$

$$\eta = -4475\varepsilon^4 + 6816\varepsilon^3 + -3813\varepsilon^2 + 945.6\varepsilon + -58.5; \quad \varepsilon(.245, .596). \quad (4.7)$$

The fits provide R^2 values of 0.9996 and 0.9934, respectively. Linear fits are provided for the $K0$ and $K056$ configurations in the region from $C0$ to $C6$, with R^2 values of 0.9551 and 0.9953:

$$\eta = 21.62\varepsilon + 20.65; \quad \varepsilon(.215, .463), \quad (4.8)$$

$$\eta = 17.96\varepsilon + 24.19; \quad \varepsilon(.245, .526). \quad (4.9)$$

From the linear fits, the unconfined efficiency values for the $K0$ and $K056$ configurations are 20.65% and 24.19%, respectively. The polynomial and linear efficiency fits with confidence bounds are provided in Fig. 4.6.

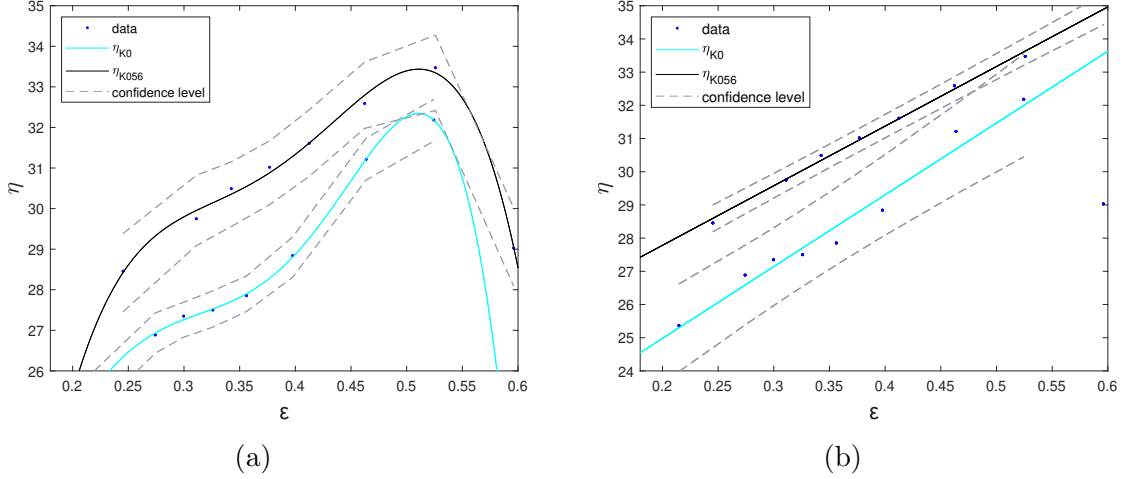


Figure 4.6: Curve fits for the efficiency η as a function of blockage ratio ϵ with 95% confidence bounds. (a) Polynomial fits for the $K0$ and $K056$ configurations using Eqs. 4.6 and 4.7. (b) Linear fits for the $K0$ and $K056$ configurations using Eqs. 4.8 and 4.9.

Blockage Correction

Two blockage corrections were tested to determine whether they were directly applicable to the fully-passive OFT, or if further studies must be recommended to extend existing blockage corrections. The models compare the turbine operating in confinement to a turbine operating in an unconfined environment to correct the performance values to the values observed in the unconfined space. Therefore, the corrected C_p values should all correspond to a constant, unconfined value. Further, the corrected values should correspond roughly to the C_p value at $\epsilon = 0$ from the linear curve fits presented in Eqs. 4.4 and 4.5.

First, the Barnsley and Wellicome (BW) correction [101] was applied, which was popularized by Bahaj et al. [102] and further utilized in works such as Kinsey et al. [83] and Gauthier et al. [6]. It is an analytical correction based on conservation of mass, energy, and momentum applied to flow around an actuator disk within confining walls. It provides a velocity correction which can then be used to correct power coefficient, which has a cubic relation to velocity. A derivation of the method

can be found in Gauthier et al. [6] and Kinsey et al. [83]. A summary of the key equations and the implementation method is provided in Appendix E.

The second correction comes from the work of Housby et al. [7]. It follows the same framework of the BW correction, but has two key distinctions: (1) the channel contains a free surface, rather than being bound at all surrounding walls, and (2) the analysis considers mixing in the wake downstream of the turbine.

The plots of the actual and corrected power coefficient data using both correction methodologies are provided in Fig. 4.7. Both models produced nearly identical correction data, which did not prove to be appropriate corrections for the turbine due to their correction values, and the shape of the curves. The change in height predicted by the Housby correction was approximately 1 cm. Given this change with respect to the total flow window area, it makes sense that it was an insignificant change in the analysis compared to the BW correction. This free surface correction also only corrected for an average downstream surface height, but the wake of the actual turbine was not uniform. The free surface addition to the BW correction therefore provided insignificant modifications to the performance correction.

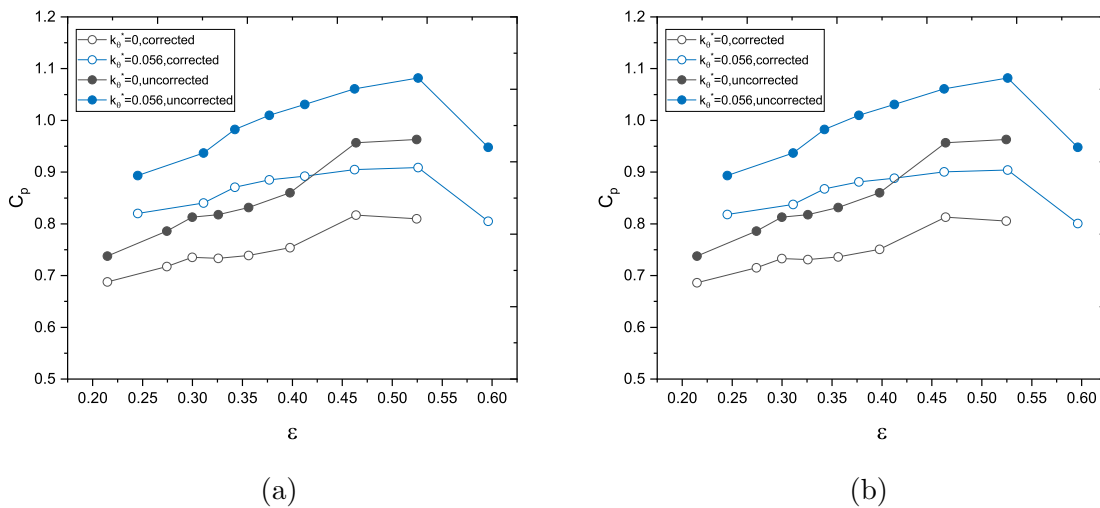


Figure 4.7: Comparison of the C_p curve data with the corrected data using the (a) BW correction. (b) Housby correction.

The average corrected C_p value from both models was approximately 0.75, with values ranging from 0.69 to 0.86 for the *K0* configuration. Comparing the average corrected C_p to that predicted by the linear data trend, $C_p = 0.56$, gave 33.8% error. Comparing the predicted value by the adjusted C_p from the least confined point, $C_p = 0.688$, gave a percent error of 22.8%.

The average corrected C_p value from both models was 0.86-0.87, with values ranging from 0.82 to 0.91 for the *K056* configuration. Comparing the average corrected C_p to that predicted by the linear data trend, $C_p = 0.73$, gave 18.6% error. Comparing the predicted value by the adjusted C_p from the least confined point, $C_p = 0.820$, gave a percent error of 12.0%.

This demonstrated that the *K056* configuration could be better predicted by the blockage corrections than the *K0* configuration. However, both configurations demonstrated high percentage errors overall. A lower percent error was also observed at lower confinements, showing that the blockage corrections became less applicable as blockage increased.

The shape of the correction curves in Fig. 4.7 was another indicator that the blockage correction models were poor fits for the fully-passive OFT. Since the models correct the values to the equivalent value at $\varepsilon = 0$, all values should be the same, meaning that the resulting curve should be a flat line. The corrected curves had shallower slopes than the actual data curves. Although these curves were closer to constant than the original uncorrected curves, they appeared related to the original curves, as they followed the same general shape. In general, the profiles were flatter for lower blockage ratios, again indicating that the blockage corrections were more applicable at lower confinement level and became less applicable at high confinement.

Potential reasoning for the blockage corrections not being applicable to the fully-passive OFT include the fact that unlike the active OFT, the kinematics of the fully-passive OFT change at each blockage ratio, so the cases were not directly comparable due to changes in the turbine's operation.

Overall, it is shown that the existing blockage corrections relying on linear momentum theory are not directly applicable to the fully-passive OFT. This area should be further investigated to provide corrections to the fully-passive OFT performance. A limitation of the current work was that the base level confinement of the water channel was quite high, meaning that there was no unconfined experimental case to compare to. The author recommends extending this study using CFD to allow a larger level of confinement levels to be investigated. With this extended confinement

data, existing blockage corrections may be extended. This is further discussed in Section 6.1 of this thesis.

Chapter 5

Quantitative Flow Patterns

5.1 Two-dimensional Flow Patterns

The normalized out-of-plane vorticity fields at several phases of the OFT's oscillation cycle are shown at three confinement levels in Figs. 5.1 and 5.2, for the *K0* and *K056* configurations, respectively. The inflow direction is from top to bottom in each plot. One half of the oscillation cycle is represented for each confinement level, at the normalized heave phases of $t^* = t/T = 0/10, 1/10, 2/10, 3/10$ and $4/10$. Only the first half of the oscillation cycle is shown since the foil oscillation and associated flow patterns were symmetric during the second half of the oscillation period. Imaging was conducted at confinement levels *C1*, *C4* and *C7* for both configurations. These cases were chosen for imaging to compare the flow fields for a relatively low confinement level, a medium confinement level where the performance increased, and the highest confinement level where performance began to plateau.

The dominant flow feature in the wake of the OFT was the LEV, which was the main contributor to the lift and moment forces acting on the foil, resulting in the self-sustained limit-cycle oscillations. The following discussion focuses on the evolution and shedding of the LEV into the wake at each phase, and compares the evolution between different cases.

We first observe the wake structures for the *K0* configuration, shown in Fig. 5.1. For this configuration, the confinement levels *C1*, *C4* and *C7* corresponded to $\varepsilon = 0.27$, $\varepsilon = 0.36$, and $\varepsilon = 0.52$, respectively. At phase $t^*=0/10$, the negative (clockwise) rotating LEV, labelled *A*, began to form for the *C1* and *C4* confinement levels. There is an important distinction between these two images, where the pitch

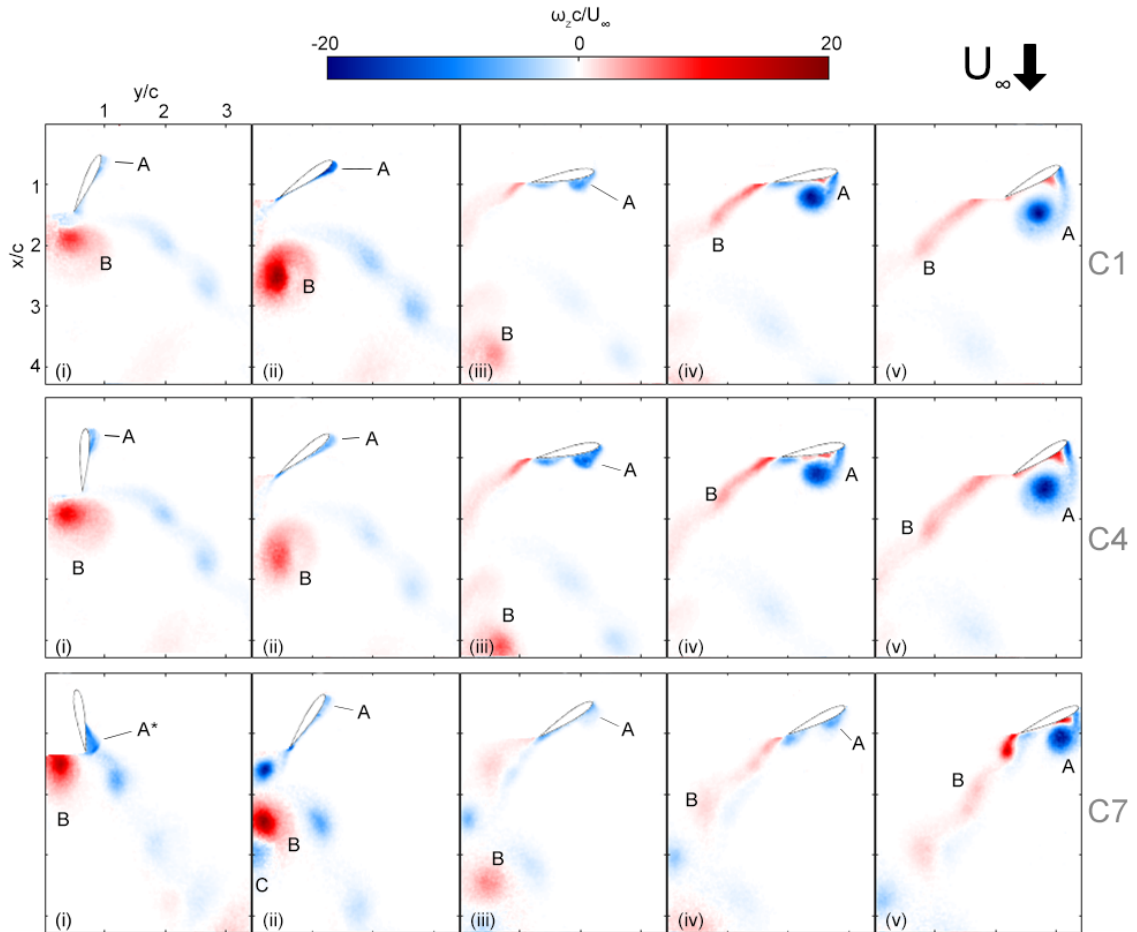


Figure 5.1: Patterns of the phase-averaged dimensionless out-of-plane vorticity at sequential phases (i) $t^* = 0/10$, (ii) $t^* = 1/10$, (iii) $t^* = 2/10$, (iv) $t^* = 3/10$, (v) $t^* = 4/10$ for the $K0$ configuration. The top, middle and bottom rows correspond to confinement levels $C1$, $C4$, and $C7$, respectively, as defined in Tbl. 2.2. The inflow velocity magnitude $U_\infty = 0.38$ m/s is directed from top to bottom. The LEV is labelled A and the shed vortex from the previous half-cycle plus the TEV from the current half-cycle is labelled B. A^* denotes the trailing edge vortex from the previous half-cycle, where the new LEV has not yet formed.

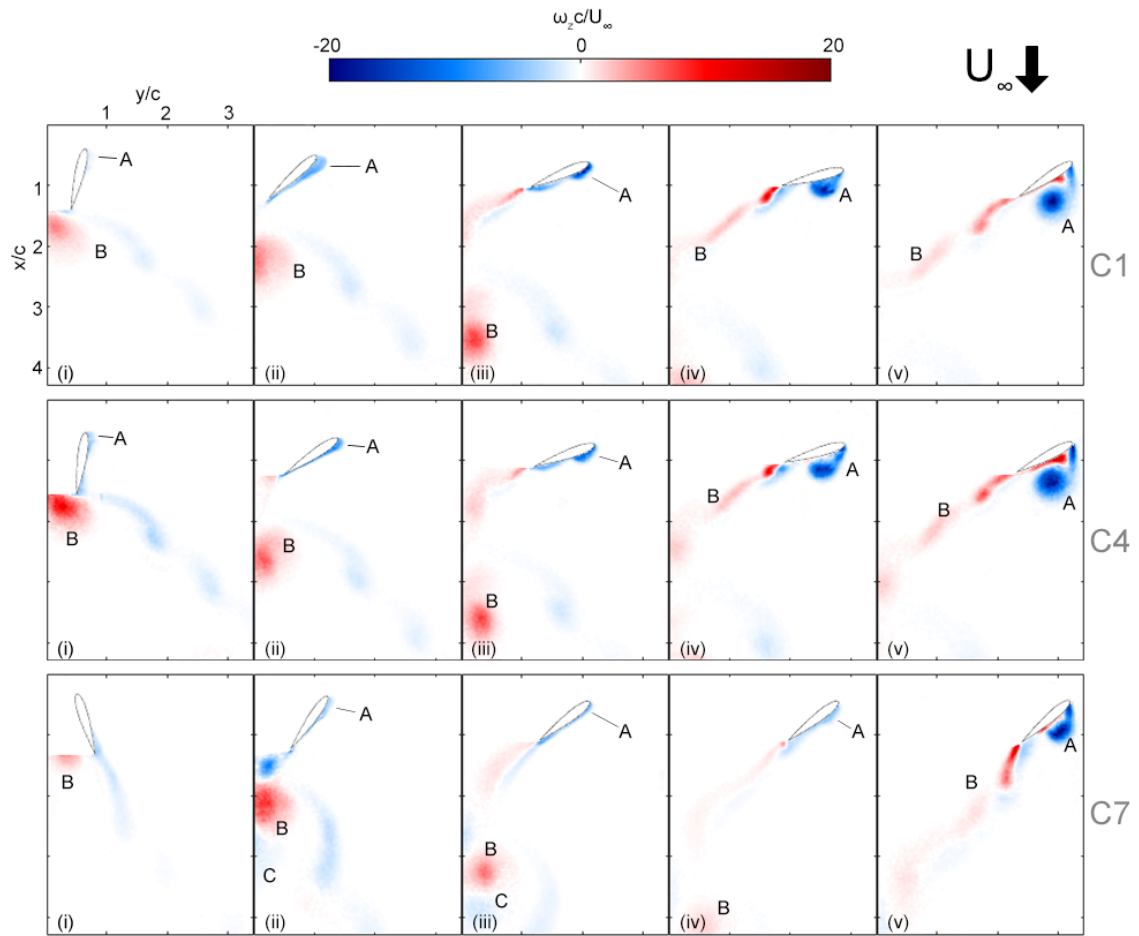


Figure 5.2: Patterns of the phase-averaged dimensionless out-of-plane vorticity at sequential phases (i) $t^* = 0/10$, (ii) $t^* = 1/10$, (iii) $t^* = 2/10$, (iv) $t^* = 3/10$, (v) $t^* = 4/10$ for the *K056* configuration. The top, middle and bottom rows correspond to confinement levels *C1*, *C4*, and *C7*, respectively, as defined in Tbl. 2.2. The inflow velocity magnitude $U_\infty = 0.38$ m/s is directed from top to bottom. The LEV is labelled A and the shed vortex from the previous half-cycle is labelled B.

position was different. This contributed to changes in the OFT operation due to the change in timing of the flow forces with the position and velocity of the degrees of freedom. The *C7* case showed the biggest discrepancy, where not only was the pitch position quite different, but the flow features were significantly different as well. In this case, the LEV had not yet begun to form, and the trailing edge vortex (TEV) from the previous half cycle had not yet convected away from the foil. Once again, the timing between the flow forces and the oscillation cycle are key for a well performing turbine. This frame showed poor timing between the flow evolution and the foil kinematics, which contributed to the degraded performance observed in Fig. 4.2.

At phases $t^* = 1/10$ to $t^* = 2/10$, the wake was qualitatively similar for cases *C1* and *C4*. The LEV continued to grow in size and magnitude, while the LEV from the previous half-cycle, vortex *B*, convected downstream. The pitch angle was also quite similar at these phases. Again, the *C7* case was qualitatively very different. First, the foil reached a much smaller pitch angle than in the previous two cases. Due to this, the LEV was much smaller in extent and in strength, and therefore lower overall lift forces acted on the foil. Another key feature was the formation of clockwise rotating vortex *C* at the wall, which interacted with the shed vorticity from the foil. This feature has also been observed in past works for various confined flows. Rehimí et al. [103] observed a counter-rotating vortex formed and advected downstream at the wall when flow passed over a cylinder in high confinement, which opposed the von Kármán vortex shed from the cylinder. Karakas and Fenercioglu [92] and Hoke et al. [93] investigated on oscillating-plate operating with close wall proximity. They found that at the closest wall proximity in their study, a counter-rotating vortex formed at the side wall and interacted with the detached vortex from the plate. They attributed the degradation of performance at very close wall spacing to the interaction between the vorticity formed by the plate and that at the wall. This is consistent with what was observed in the current PIV imaging, and the decrease in performance observed at *C7* in this study.

At phase $t^*=3/10$, the flow evolution and pitch angle were once again very similar for the *C1* and *C4* cases. The LEV began to detach from the leading edge, with the vortex core lifting from the foil surface. The LEV in case *C7* had not yet detached from the surface, again illustrating the poor timing between the flow evolution and the foil oscillation cycle. The strength and extent of the vortex at this point were both much smaller than for cases *C1* and *C4*.

Finally, at phase $t^*=4/10$, the LEV was detached for all three confinement cases,

and the pitch angle decreased from phase $t^*=3/10$ as the foil moved toward pitch reversal into the symmetric half-cycle. The pitch angle and wake patterns were very similar between $C1$ and $C4$, but once again differ for the $C7$ case. Here, the LEV was much smaller in extent as it had grown and detached later in the cycle compared with the other cases. For the $C7$ case, the strongest LEV existed in the last frame at $t^*=4/10$, while the strongest LEV existed at $t^*=3/10$ for the less confined cases. This illustrates that the highest flow forces were not acting on the foil at the optimal times. The ideal timing would occur closer to the mid-stroke, where the highest heave velocity existed, to optimize the power extraction.

Overall, the flow visualization demonstrated why a performance plateau was observed for the highest confinement case, $C7$. The key effect contributing to the loss in performance was the generation of a counter-rotating vortex at the wall which interacted with the shed vorticity from the oscillating-foil. This led to inefficient timing between the flow feature evolution and the oscillation cycle.

We now compare the above observations with the flow fields of the $K056$ configuration, shown in Fig. 5.2. Here, the confinement cases $C1$, $C4$ and $C7$ corresponded to $\varepsilon = 0.31$, $\varepsilon = 0.41$ and $\varepsilon = 0.60$. Overall, the same key observations made for the $K0$ configuration held for the $K056$ configuration: the flow fields in cases $C1$ and $C4$ were very similar with minor distinctions in the pitch angle. At phases $t^*=3/10$ and $t^*=4/10$, the LEV had grown stronger and to a larger extent for the $C4$ case than for the $C1$ case. At $t^*=3/10$, the LEV has detached for case $C4$, but remains attached for case $C1$. This change in timing of the flow force acting on the foil likely explains the enhanced performance for the $C4$ case compared to the $C1$ case. In the case $C7$ images, a large difference in the pitch angle was once again observed, compared to the other confinement cases. The pitch angle in the first frame ($t^*=0$) was larger than that observed in the $K0$ configuration. This points to the fact that the phase lag was outside the optimal range for a high performing turbine, and further explains why the $K056$ configuration experienced a drop in performance at confinement $C7$, while the $K0$ configuration only experienced a plateau. Consistent with the $K0$ configuration, the flow features developed weaker and at a slower rate than for cases $C1$ and $C4$. Vortex C was formed at the wall, and interacted with the shed vorticity from the foil as it did in the previous configuration.

Overall, the performance of the $K056$ configuration was higher than for the $K0$ configuration for every confinement case except for the highest confinement level, $C7$. Comparing the flow structures of Fig. 5.1 and 5.2, we observe that the development

and shedding of the LEV was delayed for *K056* compared to *K0*. Having the low pressure vortex core close to the foil's surface during the heaving motion provided a larger lift force on the foil, which accounted for the increase in performance. Indeed, past works have found that delaying the shedding of the LEV is beneficial for turbine performance (e.g., [100]). At confinement *C7*, the LEV developed even later in the cycle than in the *K0* configuration, and exhibited a much smaller strength. This also accounted for the larger performance decrease observed for the *K056* configuration than for the *K0* configuration at the same confinement level.

Inferences made in the previous section have been confirmed visually through the use of PIV in this section. The enhanced performance between *C1* and *C4* for both configurations resulted from well timed forces induced by the flow on the foil. Improper timing between the two DOFs and the flow features also proved to be the main factor in the decreased performance for confinement *C7*. Additionally, the counter-rotating vortex formed at the wall was an important feature which arose at high confinement and interacted negatively with the vorticity shed from the foil.

Results in this section were observed qualitatively using flow imaging, but further confirmation of the influence of wake vorticity on foil performance will be provided in the following section using the quantitative PIV data.

5.2 Contributions of the shed vorticity to the instantaneous force on the foil

Using the PIV data, the circulation in the wake was related to the forces on the foil using a concept based on hydrodynamic impulse, introduced by Lighthill [104] and Lamb [105]. Specifically, the flow-induced force acting on the foil is defined as

$$\mathbf{F} = \frac{d}{dt} \left[\frac{1}{2} \rho \int \mathbf{r} \times \boldsymbol{\omega} dV \right], \quad (5.1)$$

where $\boldsymbol{\omega}$ is vorticity, and $\int \mathbf{r} \times \boldsymbol{\omega} dV$ is the integral of the moment of vorticity with respect to the point of force application - in this case, the pitching axis. This equation requires that the volume integral includes all shed vorticity; however, this is not possible given the limited data acquisition plane. Therefore, this study gives an approximation of the moment of vorticity by considering the shed vorticity in the near-wake of the foil, only. Since the temporal resolution of the PIV data was not

adequate for calculation of the time derivative in Eq. 5.1, the loading on the foil was characterized by the normalized moments of vorticity acting in the streamwise (x) and lateral (y) directions. The normalized integral of the moment of vorticity acting in the x-direction is expressed as

$$(M_\omega)_x = +\frac{1}{U_\infty^2 c} \int y\omega_z dA, \quad (5.2)$$

and the normalized integral of the moment of vorticity acting in the y-direction is expressed as

$$(M_\omega)_y = -\frac{1}{U_\infty^2 c} \int x\omega_z dA. \quad (5.3)$$

The streamwise and the lateral force coefficients are then represented by the time derivatives of the normalized moments of vorticity as

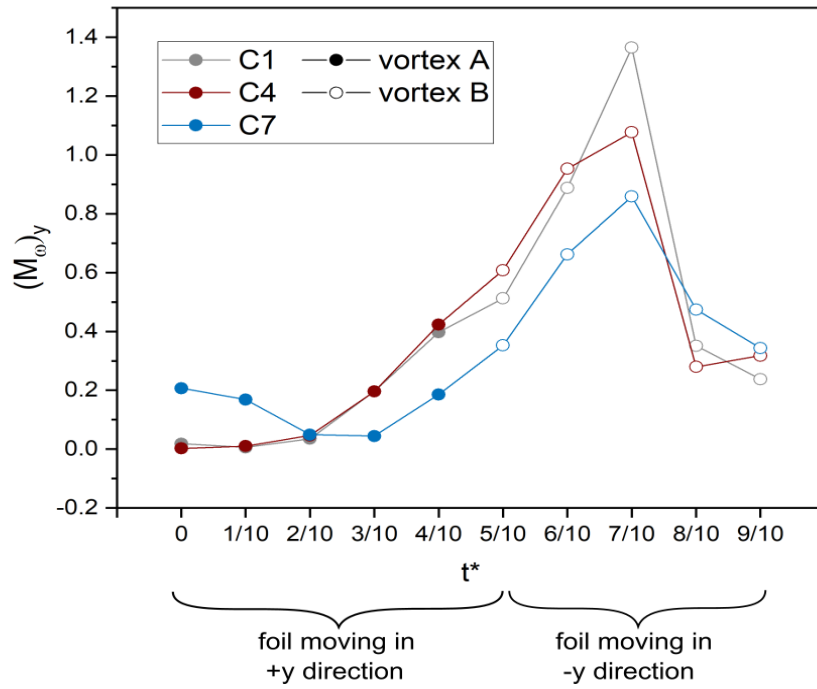
$$C_x = \frac{d(M_\omega)_x}{dt}, \quad (5.4)$$

$$C_y = \frac{d(M_\omega)_y}{dt}. \quad (5.5)$$

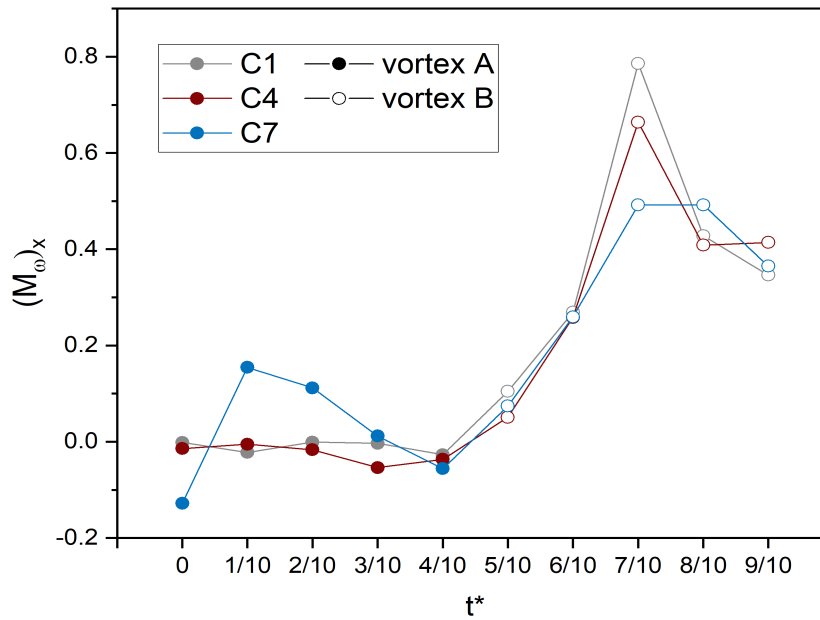
By plotting the moment of vorticity at each phase, the force coefficients can be determined from the slopes of the plots. This method has been successfully implemented in past studies on oscillating cylinders and foils by Oshkai and Rockwell [106], Siala and Liburdy [107], Iverson et al. [108], and most recently by Lee [100].

Plots of the moments of vorticity from the wake vorticity about the pitch axis of the foil are provided in Figs. 5.3 and 5.4 for the *K0* and *K056* configurations, respectively. In each figure, plot (a) shows the lateral moment of vorticity $(M_\omega)_y$ and plot (b) shows the streamwise moment of vorticity $(M_\omega)_x$. For the phases $t^* = 0/10$ to $t^*=4/10$, the moments of vorticity were plotted for the primary vortex *A*, indicated in the vorticity plots of Figs. 5.1 and 5.2, as the foil moved in the positive y-direction. In phases $t^* = 5/10$ to $t^*=9/10$, the heaving motion reversed as the foil moved in the negative y-direction, and the LEV was shed and convected downstream. This shed LEV had the equivalent circulation and position, with opposite sign, to vortex *B* showing in Figs. 5.1 and 5.2. The slope of the curves plotted in Figs. 5.3 and 5.4 are representative of the flow-induced forces, because the force coefficients are equal to the time derivatives of the moments of vorticity as shown in Eqs. 5.4 and 5.5.

The plot of $(M_\omega)_y$ is of primary relevance to the OFT performance, because it

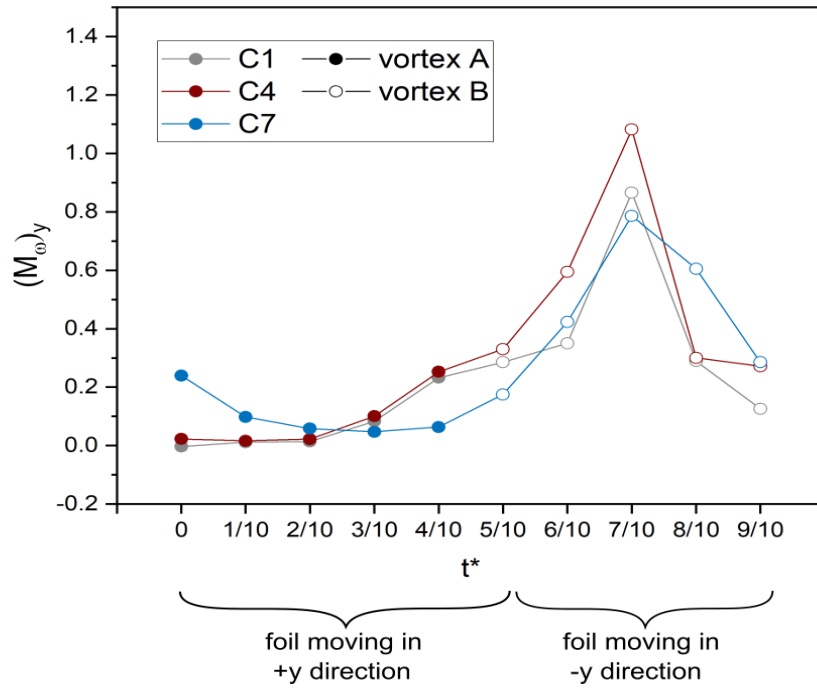


(a)

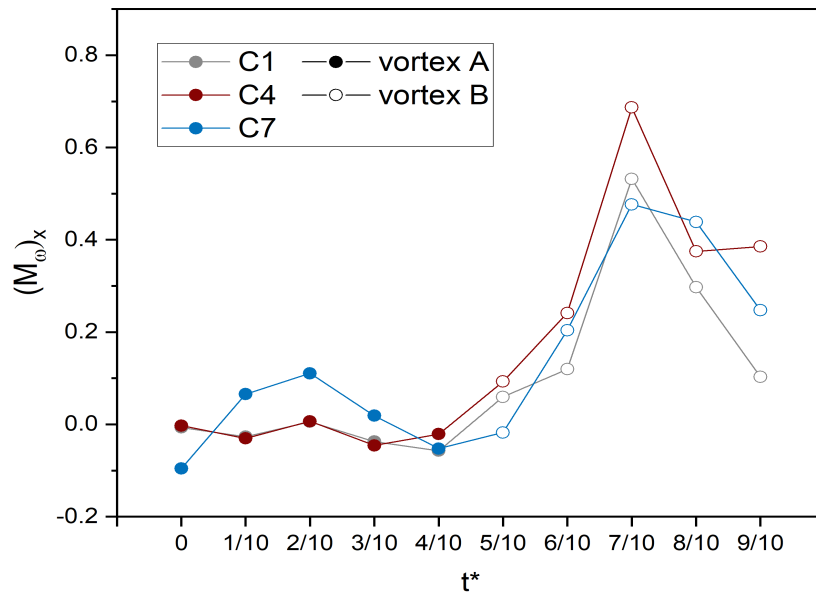


(b)

Figure 5.3: Moment of vorticity (M_ω) of the primary vortex A (\bullet) and the shed vortex B (\circ) for the $K0$ configuration. (a) Lateral moment $(M_\omega)_y$. (b) Streamwise moment $(M_\omega)_x$.



(a)



(b)

Figure 5.4: Moment of vorticity (M_ω) of the primary vortex A (\bullet) and the shed vortex B (\circ) for the *K056* configuration. (a) Lateral moment $(M_\omega)_y$. (b) Streamwise moment $(M_\omega)_x$.

corresponds to the generation of lift during the oscillation cycle. The lateral moments of vorticity are discussed first, beginning with the $K0$ configuration. From phases $t^*=0/10$ to $t^*=4/10$, the foil was moving in the positive y-direction, so a positive $(M_\omega)_y$ slope is required to supply a lift force to the foil. In the first half of the oscillation cycle, lateral moments were similar for the confinement levels $C1$ and $C4$. This aligns with what was observed in Fig. 5.1, which showed qualitatively similar flow patterns for the two cases. A slight distinction existed between phases $t^*=3/10$ and $t^*=4/10$, where the transverse moment $(M_\omega)_y$ increased slightly more rapidly for the $C4$ case than the $C1$ case. This indicated a larger lift force was generated by the LEV in the direction of travel, which acted to enhance performance. Meanwhile, the case of highest confinement $C7$ exhibited a slightly decreasing slope of $(M_\omega)_y$ in the phase range of $t^*=0/10$ to $t^*=2/10$, which corresponded to the generation of an opposing lift force for these phases. Between $t^*=2/10$ and $t^*=3/10$, the slope was nearly constant, indicating null force acting on the foil. In the remainder of the half-cycle, a positive lift force was generated for the confinement $C7$ case, indicated by an increasing slope, although the shallower slope of $(M_\omega)_y$ indicated a lower magnitude of generated lift force in the direction of travel, compared to the lower confinement levels. This result is consistent with the observations made in the previous sections on the poor synchronization between flow-induced forces and the motion of the foil.

From phases $t^*=5/10$ to $t^*=9/10$, the foil was moving in the negative y-direction, so a negative $(M_\omega)_y$ slope was required supply a lift force to the foil. In this portion of the oscillation cycle, a larger discrepancy between the $C1$ and $C4$ confinement cases was present. Between phases $t^*=5/10$ and $t^*=7/10$, the $C1$ case exhibited a steeper increase in the slope of $(M_\omega)_y$ than the $C4$, indicating a larger opposing force to the foil's travel direction. Between phases $t^*=7/10$ and $t^*=8/10$, a steep negative slope in $(M_\omega)_y$ was observed for both cases, indicating a lift force in the direction of travel. The $C1$ case demonstrated a slightly steeper decline, indicating a larger lift force than for the $C4$ case. From phases $t^*=8/10$ to $t^*=9/10$, there was a slight increase in $(M_\omega)_y$ slope for the $C4$ case, while the slope of the $C1$ curve continued to decline. This will act to change the timing of the foil motions, as the foil in the $C4$ case prepares for pitch reversal, demonstrating a more efficient transfer of energy between the two DOFs by an appropriate timing of the pitch reversal within the heave cycle. The overall increase in performance from case $C1$ to case $C4$ seemed to result from the increase in lift from the LEV in the first half-cycle, limited resisting force from the shed LEV in the second half-cycle, and more efficient transfer of energy

between the two DOFs. Unlike the first half-cycle for the *C7* case, the timing of the increasing and decreasing $(M_\omega)_y$ for the second half-cycle agreed with that observed for the lower confinement cases. The slope between $t^*=5/10$ and $t^*=7/10$ was similar to that of the *C4* case, indicating that similar impeding forces were observed. Note that this only accounts for the shed vorticity from the foil, and does not account for the effect of the vorticity generated at the confining walls that was observed in the previous section. Between phases $t^*=7/10$ and $t^*=8/10$, the negative rate of change of the moment of vorticity was much shallower than the other two confinement cases, indicating a smaller lift force acting on the foil in the direction of its travel. The poor timing of the forces from the LEV in the first half-cycle and the relatively low lift force provided from the shed vorticity in the second half-cycle accounted for the degraded performance observed at high confinement, consistent with observations from the previous section.

The trends of the lateral moment of vorticity $(M_\omega)_y$ for the *K056* configuration are now discussed and compared with those observed for the *K0* configuration. Once again, the $(M_\omega)_y$ trend for the *C1* and *C4* cases in the first half-cycle were very similar. Although the absolute value of the *C4* moments of vorticity were higher than those of the *C1* case at each phase between $t^*=0/10$ and $t^*=4/10$, the slopes appeared to be nearly identical, indicating that the LEV induced nearly the same lift on the foils at the low and medium confinement levels. However, the trend of $(M_\omega)_y$ in the first half-cycle for confinement *C7* was once again quite different from the other two confinement levels. A decreasing slope was observed from $t^*=0/10$ to $t^*=3/10$, meaning that an impeding force acted on the foil under *C7* confinement for a longer timeframe than it did for the *K0* configuration, where the decreasing slope existed until $t^*=2/10$. The slope only began to increase noticeably at the end of the stroke between $t^*=4/10$ and $t^*=5/10$. This is in agreement with the results from Section 4, which showed a more significant drop in performance for the *K056* configuration than for the *K0* configuration. This also supports that the timing between the flow-induced forces and the foil motion was not optimal, with lift forces only occurring at the very end of the stroke.

In the second half-cycle, from phases $t^*=5/10$ to $t^*=9/10$, the *K056* configuration results differed slightly from the observations from the *K0* configuration. Here, the *C4* confinement level demonstrated a larger positive rate of change of $(M_\omega)_y$ between $t^*=5/10$ and $t^*=6/10$ with respect to the *C1* case. This means that a larger opposing force existed on the foil during this range of travel. The slopes of $(M_\omega)_y$ were then

nearly identical between $t^*=6/10$ and $t^*=7/10$, indicating that the foils experienced the same opposing force at this phase. From $t^*=7/10$ to $t^*=8/10$, the decreasing slope of $(M_\omega)_y$ was much steeper for confinement level $C4$ than for confinement level $C1$. This indicated that the shed LEV induced a larger lift force on the foil under medium confinement than under low confinement, proving to be the main contributor of the enhanced performance observed in the $C4$ case. Once again, at the end of the stroke between $t^*=8/10$ and $9/10$, the foil in the $C4$ confinement had a more neutral slope compared to that of the foil in $C1$ confinement. This again demonstrated that the foil was preparing for pitch reversal, and exhibited an efficient energy transfer between the degrees of freedom. The $C7$ case demonstrated similar opposing forces to the $C4$ case between $t^*=5/10$ and $t^*=7/10$, from the similar $(M_\omega)_y$ slopes observed. However, consistent with the $K0$ configuration, the decreasing slope from $t^*=7/10$ to $t^*=9/10$ was relatively shallow, indicating a lower lift force acted on the foil. Contrary to that observed for the $K0$ configuration, the steeper portion of the curve occurred between $t^*=8/10$ and $t^*=9/10$ rather than $t^*=7/10$ and $t^*=8/10$. The higher lift force occurring later in the stroke, once again supports that the timing of the flow-induced forces and the foil oscillating played a significant role in the performance, and explains the more stark drop in performance for the $K056$ configuration than for the $K0$ configuration.

Since the streamwise moment of vorticity $(M_\omega)_x$ acted in the direction normal to the heaving motion of the foil, it is of less significance for the considered energy harvesting application. It is worth noticing, however, that for the first half of the oscillation period, the largest confinement level $C7$ resulted in a rapid change in $(M_\omega)_x$, while the streamwise moments in the cases of the low and medium confinement levels remained close to zero. Since the foil was restricted to lateral travel, the streamwise forces contributed only to changes in the pitch degree of freedom. These changes in pitch were not directly quantified in this study since the moment of vorticity was calculated with respect to the pitch axis. However, the previous results indicate that the streamwise forces were acting to decrease the pitch angle, contributing to inefficient timing between the development of the flow features and the motion of the foil at the highest confinement level.

Chapter 6

Conclusions

The effect of varying flow confinement on the fully-passive OFT was investigated experimentally and the performance of the turbine was related to the flow structures by analyzing the 2D LEV flow patterns. Two structural configurations, one with pitch stiffness $k_\theta^* = 0$ (*K0*) and one with pitch stiffness $k_\theta^* = 0.056$ (*K056*), were tested.

The kinematic and performance parameters for the *K0* and *K056* configurations were obtained at eight levels of confinement by changing the position of the lateral walls from $W/c = 9$ to $W/c = 4.25$. The blockage ratio ε exhibited a similar trend with confinement level W/c for both configurations, with the *K056* configuration reaching larger blockage ratios at each confinement point than the *K0* configuration. Based on the similar shape, the two curves were described using a single relation based on the confinement level and base level blockage ratio. Both configurations demonstrated a general increase in performance with confinement, as was expected based on previous works. The *K0* configuration had a base level performance of $\eta = 25.4\%$ and $C_p = 0.738$ at $\varepsilon = 0.215$, and reached a maximum of performance at the highest confinement level of $\eta = 32.3\%$ and $C_p = 0.963$ at $\varepsilon = 0.596$. The *K056* configuration had a base level performance of $\eta = 28.5\%$ and $C_p = 0.893$ at $\varepsilon = 0.245$, and reached a maximum of performance at the second highest confinement level of $\eta = 33.5\%$ and $C_p = 1.08$ at $\varepsilon = 0.464$.

Between the second-last and last confinement levels, the *K0* and *K056* configurations experienced a plateau and drop in performance, respectively. It was noteworthy, though, that the performance of the *K0* configuration did not drop off as it did for the *K056* configuration, because the *K0* configuration did not reach blockage ratio values as high as the *K056* configuration. It is concluded that a configuration with lower

pitch stiffness may operate within closer wall proximity before reaching degraded performance. This may be important if the turbine is to operate within an environment with pre-defined confinement level, or to know the upper level of confinement that can be imposed for performance enhancement.

The performance trends were related to the kinematics with the following general conclusions. First, the heave amplitude H_0^* increased with blockage ratio which meant the turbine had access to a greater region of flow energy, thus increasing the power coefficient C_p . The frequency of oscillation f^* remained relatively constant, indicating that the heave velocity must have also increased. Since the power is related to the square of heave velocity \dot{h}^2 , the power extraction increased with confinement. Between the second-last and last confinement levels of the *K056* configuration, the phase lag between degrees of freedom sharply increased, indicating that there was poor timing between the flow forces and foil motion.

This work presented polynomial fits within the experimental data range for a more precise fit, and linear fits to estimate the data at lower blockage ratios. These fits can be used to estimate the unconfined efficiency and power coefficient values. Further, the power coefficient data was adjusted using general turbine blockage corrections. Ultimately, these corrections were deemed inadequate for the fully-passive OFT due to the fact that the turbine kinematics change with changing confinement. This is further expanded on in Section 6.1.

Planar PIV was used for visualization of the wake structures in the first half of the oscillation cycle. Specifically, the phase-averaged out-of-plane vorticity fields showed the initial formation of the LEV and subsequent shedding into the wake for confinement levels *C1*, *C4* and *C7* for both configurations. Overall, vorticity fields for the *C1* and *C4* cases were very similar for both configurations, with the key difference being the pitch angle of the foil at a given phase of the heave cycle. Major discrepancies were observed in the flow fields of the *C7* cases compared to the lower confinement cases. This was expected since the performance results indicated a drop in power extraction at high confinement. The pitch angle was much lower than the other cases, meaning that the effective angle of attack was low, leading to poor development of the LEV. Without a strong LEV, the foil experienced much lower lift forces and therefore lower performance as was observed through the performance measurements. The LEV did not achieve substantial strength until the end of its stroke, confirming that the flow forces were not well timed with the foil motion. The other key observation was the formation of a counter-rotating vortex at the wall for

the $C7$ cases. This vortex interacted with the wake vorticity shed from the foil, and likely negatively affected the turbine's performance.

The vorticity fields obtained from the PIV measurements were correlated to the induced forces experience by the foil by calculating the moment of vorticity of the LEV as it developed and shed downstream. Forces acting on the foil were based on the rate of change of the moment of vorticity. The results further reinforced that the timing between the flow forces and foil motion are key to enhancing performance, and that poor timing results in a lower performing turbine. While the $C1$ and $C4$ cases generally followed similar trends with slightly increased forces experienced by the $C4$ foil, the $C7$ case showed much different trends, where opposing forces were present for the first part of the stroke, and positive lift forces did not occur until the very end of the stroke.

The main conclusion from the present work is that operating the turbine within close wall proximity largely impacts the kinematics, performance and wake characteristics. The results showed that the wall proximity promotes the formation of a stronger LEV leading to a stronger lift force acting on the foil during the oscillation cycle. This is important for two key reasons: (1) designing for a turbine to operate within a confined environment is desirable due to the enhanced energy extraction potential with the same turbine size, and (2) it is important to acknowledge that confining walls present in an experimental study will modify the performance that can be expected at a natural site. For the first point, an important takeaway from the study was the upper limit to the increase of energy extraction, after which a drop in performance was observed. This study showed that the two configurations experienced different blockage ratios for the same walls spacing, although the critical blockage ratio was close to $\varepsilon \approx 0.5$ for both configurations. It is therefore important to deploy the turbine in an environment where the blockage ratio does not exceed this critical parameter. For the second point, it is important to adjust reported values according to the level of blockage present. Overall, the blockage proved to be an important value to better understand the achievable performance and to help inform suitable locations for turbine deployment.

6.1 Future Work

The present work investigated the general effects of blockage on the fully-passive OFT by varying the flow confinement for two different structural configurations of

the turbine. This provided an understanding of the general trends in kinematics and performance metrics as confinement increased - specifically the regions of increasing and decreasing performance. This study also provided physical insight into why these trends occurred, based on the flow structures around the turbine. However, the experiments exhibited limitations due to the physical flow facility as well as the time needed to set up experiments. There are areas of this research that can be expanded upon in future experimental and computational works. The following are the recommended directions of research related to the present work.

The major limitation of this confinement study was brought upon by the size of the testing facility, which imposed a large baseline confinement on the turbine. This meant that the unconfined versus confined configurations could not truly be compared, but rather the trends of increasing confinement from the base level confinement of the flow channel at approximately $\varepsilon=20\%$. Without the operating data at $\varepsilon=0\%$, a correction for blockage cannot be accurately made. This provides a path for further work to test in an unconfined environment to get the baseline operating data including performance and kinematic metrics. With this baseline data, extensions of existing blockage corrections for other types of turbines and immersed bodies (e.g. [6, 82, 89]) can be attempted for the fully-passive OFT. Provided the opportunity to test the prototype in a larger flow facility, the base level performance could be obtained. This work also provides data which can be used to validate computational works. This would also be a good route for pursuing blockage corrections, since it is easier to change the flow environment while controlling all other variables.

In this study, two different structural configurations of the turbine that employed different amounts of pitch stiffness were investigated. A general trend of increasing performance was observed for both configurations, up to a critical point where performance dropped. There were, however, differences in the trendlines for performance and kinematic parameters with a key difference being the larger heave amplitude of the *K056* configuration leading to a larger blockage ratio for the same wall spacing. An extension to this work could include investigating different structural configurations by varying the heave damping and stiffness as well as the pitch stiffness. This study could further verify whether the general trends are observed, and provide a better idea of what a given structural configuration of the turbine would generate a given blockage ratio. This is important to know, since the blockage ratio is not known prior to experiments due to the passive nature of the turbine. The trends of the blockage ratio ε with confinement level W/c were similar and able to be described

using a single equation in Eq. 4.1. Looking at other structural configurations would validate whether this trend is consistent.

In extension, a parametric study at different confinement levels could be conducted to determine how the optimal operating parameters shift with confinement. The optimal parameters have been shown to shift with confinement level for the active OFT [91], so it is expected that they will shift for the fully-passive OFT as well. This is an important area to explore to understand what structural parameters to employ in a given operating site, to optimize the turbine performance. A parametric study has been conducted on the turbine prototype used in this work by Boudreau et al. [5,43], although the optimal parameters in the relatively high confinement test section are likely different than those in an unconfined environment. Further, the effect of varying freestream velocity on the turbine's confinement level should be explored. It is expected that the higher inflow would affect the flow forces on the turbine, thus changing the heave amplitude and blockage ratio experienced by the turbine.

In this study, confinement was imposed on the turbine through the use of equidistance walls, and the confinement level was varied in the lateral direction only. Further studies may investigate different configurations which simulate other scenarios encountered at a deployment site. First, lateral versus spanwise confinement may be investigated to determine if different effects are observed, or if overall blockage ratio takes president. Second, the effects of one-wall versus two-wall confinement may be explored, since it is possible that this configuration comes up at a deployment site. Third, unsymmetrical wall placement should be investigated to determine how the effects on the turbine performance and flow dynamics change.

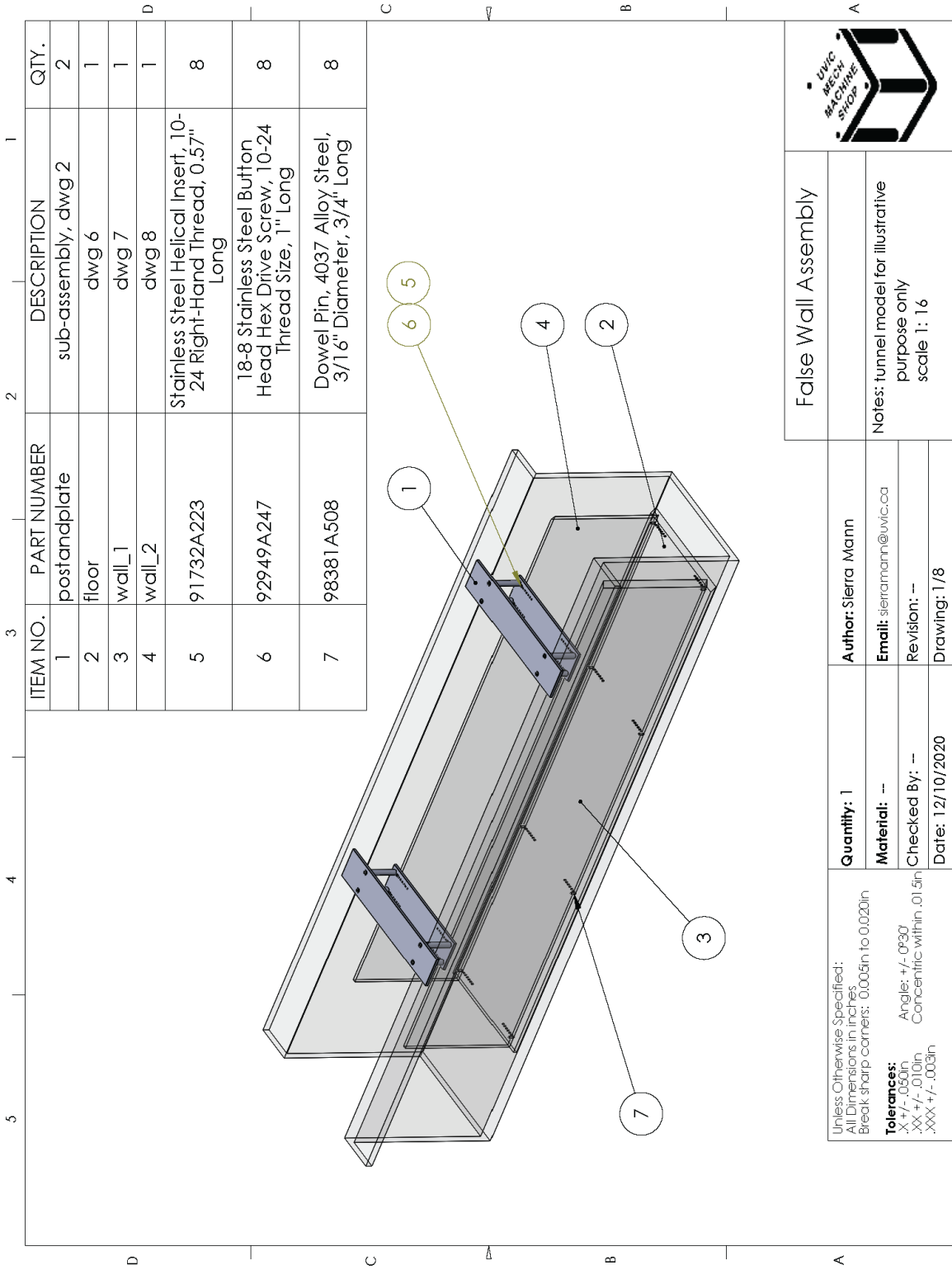
Lastly, the interaction between the foil wake vorticity and the vorticity generation on the confining walls were observed at the highest level of confinement. These PIV studies were meant to capture the wake dynamics, so the DAP was positioned downstream of the foil only, and did not cover the actual confining walls for cases outside the $C7$ confinement level. It would be interesting further investigate the vorticity generation at the wall, the level of confinement for which the wall vortex is formed and shed, and the level of confinement for which the wall vorticity and foil wake vorticity begin to interact. This would provide further insight into the physical mechanisms acting to degrade the performance at high levels of confinement.

Appendix A

False Wall Apparatus

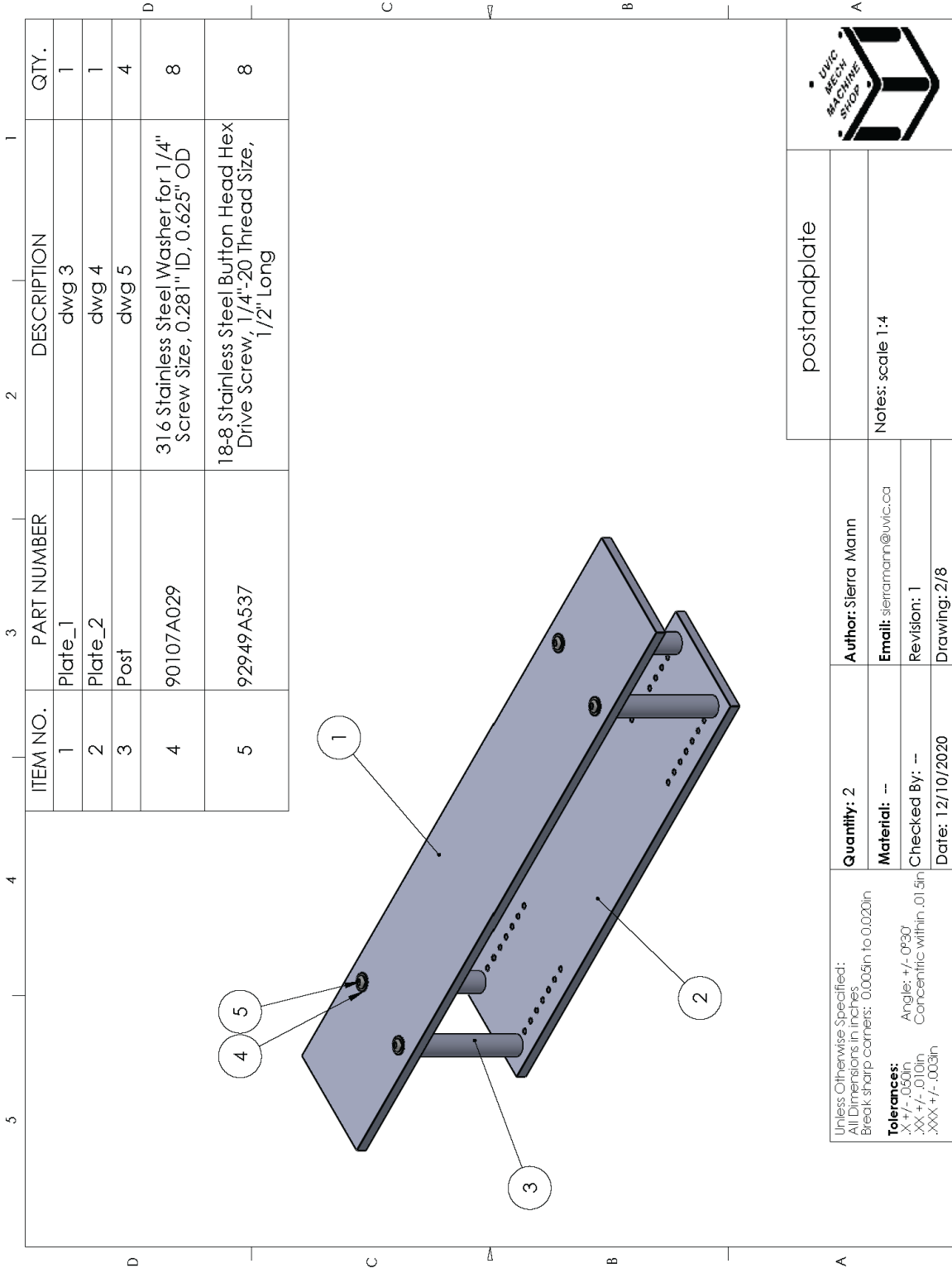
This appendix includes the drawing package for the false wall assembly. It is intended to give the reader an idea of the scale of the apparatus and an understanding of how to assemble the apparatus within the test section of the water channel.

Fig. A.1 shows the full assembly of the false wall apparatus and how it fits into the water channel. The false walls, shown in Figs. A.7 and A.8, include threaded holes at the tops and pins at the bottoms for securing at both the top and bottom. This ensures that the walls remain perfectly vertical in the channel and do not move in the flow. The false floor, in Fig. A.6 sits on the actual test section floor and includes holes at 4 different lengthwise locations, where the false wall pins insert into. Seven hole locations exist in the transverse direction, allowing for different wall placements. The walls are held at the top by a drop down plate which uses a post and plate design, shown in Figs. A.2 to A.5. The height of the post-and-plate assembly ensures that the walls will not collide with the turbine carriage, but remain above the water level used in the experiments. The bottom plate includes holes at different spacings which correspond to the holes in the false floor, so the walls are held at the same location from the top and bottom. Screws are then used to fasten the walls to the plate. Rubber shims were placed between the water channel and the bottom plate of the post-and-plate assembly, to ensure that the walls could not move side to side.



SOLIDWORKS Educational Product. For Instructional Use Only.

Figure A.1: False wall assembly drawing.



SOLIDWORKS Educational Product. For Instructional Use Only.

Figure A.2: Post and plate assembly drawing.

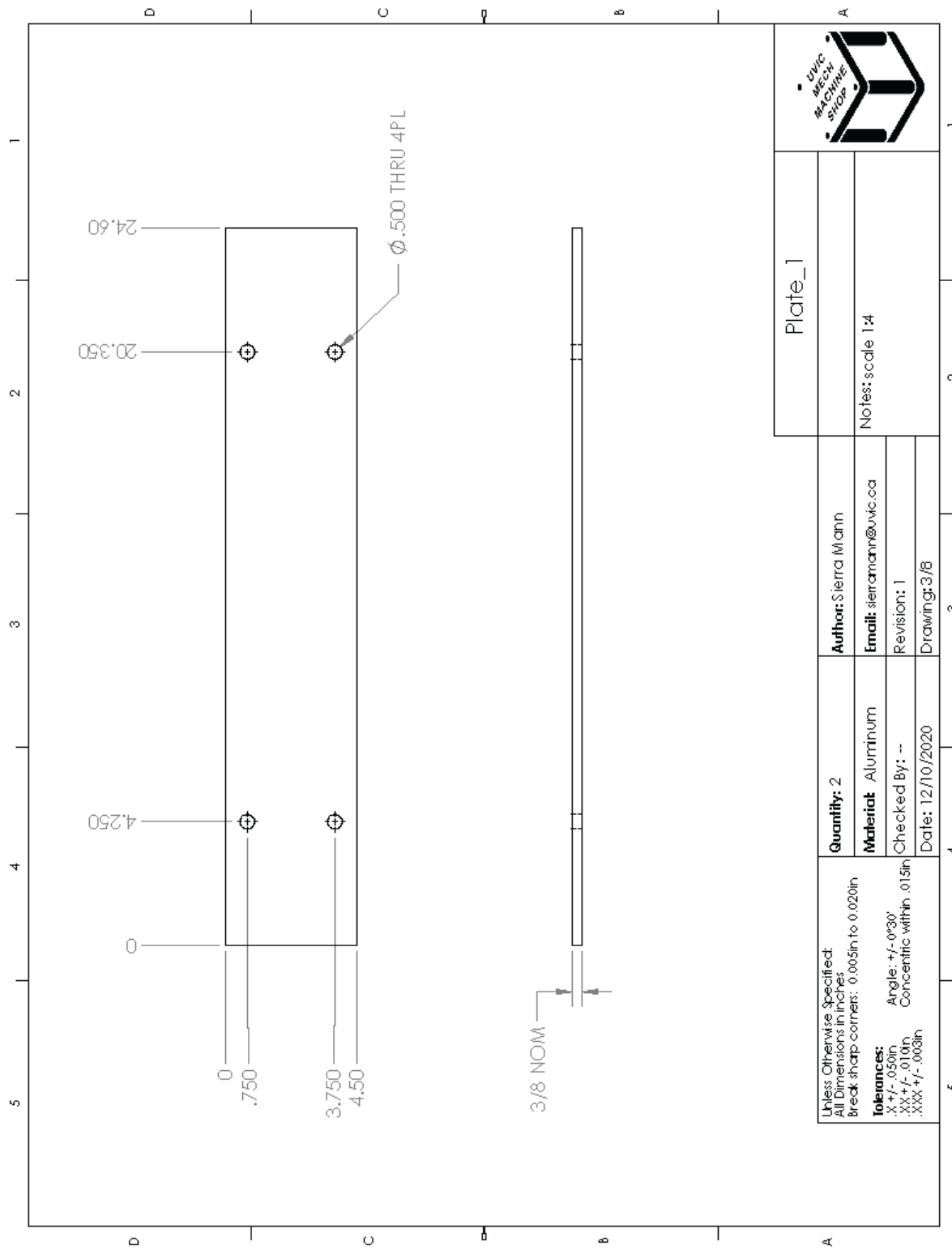


Figure A.3: Top plate of post and plate assembly drawing.

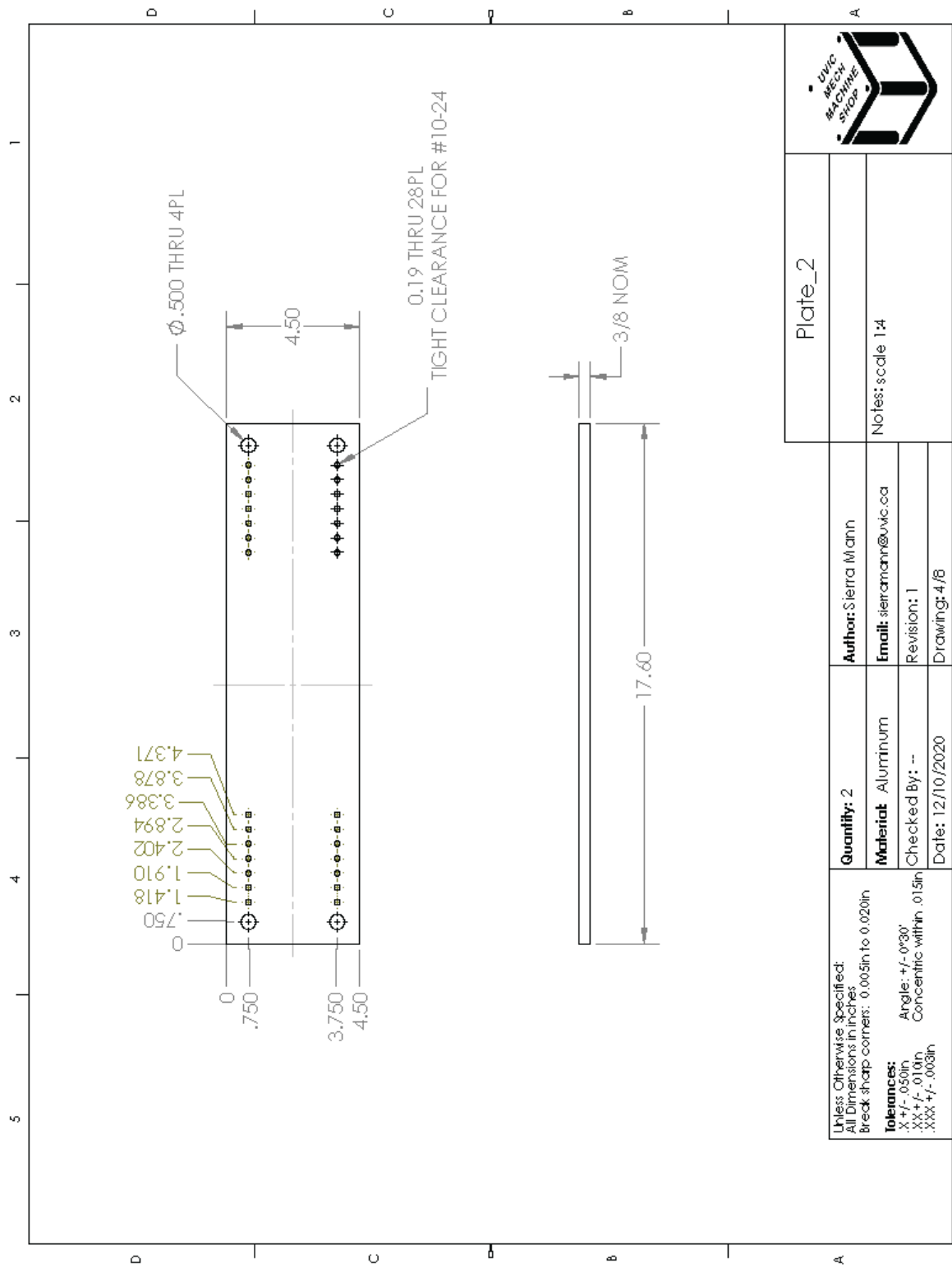


Figure A.4: Bottom plate of post and plate assembly drawing.

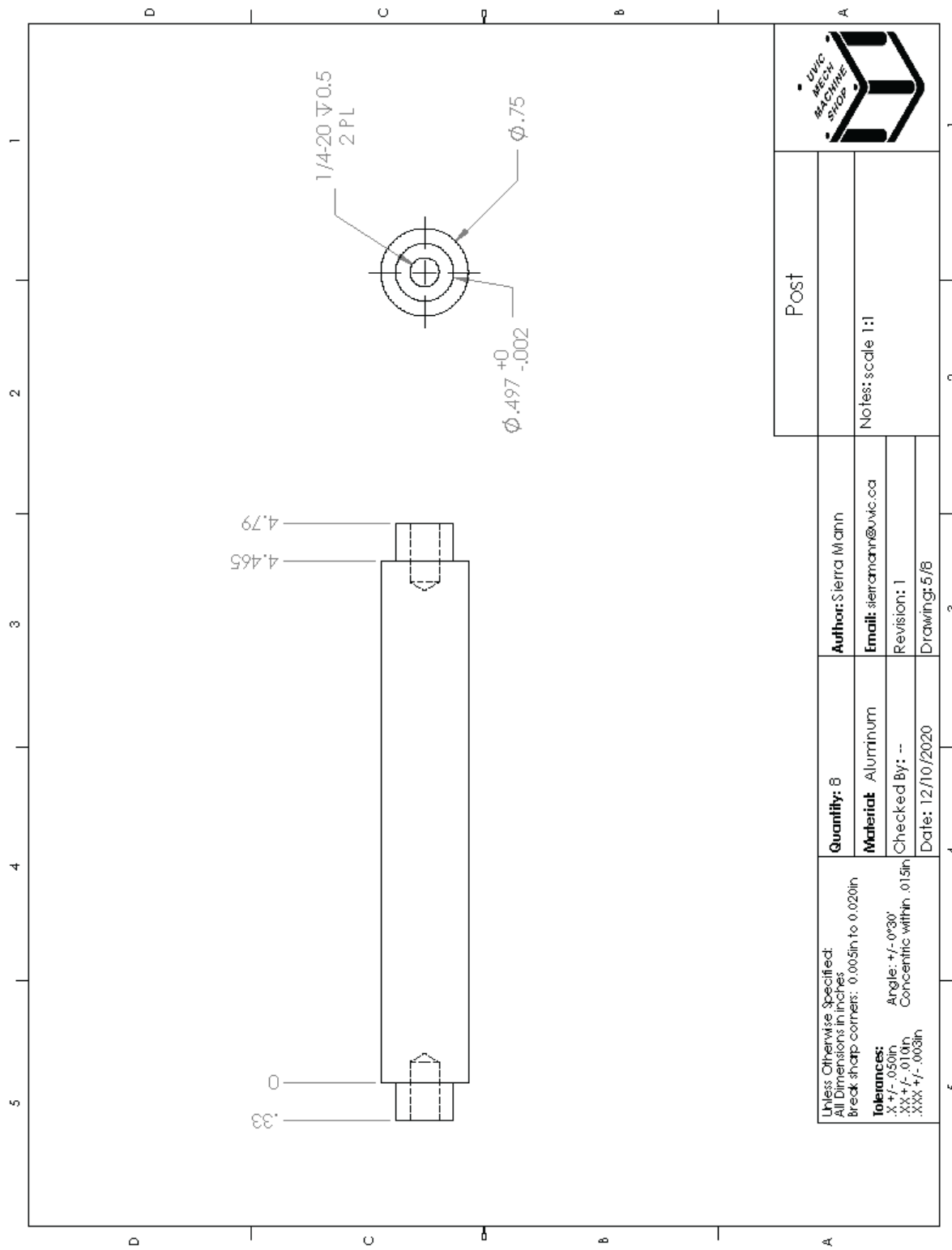


Figure A.5: Post in the post and plate assembly drawing.

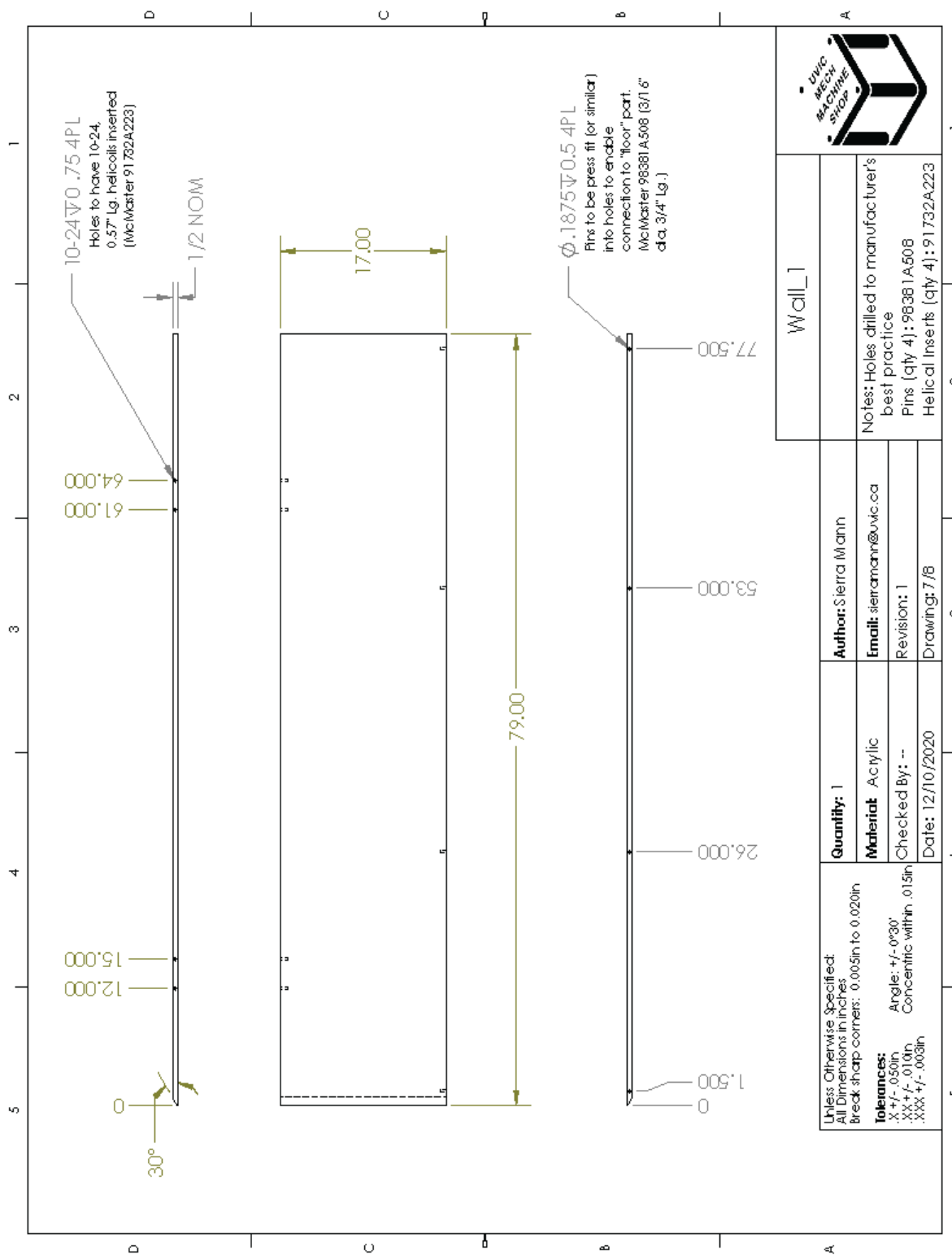


Figure A.7: False wall 1 drawing.

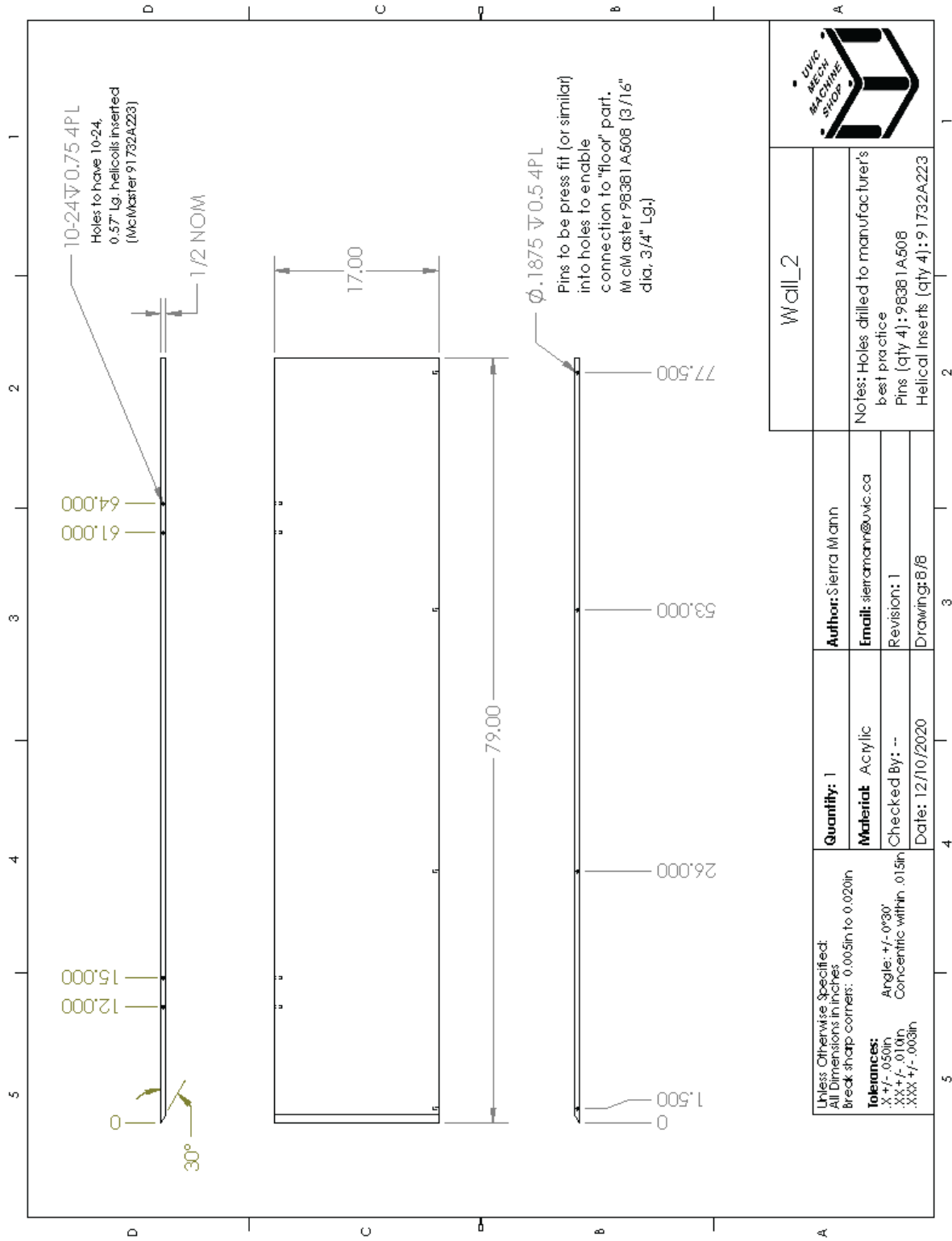


Figure A.8: False wall 2 drawing.

Appendix B

Standard deviations of the kinematic and performance parameters

This appendix provides the standard deviations in the performance and kinematic indicators for the data sets. The time evolution of the normalized heave and pitch positions are provided in Figs. B.1 and B.2 over 10 cycles for the *K0* and *K056* configurations, respectively. This is intended to provide a sense of the DOF motions relative to one another, and the change in cyclic variation between low and high confinement levels.

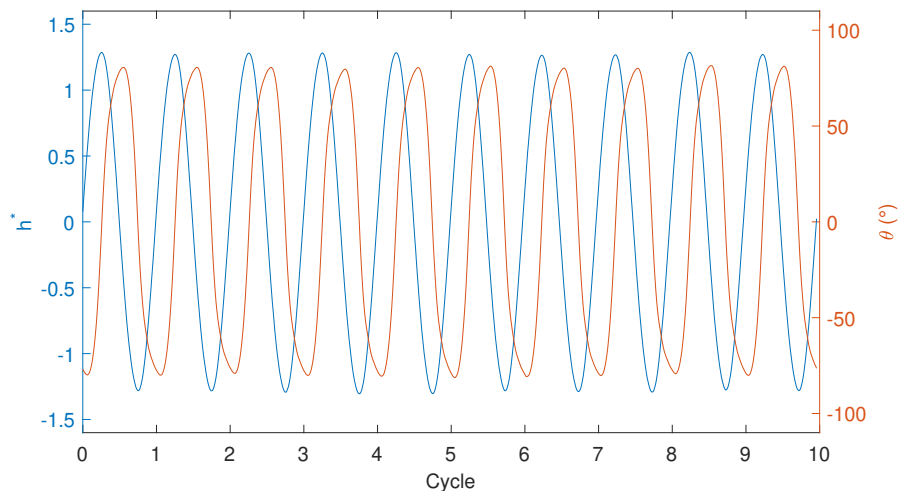


Figure B.1: Time evolution of the normalized heave and pitch positions of the foil over 10 cycles for the *K0* configuration at confinement level *C0*.

Appendix C

Uncertainty in the kinematic and performance parameters

This appendix provides the percentage uncertainties in the performance and kinematic indicators for the data sets. Uncertainty for the $K0$ data set is provided in Tbl. C.1 and uncertainty for the $K056$ data set is provided in Tbl. C.2. Sources of uncertainty are discussed in the main thesis body.

Table C.1: Uncertainties (%) in kinematic and performance parameters for the $K0$ configuration

Parameter	C0	C1	C2	C3	C4	C5	C6	C7
U_{C_p}	2.679	2.684	2.674	2.719	2.718	2.727	2.666	2.745
U_η	2.703	2.707	2.696	2.742	2.740	2.749	2.686	2.768
$U_{H_0^*}$	0.177	0.174	0.172	0.172	0.171	0.169	0.163	0.162
U_{θ_0}	1.059	1.059	1.059	1.059	1.059	1.059	1.059	1.059
U_ϕ	3.365	3.295	3.320	3.276	3.276	3.211	3.129	3.029
U_{f^*}	1.000	0.993	1.002	0.997	1.001	0.998	1.002	0.994

Table C.2: Uncertainties (%) in kinematic and performance parameters for the *K056* configuration

Parameter	C0	C1	C2	C3	C4	C5	C6	C7
U_{C_p}	2.640	2.647	2.668	2.603	2.678	2.668	2.6599	2.681
U_η	2.658	2.666	2.685	2.620	2.696	2.685	2.616	2.698
$U_{H_0^*}$	0.163	0.161	0.158	0.156	0.156	0.154	0.151	0.150
U_{θ_0}	1.060	1.060	1.060	1.060	1.060	1.060	1.060	1.062
U_ϕ	3.172	3.019	3.034	2.990	3.025	2.873	2.734	2.245
U_{f^*}	0.977	0.971	0.977	0.972	0.976	0.967	0.952	0.894

Appendix D

Curve Fitting

The MatLab Curve Fitting toolbox was used to test different curve fits on the data to provide curve equations for the ε vs. W/c , C_p vs. ε , and η vs. ε trends. The MatLab package applies the least squares method to determine the coefficient values in a given equation. The fits were evaluated based on the R^2 value as well as physical fit judged from plotting the trends to compare to the actual data. This appendix provides the MatLab outputs for different curve fits including the coefficients, confidence bounds, and R^2 value of the fit, as well as plots summarizing the different fits.

D.1 ε vs. W/c curve fits

Since the ε vs. W/c trends for both the *K0* and *K056* configurations were visually similar but shifted about the y -axis, the curves were fit using a single trendline as a function of the confinement level W/c , and the base level blockage ratio $\varepsilon_0 = \varepsilon(W/c = 9)$. The polynomial function of two variables is called in MatLab using `polyxy`, where x is the degree of the first independent variable (in this case, W/c), and y is the second independent variable (in this case, ε_0). Three different fits are provided here: Poly21, second degree in x and first degree in y ; Poly31, third degree in x and first degree in y , and Poly21+power, a user input model which followed the Poly21 model with an added power term. Note that the last fit required nonlinear regression due to the nonlinear power term. The following are the outputs from Matlab which provide the form of the equation, the calculated coefficients with confidence bounds, and the R^2 value:

Poly21

Linear model Poly21:

$$\text{val}(x,y) = p00 + p10*x + p01*y + p20*x^2 + p11*x*y$$

Coefficients (with 95% confidence bounds):

p00 =	0.4993	(0.2119, 0.7867)
p10 =	-0.1632	(-0.2134, -0.113)
p01 =	3.55	(2.348, 4.752)
p20 =	0.01242	(0.01057, 0.01428)
p11 =	-0.2996	(-0.4899, -0.1094)

$$R^2 = 0.9965$$

Poly31

Linear model Poly31:

$$\text{val}(x,y) = p00 + p10*x + p01*y + p20*x^2 + p11*x*y + p30*x^3 + p21*x^2*y$$

Coefficients (with 95% confidence bounds):

p00 =	0.8296	(0.188, 1.471)
p10 =	-0.3705	(-0.5891, -0.1518)
p01 =	4.749	(2.151, 7.347)
p20 =	0.05203	(0.02947, 0.0746)
p11 =	-0.6832	(-1.497, 0.1308)
p30 =	-0.002333	(-0.003218, -0.001447)
p21 =	0.02912	(-0.03224, 0.09047)

$$R^2=0.9993$$

Poly21+power

General model -> poly21+power:

$$\text{gen} = a*y + c*(x)^b + d*x + e*x*y + f + g*x^2$$

Coefficients (with 95% confidence bounds):

a =	3.55	(2.898, 4.202)
b =	0.3056	(-10.7, 11.31)
c =	-5.405	(-186.9, 176)
d =	0.6168	(-11.95, 13.19)

$$\begin{aligned}
 e &= -0.2997 & (-0.4029, -0.1965) \\
 f &= 6.048 & (-192.7, 204.8) \\
 g &= -0.01217 & (-0.1805, 0.1561)
 \end{aligned}$$

$$R^2=0.9992$$

Plots comparing the different curve fits against the experimental data are provided in Figs. D.1 and D.2 for the $K0$ and $K056$ configurations.

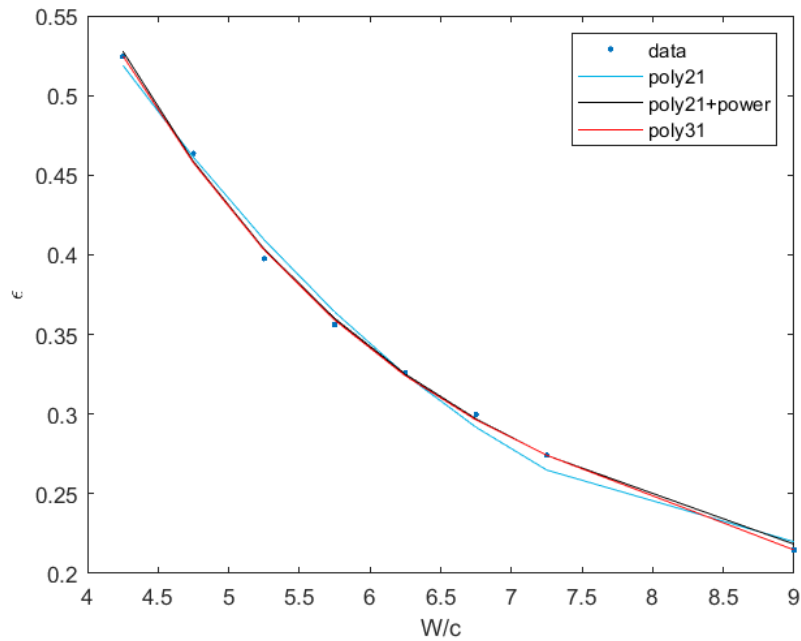


Figure D.1: Comparison of curve trends of ε vs. W/c for the $K0$ configuration.

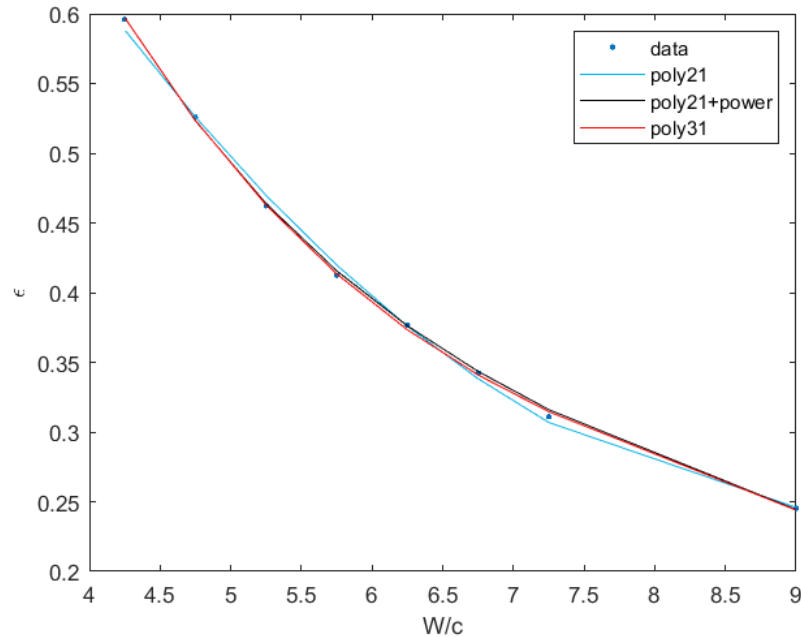


Figure D.2: Comparison of curve trends of ε vs. W/c for the *K056* configuration.

D.2 C_p vs. ε curve fits

The C_p vs. ε data was fit separately for the two configurations, since the trends were less similar than they were for the previous case. Different degrees of polynomial fits were used for each configuration, where Poly x denotes x degree of the polynomial. Since eight data points were collected for each configuration, polynomials up to the seventh degree can be fit. However, the higher the degree means a higher degree of oscillation in the trend, making the fits less physical. Here, the different curve fit outputs and plots of the curvefits are provided for C_p vs. ε for each configuration. For the poly1 (linear) fits, only the first seven points are used, since the performance drops off after that point and does not continue the trend. The following are the Matlab outputs for the different curve fits for the K0 and configurations:

Configuration *K0*:

Poly1

```
Linear model Poly1:
val(x) = p1*x + p2
```

Coefficients (with 95% confidence bounds):

p1 = 0.8104 (0.5981, 1.023)
 p2 = 0.559 (0.4865, 0.6316)

$$R^2 = 0.9506$$

Poly4

Linear model Poly4:

$$\text{val}(x) = p1*x^4 + p2*x^3 + p3*x^2 + p4*x + p5$$

Coefficients (with 95% confidence bounds):

p1 = -227 (-445.1, -8.904)
 p2 = 329.8 (8.233, 651.5)
 p3 = -173.8 (-346.6, -1.086)
 p4 = 40.04 (0.08873, 79.99)
 p5 = -2.63 (-5.978, 0.7187)

$$R^2 = 0.9927$$

Poly5

Linear model Poly5:

$$\text{val}(x) = p1*x^5 + p2*x^4 + p3*x^3 + p4*x^2 + p5*x + p6$$

Coefficients (with 95% confidence bounds):

p1 = -2110 (-4662, 442.8)
 p2 = 3671 (-1047, 8390)
 p3 = -2488 (-5902, 926.9)
 p4 = 820.1 (-387.1, 2027)
 p5 = -130.9 (-339.1, 77.35)
 p6 = 8.812 (-5.182, 22.81)

$$R^2 = 0.9990$$

Poly6

Linear model Poly6:

$$\text{val}(x) = p1*x^6 + p2*x^5 + p3*x^4 + p4*x^3 + p5*x^2 + p6*x + p7$$

Coefficients (with 95% confidence bounds):

p1 = 1.472e+04 (-2.202e+05, 2.496e+05)
 p2 = -3.449e+04 (-5.512e+05, 4.822e+05)
 p3 = 3.286e+04 (-4.331e+05, 4.988e+05)
 p4 = -1.628e+04 (-2.366e+05, 2.041e+05)
 p5 = 4421 (-5.316e+04, 6.201e+04)
 p6 = -623 (-8504, 7258)
 p7 = 36.3 (-404.6, 477.1)

$$R^2 = 0.9994$$

A plot comparing the above curve fits of C_p vs. ε for the $K0$ configuration are provided in Fig. D.3.

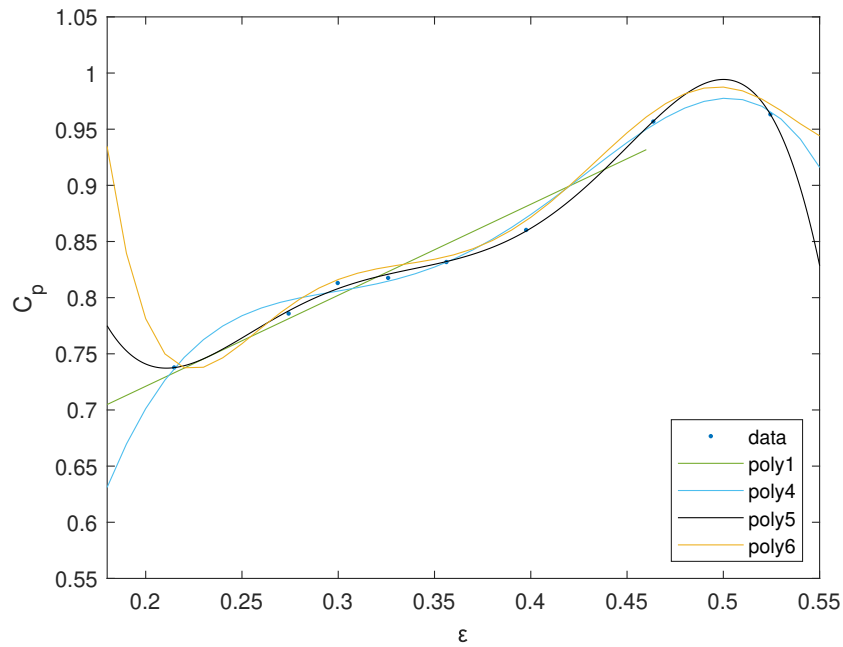


Figure D.3: Comparison of curve trends of C_p vs. ε for the $K0$ configuration.

Configuration K056:**Poly1**

Linear model Poly1:

$$\text{val}(x) = p1*x + p2$$

Coefficients (with 95% confidence bounds):

$$p1 = 0.6987 \quad (0.5381, 0.8593)$$

$$p2 = 0.7323 \quad (0.6693, 0.7953)$$

$$R^2 = 0.9616$$

Poly3

Linear model Poly3:

$$\text{val}(x) = p1*x^3 + p2*x^2 + p3*x + p4$$

Coefficients (with 95% confidence bounds):

$$p1 = -7.194 \quad (-24.17, 9.781)$$

$$p2 = 6.993 \quad (-12.6, 26.59)$$

$$p3 = -1.368 \quad (-8.672, 5.936)$$

$$p4 = 0.9124 \quad (0.03473, 1.79)$$

$$R^2 = 0.9742$$

Poly4

Linear model Poly4:

$$\text{val}(x) = p1*x^4 + p2*x^3 + p3*x^2 + p4*x + p5$$

Coefficients (with 95% confidence bounds):

$$p1 = -77.8 \quad (-226, 70.37)$$

$$p2 = 109.4 \quad (-139.3, 358.1)$$

$$p3 = -56.99 \quad (-209, 95.07)$$

$$p4 = 13.84 \quad (-26.2, 53.89)$$

$$p5 = -0.4088 \quad (-4.232, 3.415)$$

$$R^2 = 0.9866$$

Poly5

Linear model Poly5:

$$\text{val}(x) = p1*x^5 + p2*x^4 + p3*x^3 + p4*x^2 + p5*x + p6$$

Coefficients (with 95% confidence bounds):

p1 =	-1236	(-2507, 35.57)
p2 =	2516	(-153.6, 5185)
p3 =	-2020	(-4214, 174.7)
p4 =	796.7	(-85.26, 1679)
p5 =	-153	(-326, 19.96)
p6 =	12.3	(-0.931, 25.53)

$$R^2 = 0.9986$$

A plot comparing the above curve fits of C_p vs. ε for the *K056* configuration are provided in Fig. D.4.

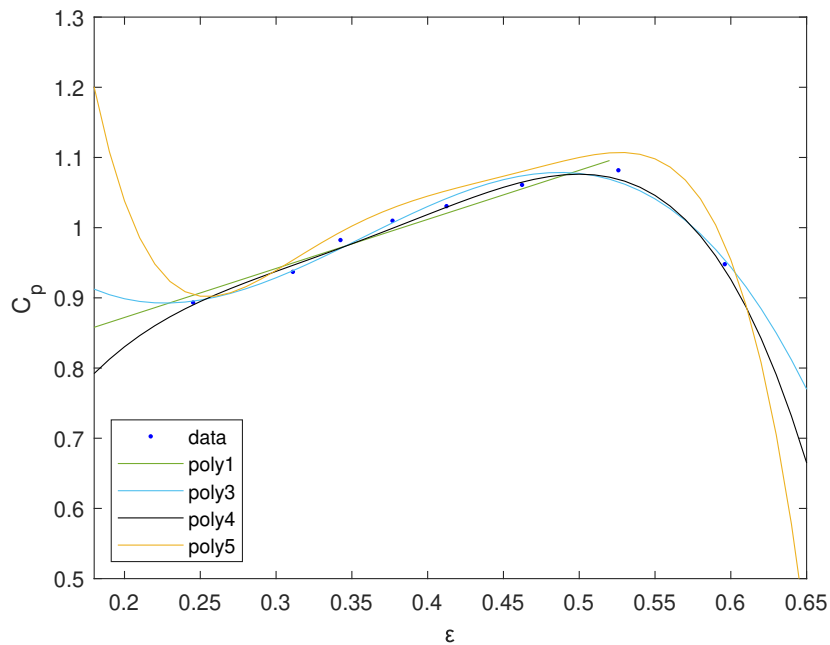


Figure D.4: Comparison of curve trends of C_p vs. ε for the *K056* configuration.

D.3 η vs. ε curve fits

The η vs. ε data was again fit into separate curves for the two different configurations. This section once again lists the different polynomial fits applied to the data sets and their respective confidence bounds and R^2 values, plus plots used to summarize the different curve fits. The poly1 (linear) curve fit used only the first seven data points, before the trend changed as the performance declined. The following are the Matlab outputs for the K0 and K056 configurations:

Configuration *K0*:

Poly1

Linear model Poly1:

$$\text{val}(x) = p1*x + p2$$

Coefficients (with 95% confidence bounds):

$$p1 = \quad 21.62 \quad (16.23, 27.01)$$

$$p2 = \quad 20.65 \quad (18.81, 22.5)$$

$$R^2=0.9551$$

Poly3

Linear model Poly3:

$$\text{val}(x) = p1*x^3 + p2*x^2 + p3*x + p4$$

Coefficients (with 95% confidence bounds):

$$p1 = \quad 27.49 \quad (-516.5, 571.5)$$

$$p2 = \quad -12.15 \quad (-611.1, 586.8)$$

$$p3 = \quad 19.14 \quad (-192.1, 230.4)$$

$$p4 = \quad 21.7 \quad (-2.17, 45.57)$$

$$R^2 = 0.9810$$

Poly4

Linear model Poly4:

$$\text{val}(x) = p1*x^4 + p2*x^3 + p3*x^2 + p4*x + p5$$

Coefficients (with 95% confidence bounds):

p1 = -5372 (-7624, -3119)
 p2 = 7939 (4618, 1.126e+04)
 p3 = -4246 (-6030, -2462)
 p4 = 991.8 (579.2, 1404)
 p5 = -59.05 (-93.63, -24.47)

$$R^2 = 0.9991$$

Poly5

Linear model Poly5:

$$\text{val}(x) = p1*x^5 + p2*x^4 + p3*x^3 + p4*x^2 + p5*x + p6$$

Coefficients (with 95% confidence bounds):

p1 = -1.78e+04 (-6.423e+04, 2.863e+04)
 p2 = 2.752e+04 (-5.832e+04, 1.134e+05)
 p3 = -1.583e+04 (-7.795e+04, 4.629e+04)
 p4 = 4140 (-1.782e+04, 2.61e+04)
 p5 = -450.1 (-4238, 3338)
 p6 = 37.49 (-217.1, 292.1)

$$R^2 = 0.9996$$

Poly6

Linear model Poly6:

$$\text{val}(x) = p1*x^6 + p2*x^5 + p3*x^4 + p4*x^3 + p5*x^2 + p6*x + p7$$

Coefficients (with 95% confidence bounds):

p1 = 3.935e+05 (-1.806e+06, 2.593e+06)
 p2 = -8.834e+05 (-5.723e+06, 3.956e+06)
 p3 = 8.078e+05 (-3.556e+06, 5.172e+06)
 p4 = -3.845e+05 (-2.448e+06, 1.679e+06)
 p5 = 1.004e+05 (-4.389e+05, 6.397e+05)
 p6 = -1.36e+04 (-8.741e+04, 6.02e+04)
 p7 = 772.1 (-3356, 4901)

$$R^2 = 0.9999$$

A plot comparing the above curve fits of η vs. ε for the $K0$ configuration are provided in Fig. D.5.

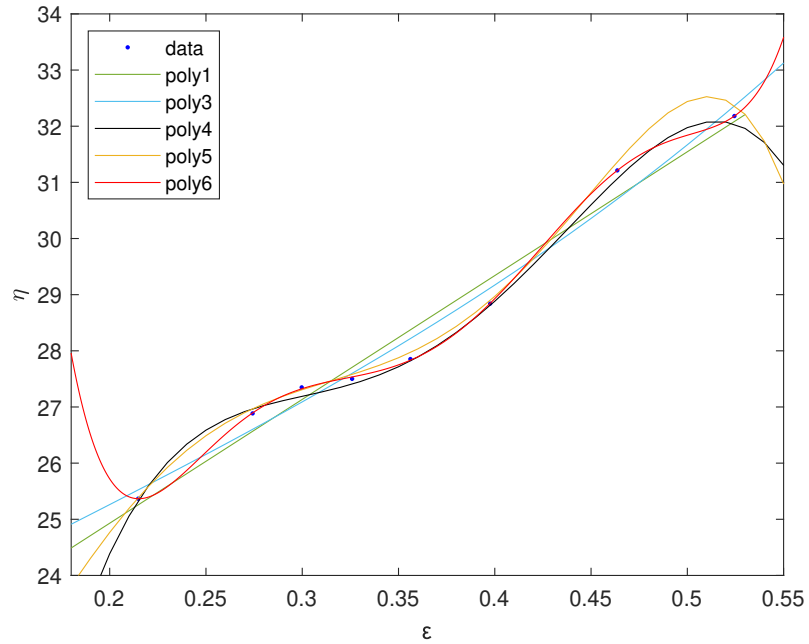


Figure D.5: Comparison of curve trends of η vs. ε for the $K0$ configuration.

Configuration ***K056***:

Poly1

Linear model Poly1:

$$\text{val}(x) = p1*x + p2$$

Coefficients (with 95% confidence bounds):

$$p1 = \quad 17.96 \quad (16.53, 19.38)$$

$$p2 = \quad 24.19 \quad (23.63, 24.75)$$

$$R^2 = 0.9953$$

Poly3

Linear model Poly3:

$$\text{val}(x) = p1*x^3 + p2*x^2 + p3*x + p4$$

Coefficients (with 95% confidence bounds):

p1 =	-686.1	(-1202, -170.1)
p2 =	758	(109.3, 1407)
p3 =	-250.6	(-512.1, 10.88)
p4 =	54.65	(20.89, 88.42)

$$R^2 = 0.9354$$

Poly4

Linear model Poly4:

$$\text{val}(x) = p1*x^4 + p2*x^3 + p3*x^2 + p4*x + p5$$

Coefficients (with 95% confidence bounds):

p1 =	-4475	(-7252, -1698)
p2 =	6816	(2156, 1.148e+04)
p3 =	-3813	(-6663, -963.2)
p4 =	945.6	(195.1, 1696)
p5 =	-58.5	(-130.2, 13.16)

$$R^2 = 0.9934$$

Poly5

Linear model Poly5:

$$\text{val}(x) = p1*x^5 + p2*x^4 + p3*x^3 + p4*x^2 + p5*x + p6$$

Coefficients (with 95% confidence bounds):

p1 =	-2.407e+04	(-3.701e+04, -1.114e+04)
p2 =	4.605e+04	(1.889e+04, 7.321e+04)
p3 =	-3.467e+04	(-5.699e+04, -1.234e+04)
p4 =	1.282e+04	(3845, 2.179e+04)
p5 =	-2306	(-4066, -545.6)
p6 =	189.1	(54.47, 323.7)

$$R^2 = 0.9998$$

Poly6

Linear model Poly6:

$$\text{val}(x) = p1*x^6 + p2*x^5 + p3*x^4 + p4*x^3 + p5*x^2 + p6*x + p7$$

Coefficients (with 95% confidence bounds):

p1 =	7.637e+04	(-5.771e+05, 7.298e+05)
p2 =	-2.157e+05	(-1.856e+06, 1.424e+06)
p3 =	2.432e+05	(-1.445e+06, 1.931e+06)
p4 =	-1.41e+05	(-1.052e+06, 7.701e+05)
p5 =	4.449e+04	(-2.274e+05, 3.163e+05)
p6 =	-7247	(-4.973e+04, 3.524e+04)
p7 =	504.1	(-2210, 3218)

$$R^2 = 0.9999$$

A plot comparing the above curve fits of η vs. ε for the *K056* configuration are provided in Fig. D.6.

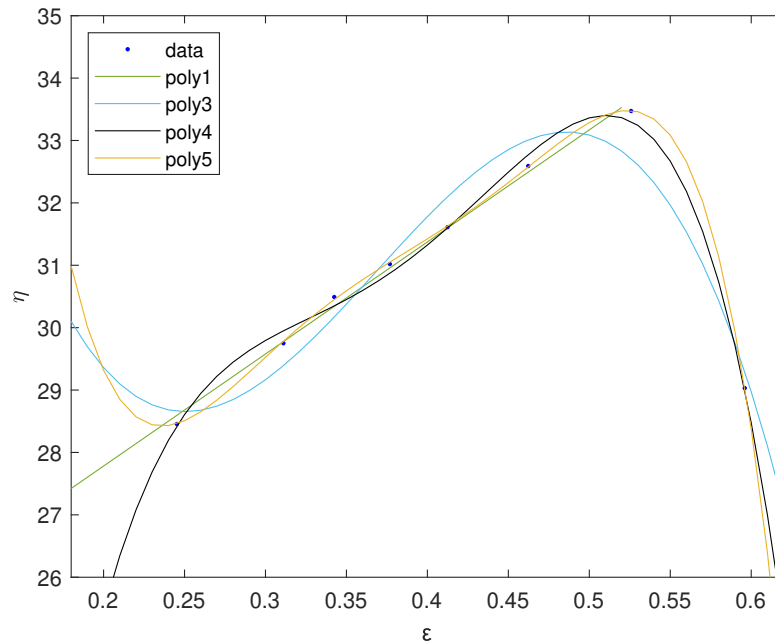


Figure D.6: Comparison of curve trends of η vs. ε for the *K056* configuration.

Appendix E

Blockage Corrections

E.1 Barnsley and Wellicome Correction

The measured results in this thesis were compared with the Barnsley and Wellicome (BW) correction [101], which is an analytical correction based on continuity, the conservation of energy, and conservation of momentum on flow around an actuator disk. The analysis considers a streamtube which contains the actuator disk, and defines i stations: (1) far upstream of the turbine, (2) just upstream of the turbine, (3) just downstream of the turbine, and (4) far downstream of the turbine. Velocities within and outside of the streamtube at each station are defined as fractions of the freestream velocity, designated by α_i and β_i , respectively. This is illustrated in Fig. E.1.

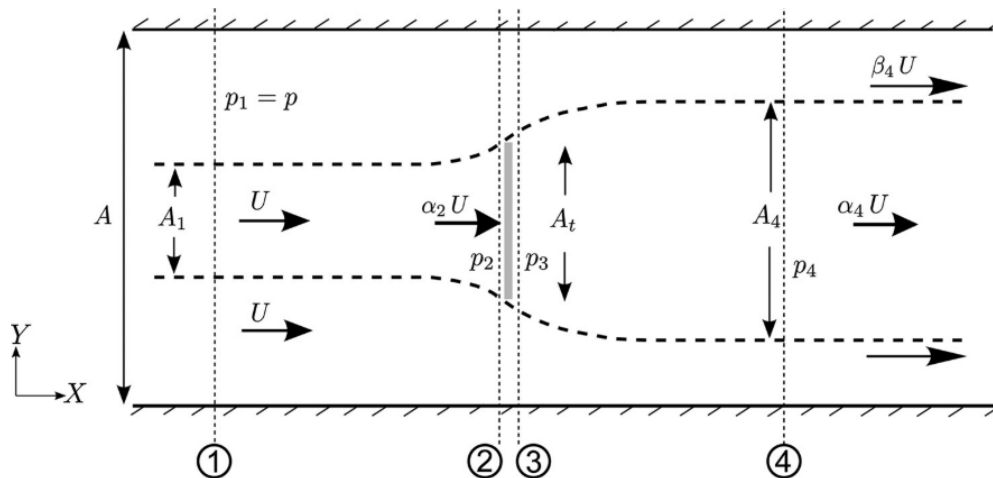


Figure E.1: Illustration of the control volume used in the BW blockage correction analysis [6].

The reader is referred to Gauthier et al. [6] for a comprehensive derivation of the correction, which determines the ratio of freestream velocity in the confined arrangement U , to the equivalent freestream velocity in an equivalent unconfined environment U' . Since the power coefficient is proportional to U^3 , the equivalent power coefficient in an unconfined environment C'_p is given by the relation

$$C'_p = C_p \left(\frac{U}{U'} \right)^3. \quad (\text{E.1})$$

Other key equations for the calculation include the results for the velocity ratio terms, α_i and β_i :

$$\frac{\alpha_2}{\alpha_4} = \frac{-1 + \sqrt{1 + \varepsilon \left[\left(\frac{\beta_4}{\alpha_4} \right)^2 - 1 \right]}}{\varepsilon \left(\frac{\beta_4}{\alpha_4} - 1 \right)}, \quad (\text{E.2})$$

$$\frac{1}{\alpha_4} = \frac{\beta_4}{\alpha_4} - \varepsilon \frac{\alpha_2}{\alpha_4} \left(\frac{\beta_4}{\alpha_4} - 1 \right), \quad (\text{E.3})$$

$$\frac{\beta_4}{\alpha_4} = \sqrt{C_p \left(\frac{1}{\alpha_4} \right)^2 + 1}, \quad (\text{E.4})$$

$$\alpha_2 = \frac{\alpha_2}{\alpha_4} \left[\frac{\beta_4}{\alpha_4} - \varepsilon \frac{\alpha_2}{\alpha_4} \left(\frac{\beta_4}{\alpha_4} - 1 \right) \right]^{-1}. \quad (\text{E.5})$$

Because force measurements were not taken directly, the method used by Gauthier et al. [6] was modified to include the calculation of the drag coefficient C_D from the power coefficient C_p :

$$C_D = C_p \left(\frac{c}{2\alpha_2 H_0} \right) \quad (\text{E.6})$$

The α_i and β_i parameters were calculated using the modified iterative process outlined by Gauthier et al. [6]:

1. Provide an initial guess for β_4/α_4 and α_2 .
2. Calculated C_D from Eq. E.6.

3. Calculate α_2/α_4 from Eq. E.2.
4. Calculate $1/\alpha_4$ from Eq. E.3.
5. Calculate β_4/α_4 from Eq. E.4.
6. Calculate α_2 from Eq. E.5.
7. Repeat until the residual of β_4/α_4 between iterations is less than 10^{-6} .

The confined configuration is then compared to an unconfined configuration using the following relations:

$$C_D U^2 = D'_D U'^2, \quad (\text{E.7})$$

$$\alpha_2 U = \alpha'_2 U'. \quad (\text{E.8})$$

Using a momentum analysis on the unconfined configuration combined with the above relations results in the velocity ratio of confined and unconfined values:

$$\frac{U}{U'} = \frac{\alpha_2}{\alpha_2^2 + C_D/4}. \quad (\text{E.9})$$

The velocity ratio was then calculated at each experimental confinement level, and the corrected power coefficient values were obtained using Eq. E.1.

The MatLab code used to calculate the corrected C_p values for each configuration is provided below:

```
%-----
clear
clc
close

%epsilon for both configs
eps_K0 = transpose([0.214787486637185 0.274229514321351...
0.299724801860621 0.325901261907801 0.356168136454852...
0.397579927347693 0.463642645995721 0.524444963031161]);

eps_K056 = transpose([0.245253906502714 0.311076254547952...
0.342472203085873 0.376815053802996 0.412453474522421...
0.462262443421617 0.525818987899799 0.596025350002993]);
```

```

eps=cat(1,eps_K0,eps_K056);

c=.0505; %chord length
% Cp data
cp_K0 = transpose([0.737816606102862 0.785863097863982...
0.813055950896917 0.817607810421112 0.831749995540476...
0.860285583330237 0.956820773152235 0.963236290722575]);

cp_K056 = transpose([0.89335070010747 0.937040133124583...
0.982368509029539 1.0098734008904 1.03065920881199...
1.06099523069437 1.08180576326725 0.947989489056794]);

cp=cat(1,cp_K0,cp_K056);

% heave amplitudes
H0_K0 = c*transpose([1.07 1.10 1.12 1.12 1.13 1.15 1.22 1.23]);
H0_K056 = c*transpose([1.22 1.24 1.28 1.30 1.31 1.34 1.38 1.40]);

H0=cat(1,H0_K0,H0_K056);

beta4alpha4 = 1.6*ones(size(cp)); %beta4 / alpha4
R=ones(size(cp));
residual = 1;
iter=0;
CD=ones(size(cp));
CD_new=ones(size(cp));
alpha2=0.8*ones(size(cp));
alpha2alpha4=ones(size(cp));
inv_alpha=ones(size(cp));
beta4alpha4_new=ones(size(cp));

while residual>10^(-6) && iter<10^6
    for i = 1:16
        CD(i) = cp(i).*(c/(2*alpha2(i).*H0(i)));
        alpha2alpha4(i) = (-1 + sqrt(1 +eps(i) .*(beta4alpha4(i)...
^2-1)))/(eps(i).*(beta4alpha4(i) -1)); %alpha2/alpha4

```

```

    inv_alpha(i) = beta4alpha4(i) - eps(i) .*...
    alpha2alpha4(i) *(beta4alpha4(i) - 1); %1/alpha
    beta4alpha4_new(i) = sqrt(CD(i).*(inv_alpha(i) )^2+1);
    alpha2(i) = alpha2alpha4(i) * (beta4alpha4(i)-eps(i)).*...
    alpha2alpha4(i)*(beta4alpha4(i)-1))^(-1);

    R(i) = beta4alpha4_new(i)-beta4alpha4(i);
    beta4alpha4(i) = beta4alpha4_new(i);
    iter=iter+1;
    residual=max(abs(R));
end
end

for i=1:16
    ratio_U(i) = alpha2(i)./(alpha2(i).^2+CD(i)./4);
    cp_cor(i) = cp(i).*ratio_U(i)^3;
end

cp_K0_cor = cp_cor(1:8);
cp_K056_cor = cp_cor(9:16);

```

E.2 Houlby Correction

A second correction was applied to the experimental data to correct for blockage effects. This correction relies on the linear momentum analysis applied to an actuator disk in a control volume with a free surface, derived by Houlby et al [7]. A 1D momentum analysis is once again employed. This analysis, however, accounts for a height change due to the free surface, and adds a fifth station (5) far downstream to account for wake mixing. A graphic of the analyzed configuration is provided in Fig. E.2.

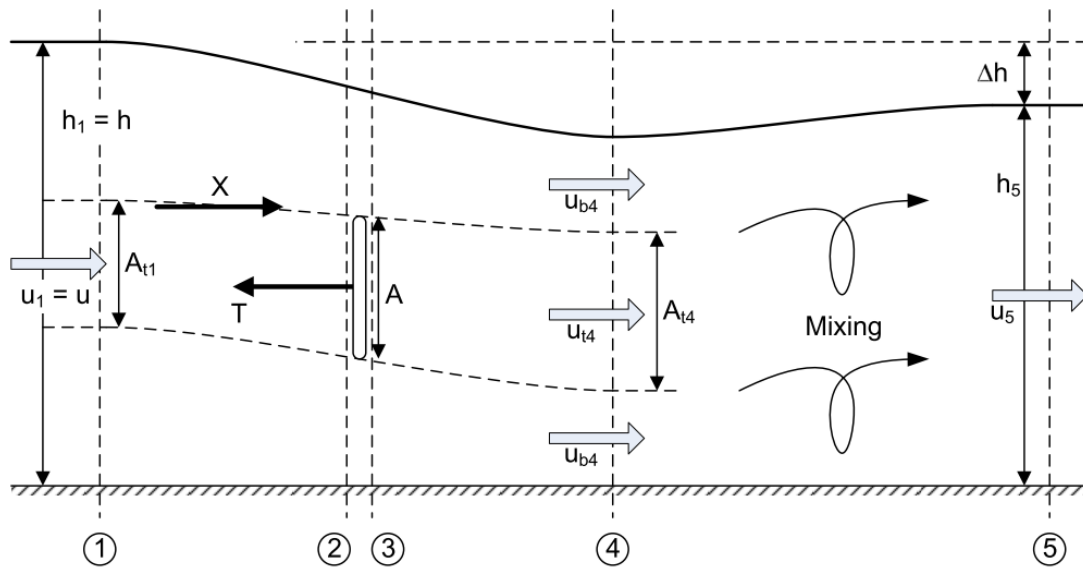


Figure E.2: Illustration of the control volume used in the 1D momentum analysis considering free surface effects and downstream wake mixing [7]

This appendix provides only the key equations needed to perform the blockage correction analysis, however a comprehensive derivation can be found in Houlby et al. [7].

The adjusted power coefficient C_p can be obtained again using the relation in Eq. E.1. Velocity ratios at different stations are again obtained using an iterative approach, with the following key equations:

$$\alpha_4 = \sqrt{\beta_4^2 - C_D} \quad (\text{E.10})$$

$$\alpha_2 = \frac{2(\beta_4 + \alpha_4) - (\beta_4 - 1)^3 / \epsilon \beta_4 (\beta_4 - \alpha_4)}{4 + (\beta_4^2 - 1) / \alpha_4 \beta_4} \quad (\text{E.11})$$

$$\frac{F_r^2}{2} \beta_4^4 + 2\alpha_4 F_r^2 \beta_4^3 - (2 - 2\varepsilon + F_r^2) \beta_4^2 - (4\alpha_4 + 2\alpha_4 F_r^2 - 4) \beta_4 + \left(\frac{F_r^2}{2} + 4\alpha_4 - 2\varepsilon\alpha_4^2 - 2 \right) = 0 \quad (\text{E.12})$$

where $F_r = u/\sqrt{gh}$ is the Froude number and $\beta_4 > 1$, and $1 > \alpha_2 > \alpha_4$.

The following iteration loop is then applied to calculate the α_i and β_i parameters:

1. Provide an initial guess for β_4 , such that $\beta_4 > 1$, and for α_2 , such that $0 < \alpha_2 < 1$.
2. Calculate C_D from Eq. E.6.
3. Calculate α_4 from Eq. E.10.
4. Calculate α_2 from Eq. E.11
5. Calculate β_4 from Eq. E.12. Select the root which satisfies the conditions $\beta_4 > 1$ and $1 > \alpha_2 > \alpha_4$.
6. Calculate the residual between the new and previous values of β_4 and repeat previous steps until residual is less than 10^{-6} . Use a relaxation parameter to ensure the iterations are stable.

Once the value of α_2 is determined, the final steps from Gauthier et al.'s analysis can be applied, comparing the values of the confined configuration to those of an unconfined configuration. Specifically, Eqs. E.9 and E.1 are calculated.

The change in height between the upstream and downstream stations Δh can also be calculated using the following cubic formula:

$$\frac{1}{2} \left(\frac{\Delta h}{h} \right)^3 - \frac{3}{2} \left(\frac{\Delta h}{h} \right)^2 + \left(1 - F_r^2 + \frac{C_D \varepsilon F_r^2}{2} \right) \left(\frac{\Delta h}{h} \right) - \frac{C_D \varepsilon F_r^2}{2} = 0 \quad (\text{E.13})$$

The MatLab code used to correct the C_p values for each configuration is provided below:

```
%-----
%specify principal dimensioning parameters
rho = 998.2;
g=9.81;
h = 0.42;
U=0.377; %upstream velocity
```

```

Fr = U/sqrt(g*h);% Froude number

%initial guess
beta_4=1.15*ones(1,16);
alpha_2=0.8*ones(size(beta_4));

%initialize values and arrays
R=ones(size(beta_4));
iter=0;
alpha_4=zeros(size(beta_4));
beta_4_new=zeros(size(beta_4));
residual=1;

%iteration loop
while residual>10^(-6) && iter<10^6
    for i=1:16
        cd(i) = cp(i)/(2*alpha_2(i)*H0(i));
        alpha_4(i) = sqrt(beta_4(i)^2-cd(i));
        alpha_2(i) = (2*(beta_4(i)+alpha_4(i))-(beta_4(i)-1)^3 ...
            /(eps(i)*beta_4(i)*(beta_4(i)-alpha_4(i))))/(4+...
            ((beta_4(i)^2-1)/(alpha_4(i)*beta_4(i))));

        coefvct_beta4 = [(Fr^2/2) (2*alpha_4(i)*Fr^2) (-(2-2*eps(i)+...
            Fr^2)) (-(4*alpha_4(i) + 2*alpha_4(i)*Fr^2-4)) ((Fr^2/2...
            +4*alpha_4(i) -2*eps(i)*alpha_4(i)^2-2))]; % Coefficient Vector
        beta_4_roots = roots(coefvct_beta4) ;

        beta_4_new(i)=beta_4_roots(3);
        R(i) = beta_4_new(i)-beta_4(i);
        residual=max(abs(R));
        beta_4(i) = (.5*beta_4_new(i)+.5*beta_4(i)) ; %under relax by...
        taking average of new and old values for stability
        iter=iter+1;
    end
end

%calculate corrected values for U, Cp

```

```
for i=1:16
    ratio_U(i) = alpha_2(i)/(alpha_2(i)^2+cd(i)/4);
    cp_cor(i) = cp(i)*ratio_U(i)^3;
end

cp_K0_cor = cp_cor(1:8);
cp_K056_cor = cp_cor(9:16);
%-----
```

Bibliography

- [1] M. Boudreau, G. Dumas, M. Rahimpour, and P. Oshkai, “Experimental investigation of the energy extraction by a fully-passive flapping-foil hydrokinetic turbine prototype,” *Journal of Fluids and Structures*, vol. 82, pp. 446–472, 2018.
- [2] E. Gauthier, “Oscillating-Foils Hydrokinetic Turbine Performance Prediction: Impact of Turbulence Modeling, of Structure Interference and of Confinement,” Master’s thesis, 2015.
- [3] T. Kinsey, G. Dumas, G. Lalande, J. Ruel, A. Méhut, P. Viarouge, J. Lemay, and Y. Jean, “Prototype testing of a hydrokinetic turbine based on oscillating hydrofoils,” *Renewable Energy*, vol. 36, no. 6, pp. 1710–1718, 2011.
- [4] C. Garrett and P. Cummins, “The efficiency of a turbine in a tidal channel,” *Journal of Fluid Mechanics*, vol. 588, pp. 243–251, 2007.
- [5] M. Boudreau, “Optimizing the power-generation performance of flapping-foil turbines while simplifying their mechanical design with the use of elastic supports,” Ph.D. thesis, Université Laval, 2018.
- [6] E. Gauthier, T. Kinsey, and G. Dumas, “Impact of blockage on the hydrodynamic performance of oscillating-foils hydrokinetic turbines,” *Journal of Fluids Engineering, Transactions of the ASME*, vol. 138, no. 9, pp. 1–13, 2016.
- [7] G. T. Houlsby, S. Draper, and M. L. G. Oldfield, “Application of Linear Momentum Actuator Disc Theory to Open Channel Flow by,” *Report no. OUEL*, no. July 2015, pp. 1–23, 2008.
- [8] IPCC, “Summary for policymakers. in: Climate change 2021: The physical science basis,” tech. rep., Cambridge University Press. In Press, 2021.
- [9] GovernmentofCanada, “The paris agreement,” Jan. 1, 2016 [Online].
- [10] IEA, “Net zero by 2050,” tech. rep., IEA, Paris, 2021. <https://www.iea.org/reports/net-zero-by-2050>.

- [11] Hydro-Québec, “Renewable energy option: Hydrokinetic power.” <https://www.hydroquebec.com/sustainable-development/specialized-documentation/renewable-energy.html>, 2021. Accessed 7 January 2022.
- [12] M. S. Chowdhury, K. S. Rahman, V. Selvanathan, N. Nuthammachot, M. Suklueng, A. Mostafaeipour, A. Habib, M. Akhtaruzzaman, N. Amin, and K. Techato, “Current trends and prospects of tidal energy technology,” *Environment, Development and Sustainability*, vol. 23, no. 6, pp. 8179–8194, 2021.
- [13] W. Shyy, H. Aono, C.-k. Kang, and H. Liu, *An Introduction to Flapping Wing Aerodynamics*. Cambridge Aerospace Series, Cambridge University Press, 2013.
- [14] M. Sfakiotakis, D. M. Lane, and J. B. C. Davies, “Review of fish swimming modes for aquatic locomotion,” *IEEE Journal of Oceanic Engineering*, vol. 24, no. 2, pp. 237–252, 1999.
- [15] D. Weihs, “Stability versus maneuverability in aquatic locomotion,” *Integrative and Comparative Biology*, vol. 42, no. 1, pp. 127–134, 2002.
- [16] K. A. Harper, M. D. Berkemeier, and S. Grace, “Modeling the Dynamics of Spring-Driven Oscillating-Foil Propulsion,” *Aerospace*, vol. 23, no. 3, pp. 1–16, 1998.
- [17] P. R. Bandyopadhyay, “Maneuvering hydrodynamics of fish and small underwater vehicles,” *Integrative and Comparative Biology*, vol. 42, no. 1, pp. 102–117, 2002.
- [18] D. Barrett, M. Grosenbaugh, and M. Triantafyllou, “Optimal control of a flexible hull robotic undersea vehicle propelled by an oscillating foil,” *Proceedings of the IEEE Symposium on Autonomous Underwater Vehicle Technology*, pp. 1–9, 1996.
- [19] Y. Fung, *An Introduction to the Theory of Aeroelasticity*. Dover Books on Aeronautical Engineering, Dover Publications, 2008.
- [20] P. R. Bandyopadhyay, “Swimming and flying in nature - The route toward applications: The freeman scholar lecture,” *Journal of Fluids Engineering, Transactions of the ASME*, vol. 131, no. 3, pp. 0318011–03180129, 2009.
- [21] S. S. Bhat, J. Zhao, J. Sheridan, K. Hourigan, and M. C. Thompson, “Effects of flapping-motion profiles on insect-wing aerodynamics,” *Journal of Fluid Mechanics*, vol. 884, pp. A8–1–23, 2020.
- [22] J. D. Eldredge and A. R. Jones, “Leading-edge vortices: Mechanics and modeling,” *Annual Review of Fluid Mechanics*, vol. 51, pp. 75–104, 2019.

- [23] C. P. Ellington, C. V. den Berg, A. P. Willmott, and A. L. R. Thomas, “Leading-edge vortices in insect flight,” *Nature*, vol. 384, pp. 626–630, 1996.
- [24] M. H. Dickinson, F.-o. Lehmann, S. P. Sane, M. H. Dickinson, F.-o. Lehmann, and S. P. Sane, “Wing Rotation and the Aerodynamic Basis of Insect Flight,” *Science*, vol. 284, no. 5422, pp. 1954–1960, 1999.
- [25] M. Boudreau and G. Dumas, “Vortex dynamics in the wake of three generic types of freestream turbines,” *Journal of Fluids Engineering, Transactions of the ASME*, vol. 140, no. 2, 2018.
- [26] I. Fenercioglu, B. Zaloglu, J. Young, M. A. Ashraf, J. C. Lai, and M. F. Platzer, “Flow structures around an oscillating-wing power generator,” *AIAA Journal*, vol. 52, no. 11, pp. 3316–3326, 2015.
- [27] K. Lu, Y. Xie, D. Zhang, and G. Xie, “Systematic investigation of the flow evolution and energy extraction performance of a flapping-airfoil power generator,” *Energy*, vol. 89, pp. 138–147, 2015.
- [28] F. F. Siala, M. W. Prier, and J. A. Liburdy, “Force production mechanisms of a heaving and pitching foil operating in the energy harvesting regime,” *American Society of Mechanical Engineers, Fluids Engineering Division (Publication) FEDSM*, vol. 1, pp. 1–11, 2018.
- [29] J. Young, J. C. Lai, and M. F. Platzer, “A review of progress and challenges in flapping foil power generation,” *Progress in Aerospace Sciences*, vol. 67, pp. 2–28, 2014.
- [30] Q. Xiao and Q. Zhu, “A review on flow energy harvesters based on flapping foils,” *Journal of Fluids and Structures*, vol. 46, pp. 174–191, 2014.
- [31] X. Wu, X. Zhang, X. Tian, X. Li, and W. Lu, “A review on fluid dynamics of flapping foils,” *Ocean Engineering*, vol. 195, p. 106712, 2020.
- [32] W. McKinney and J. DeLaurier, “Wingmill: an oscillating-wing windmill,” *Journal of Energy*, vol. 5, no. 2, pp. 109–115, 1981.
- [33] K. D. Jones, K. Lindsey, and M. F. Platzer, “An investigation of the fluid-structure interaction in an oscillating-wing micro-hydropower generator,” *WIT Transactions on the Built Environment*, vol. 71, pp. 72–82, 2003.
- [34] T. Kinsey and G. Dumas, “Parametric study of an oscillating airfoil in a power-extraction regime,” *AIAA Journal*, vol. 46, no. 6, pp. 1318–1330, 2008.

- [35] A. Betz, “Das Maximum der Theoretisch Möglichen Ausnützung des Windes Durch Windmotoren,” *Zeitschrift für das Gesamte Turbinenwesen*, vol. 26, pp. 307–309, 1920.
- [36] H. ABIRU and A. YOSHITAKE, “Study on a Flapping Wing Hydroelectric Power Generation System,” *Journal of Environment and Engineering*, vol. 6, no. 1, pp. 178–186, 2011.
- [37] B. J. Simpson, F. S. Hover, and M. S. Triantafyllou, “Experiments in direct energy extraction through flapping foils,” 2008.
- [38] J. Deng, L. Teng, D. Pan, and X. Shao, “Inertial effects of the semi-passive flapping foil on its energy extraction efficiency,” *Physics of Fluids*, vol. 27, no. 5, 2015.
- [39] Q. Zhu, M. Haase, and C. H. Wu, “Modeling the capacity of a novel flow-energy harvester,” *Applied Mathematical Modelling*, vol. 33, no. 5, pp. 2207–2217, 2009.
- [40] Q. Zhu and Z. Peng, “Mode coupling and flow energy harvesting by a flapping foil,” *Physics of Fluids*, vol. 21, no. 3, 2009.
- [41] E. Shimizu, K. Isogai, and S. Obayashi, “Multiobjective design study of a flapping wing power generator,” *Journal of Fluids Engineering, Transactions of the ASME*, vol. 130, no. 2, pp. 0211041–0211048, 2008.
- [42] L. Teng, J. Deng, D. Pan, and X. Shao, “Effects of non-sinusoidal pitching motion on energy extraction performance of a semi-active flapping foil,” *Renewable Energy*, vol. 85, pp. 810–818, 2016.
- [43] M. Boudreau, K. Gunther, and G. Dumas, “Investigation of the energy-extraction regime of a novel semi-passive flapping-foil turbine concept with a prescribed heave motion and a passive pitch motion,” *Journal of Fluids and Structures*, vol. 84, pp. 368–390, 2019.
- [44] D. Poirel, Y. Harris, and A. Benaïssa, “Self-sustained aeroelastic oscillations of a NACA0012 airfoil at low-to-moderate Reynolds numbers,” *Journal of Fluids and Structures*, vol. 24, no. 5, pp. 700–719, 2008.
- [45] Z. Peng and Q. Zhu, “Energy harvesting through flow-induced oscillations of a foil,” *Physics of Fluids*, vol. 21, no. 12, pp. 1–9, 2009.
- [46] Z. Wang, L. Du, J. Zhao, and X. Sun, “Structural response and energy extraction of a fully passive flapping foil,” *Journal of Fluids and Structures*, vol. 72, 2017.

- [47] N. Duarte, Leandro Dellinger, G. Dellinger, A. Ghenaïm, and A. Terfous, “Experimental investigation of the dynamic behaviour of a fully passive flapping foil hydrokinetic turbine,” *Journal of Fluids and Structures*, vol. 88, p. 12, 2019.
- [48] Q. Zhu, “Energy harvesting by a purely passive flapping foil from shear flows,” *Journal of Fluids and Structures*, vol. 34, pp. 157–169, 2012.
- [49] W. Jiang, Y. L. Wang, D. Zhang, and Y. H. Xie, “Numerical investigation into the effect of nonlinear spring on the adaptation of an oscillating foil for energy extraction,” *Renewable Energy*, vol. 117, pp. 12–21, 2018.
- [50] W. Jiang, Y. L. Wang, D. Zhang, and Y. H. Xie, “Numerical investigation into power extraction by a fully passive oscillating foil with double generators,” *Renewable Energy*, vol. 133, pp. 32–43, 2019.
- [51] W. Jiang, Y. L. Wang, D. Zhang, and Y. H. Xie, “Numerical investigation into the energy extraction characteristics of 3D self-induced oscillating foil,” *Renewable Energy*, vol. 148, pp. 60–71, 2020.
- [52] J. C. Veilleux and G. Dumas, “Numerical optimization of a fully-passive flapping-airfoil turbine,” *Journal of Fluids and Structures*, vol. 70, 2017.
- [53] M. Boudreau, M. Picard-Deland, and G. Dumas, “A parametric study and optimization of the fully-passive flapping-foil turbine at high Reynolds number,” *Renewable Energy*, vol. 146, pp. 1958–1975, 2020.
- [54] L. Duarte, N. Dellinger, G. Dellinger, A. Ghenaïm, and A. Terfous, “Experimental optimisation of the pitching structural parameters of a fully passive flapping foil turbine,” *Renewable Energy*, vol. 171, pp. 1436–1444, 2021.
- [55] M. N. M. Qadri, F. Zhao, and H. Tang, “Fluid-structure interaction of a fully passive flapping foil for flow energy extraction,” *International Journal of Mechanical Sciences*, vol. 177, no. February, p. 105587, 2020.
- [56] Q. Zhu, “Optimal frequency for flow energy harvesting of a flapping foil,” *Journal of Fluid Mechanics*, vol. 675, pp. 495–517, 2011.
- [57] M. Picard-Deland, M. Olivier, G. Dumas, and T. Kinsey, “Oscillating-foil turbine operating at large heaving amplitudes,” *AIAA Journal*, vol. 57, no. 12, pp. 5104–5113, 2019.

- [58] Z. Qi, J. Zhai, G. Li, and J. Peng, “Effects of non-sinusoidal pitching motion on the propulsion performance of an oscillating foil,” *Plos One*, vol. 14, no. 7, p. e0218832, 2019.
- [59] F. S. Hover, Haugsdal, and M. S. Triantafyllou, “Effect of angle of attack profiles in flapping foil propulsion,” *Journal of Fluids and Structures*, vol. 19, no. 1, pp. 37–47, 2004.
- [60] M. Platzer, M. Ashraf, J. Young, and J. Lai, *Development of a New Oscillating-Wing Wind and Hydropower Generator*. 2009.
- [61] M. A. Ashraf, J. Young, J. C. Lai, and M. F. Platzer, “Numerical analysis of an oscillating-wing wind and hydropower generator,” *AIAA Journal*, vol. 49, no. 7, pp. 1374–1386, 2011.
- [62] A. Boudis, A. Benzaoui, H. Oualli, O. Guerri, A. C. Bayeul-Lainé, and O. C. Delgoshia, “Energy extraction performance improvement of a flapping foil by the use of combined foil,” *Journal of Applied Fluid Mechanics*, vol. 11, no. 6, pp. 1651–1663, 2018.
- [63] B. Zhu, Y. Huang, and Y. Zhang, “Energy harvesting properties of a flapping wing with an adaptive Gurney flap,” *Energy*, vol. 152, pp. 119–128, 2018.
- [64] D. Iverson, M. Boudreau, G. Dumas, and P. Oshkai, “Boundary layer tripping on moderate Reynolds number oscillating foils,” *Journal of Fluids and Structures*, vol. 86, pp. 1–12, 2019.
- [65] W. Liu, Q. Xiao, and F. Cheng, “A bio-inspired study on tidal energy extraction with flexible flapping wings,” *Bioinspiration and Biomimetics*, vol. 8, no. 3, 2013.
- [66] T. Q. Le and J. H. Ko, “Effect of hydrofoil flexibility on the power extraction of a flapping tidal generator via two- and three-dimensional flow simulations,” *Renewable Energy*, vol. 80, pp. 275–285, 2015.
- [67] W. Liu, Q. Xiao, and Q. Zhu, “Passive flexibility effect on oscillating foil energy harvester,” *AIAA Journal*, vol. 54, no. 4, 2016.
- [68] A. D. Totpal, F. F. Siala, and J. A. Liburdy, “Energy harvesting of an oscillating foil at low reduced frequencies with rigid and passively deforming leading edge,” *Journal of Fluids and Structures*, vol. 82, no. August, pp. 329–342, 2018.
- [69] K. Lindsey, “A feasibility study of oscillating-wing power generators,” Master’s thesis, 2002.

- [70] T. Kinsey and G. Dumas, “Three-dimensional effects on an oscillating-foil hydrokinetic turbine,” *Journal of Fluids Engineering, Transactions of the ASME*, vol. 134, no. 7, pp. 1–11, 2012.
- [71] D. Kim, B. Strom, S. Mandre, and K. Breuer, “Energy harvesting performance and flow structure of an oscillating hydrofoil with finite span,” *Journal of Fluids and Structures*, vol. 70, no. September 2016, pp. 314–326, 2017.
- [72] T. Kinsey and G. Dumas, “Optimal operating parameters for an oscillating foil turbine at reynolds number 500, 000,” *AIAA Journal*, vol. 52, no. 9, pp. 1885–1895, 2014.
- [73] M. Sergio Campobasso, A. Piskopakis, J. Drofelnik, and A. Jackson, “Turbulent Navier-Stokes analysis of an oscillating wing in a power-extraction regime using the shear stress transport turbulence model,” *Computers and Fluids*, vol. 88, pp. 136–155, 2013.
- [74] P. Ma, Y. Wang, Y. Xie, and Z. Huo, “Effects of time-varying freestream velocity on energy harvesting using an oscillating foil,” *Ocean Engineering*, vol. 153, no. February, pp. 353–362, 2018.
- [75] T. Kinsey and G. Dumas, “Optimal tandem configuration for oscillating-foils hydrokinetic turbine,” *Journal of Fluids Engineering, Transactions of the ASME*, vol. 134, no. 3, 2012.
- [76] T. Kinsey and G. Dumas, “Computational fluid dynamics analysis of a hydrokinetic turbine based on oscillating hydrofoils,” *Journal of Fluids Engineering, Transactions of the ASME*, vol. 134, no. 2, pp. 1–16, 2012.
- [77] J. Xu, H. Sun, and S. Tan, “Wake vortex interaction effects on energy extraction performance of tandem oscillating hydrofoils,” *Journal of Mechanical Science and Technology*, vol. 30, no. 9, pp. 4227–4237, 2016.
- [78] G. D. Xu and W. H. Xu, “Energy extraction of two flapping foils with tandem configurations and vortex interactions,” *Engineering Analysis with Boundary Elements*, vol. 82, no. November 2016, pp. 202–209, 2017.
- [79] B. Kirschmeier, J. Summerour, and M. Bryant, “Experimental investigation of low aspect ratio, large amplitude, aeroelastic energy harvesting systems,” *Active and Passive Smart Structures and Integrated Systems 2017*, vol. 10164, no. April 2017, p. 101641F, 2017.

- [80] H. R. Karbasian, J. A. Esfahani, and E. Barati, "Simulation of power extraction from tidal currents by flapping foil hydrokinetic turbines in tandem formation," *Renewable Energy*, vol. 81, 2015.
- [81] P. Ma, Y. Wang, Y. Xie, and J. Zhang, "Analysis of a hydraulic coupling system for dual oscillating foils with a parallel configuration," *Energy*, vol. 143, pp. 273–283, 2018.
- [82] E. C. Maskell, "A Theory of the Blockage Effects on, Bluff Bodies and Stalled Wings in a Closed Wind Tunnel," *Reports and Memoranda*, no. 3400, 1963.
- [83] T. Kinsey and G. Dumas, "Impact of channel blockage on the performance of axial and cross-flow hydrokinetic turbines," *Renewable Energy*, vol. 103, 2017.
- [84] H. Glauert, *Airplane Propellers*, pp. 169–360. Berlin, Heidelberg: Springer Berlin Heidelberg, 1935.
- [85] C. Garrett and P. Cummins, "The power potential of tidal currents in channels," *Proceedings of the Royal Society A: Mathematical, Physical and Engineering Sciences*, vol. 461, no. 2060, pp. 2563–2572, 2005.
- [86] J. I. Whelan, J. M. Graham, and J. Peiró, "A free-surface and blockage correction for tidal turbines," *Journal of Fluid Mechanics*, vol. 624, pp. 281–291, 2009.
- [87] G. T. Houlsby and C. R. Vogel, "The power available to tidal turbines in an open channel flow," *Proceedings of Institution of Civil Engineers: Energy*, vol. 170, no. 1, pp. 12–21, 2017.
- [88] J. M. Gorle, L. Chatellier, F. Pons, and M. Ba, "Flow and performance analysis of H-Darrieus hydroturbine in a confined flow: A computational and experimental study," *Journal of Fluids and Structures*, vol. 66, pp. 382–402, 2016.
- [89] H. Jeong, S. Lee, and S. D. Kwon, "Blockage corrections for wind tunnel tests conducted on a Darrieus wind turbine," *Journal of Wind Engineering and Industrial Aerodynamics*, vol. 179, pp. 229–239, 2018.
- [90] H. Ross and B. Polagye, "An experimental assessment of analytical blockage corrections for turbines," *Renewable Energy*, vol. 152, pp. 1328–1341, 2020.
- [91] Y. Su, M. Miller, S. Mandre, and K. Breuer, "Confinement effects on energy harvesting by a heaving and pitching hydrofoil," *Journal of Fluids and Structures*, vol. 84, pp. 233–242, 2019.

- [92] F. Karakas and I. Fenercioglu, “Effect of side-walls on flapping-wing power-generation: An experimental study,” *Journal of Applied Fluid Mechanics*, vol. 9, no. 6, pp. 2769–2779, 2016.
- [93] C. M. Hoke, J. Young, J. C. Lai, F. Karakas, B. Zaloglu, and I. Fenercioglu, “Investigation of Oscillating-Foil Power Generation in Constrained Flow,” *Procedia Engineering*, vol. 199, pp. 3450–3455, 2017.
- [94] D. Iverson, “Experimental Investigation of Oscillating-Foil Technologies,” M.Sc. thesis, University of Victoria, 2018.
- [95] J.-C. Veilleux, “Optimization of a Fully-Passive Flapping-Airfoil Turbine,” M.Sc. thesis, Université Laval, 2014.
- [96] K. Fujiwara, R. Sriram, and K. Kotis, “Experimental investigations on the sharp leading-edge separation over a flat plate at zero incidence using particle image velocimetry,” *Experiments in Fluids*, vol. 61, no. 9, pp. 1–21, 2020.
- [97] T. Ota, Y. Asano, and J.-i. Okawa, “Reattachment Length and Transition of the Separated Flow over Blunt Flat Plates,” *Bulletin of the JSME*, vol. 24, no. 192, pp. 941–947, 1981.
- [98] Z. J. Taylor, R. Gurka, and G. A. Kopp, “Effects of leading edge geometry on the vortex shedding frequency of an elongated bluff body at high Reynolds numbers,” *Journal of Wind Engineering and Industrial Aerodynamics*, vol. 128, pp. 66–75, 2014.
- [99] B. F. Feeny and J. W. Liang, “A decrement method for the simultaneous estimation of Coulomb and viscous friction,” *Journal of Sound and Vibration*, vol. 195, no. 1, pp. 149–154, 1996.
- [100] W. Lee, “Influence of the Sweep Angle on the Leading Edge Vortex and its Relation to the Power Extraction of a Fully-Passive Oscillating-Plate Hydrokinetic Turbine Prototype,” M.Sc. thesis, University of Victoria, 2021.
- [101] M. Barnsley and J. Wellicome, “Final report on the 2nd phase of development and testing of a horizontal axis wind turbine test rig for the investigation of stall regulation aerodynamics,” *Carried Out Under ETSU Agreement No. E. A*, vol. 5, 1990.
- [102] A. S. Bahaj, A. F. Molland, J. R. Chaplin, and W. M. Batten, “Power and thrust measurements of marine current turbines under various hydrodynamic flow conditions in a cavitation tunnel and a towing tank,” *Renewable Energy*, vol. 32, no. 3, pp. 407–426, 2007.

- [103] F. Rehim, A. F., and N. B. Nasrallah, “Reorganization of coherent structures downstream a circular cylinder located between two parallel walls,” *Journal of Applied Fluid Mechanics*, vol. 4, no. 3, pp. 51–56, 2011.
- [104] J. Lighthill, *An Informal Introduction to Theoretical Fluid Mechanics*. New York: Oxford University Press, 1986.
- [105] S. H. Lamb, *Hydrodynamics*. Cambridge: University Press, sixth ed., 1932.
- [106] P. Oshkai and D. Rockwell, “Free Surface Wave Interaction With a Horizontal Cylinder,” *Journal of Fluids and Structures*, vol. 60, no. 10, pp. 935–954, 1999.
- [107] F. F. Siala and J. A. Liburdy, “Leading-edge vortex dynamics and impulse-based lift force analysis of oscillating airfoils,” *Experiments in Fluids*, vol. 60, no. 10, pp. 1–18, 2019.
- [108] D. Iverson, M. Rahimpour, W. Lee, T. Kiwata, and P. Oshkai, “Effect of chordwise flexibility on propulsive performance of high inertia oscillating-foils,” *Journal of Fluids and Structures*, vol. 91, p. 102750, 2019.